12-2018

Exploring Potential Water-Ice Occurrence on Asteroid 4 Vesta Using Orbital Radar Observations by the Dawn Mission

Elizabeth M. Palmer

EXPLORING POTENTIAL WATER-ICE OCCURRENCE ON ASTEROID 4 VESTA USING ORBITAL RADAR OBSERVATIONS BY THE DAWN MISSION

by

Elizabeth M. Palmer

A dissertation submitted to the Graduate College
in partial fulfillment of the requirements
for the degree of Doctor of Philosophy
Geological and Environmental Sciences
Western Michigan University
December 2018

Doctoral Committee:

William A. Sauck, Ph.D., Chair
Essam Heggy, Ph.D.
Wlodek Kofman, Ph.D.
Johnson R. Haas, Ph.D.

ACKNOWLEDGEMENTS

I would like to thank all of my peers who have supported me throughout the many stages of academic and personal growth that have led to the completion of this culminating document. I would also like to thank all those who acted as mentors along the way, especially Essam, who has shared considerable advice on charting the path toward a successful, fulfilling career in the Earth and planetary sciences. Most of all, I am grateful for the unwavering support my family, who has believed in me from the start and taught me to persevere.

Elizabeth M. Palmer

EXPLORING POTENTIAL WATER-ICE OCCURRENCE ON ASTEROID 4 VESTA USING ORBITAL RADAR OBSERVATIONS BY THE DAWN MISSION

Elizabeth M. Palmer, Ph.D.

Western Michigan University, 2018

Airless, differentiated planetesimals in the inner solar system were presumed to have been depleted of most of their initial volatile content during formation. However, water-ice has been discovered at the lunar poles (Li et al., 2018), is inferred to exist in polar craters on Mercury (e.g., Butler, Slade & Muhleman, 1993, and suggested to survive beneath the dusty regolith of objects in the main asteroid belt if buried at sufficient depths—at least one meter for small-bodies in the outer main-belt (Schorghofer, 2008). Hence, the study of volatile occurrence, past or present, on airless, desiccated small-bodies provides insights into the timing, distribution and potential delivery mechanisms of water to the inner solar system.

One technique particularly well-suited to such studies is radar remote sensing, which can characterize the electrical and textural properties of desiccated planetary surfaces (e.g., Campbell, 2002). However, accurately interpreting radar observations requires disentangling the primary geophysical parameters that affect frequency, power and polarization, including surface topography, surface dielectric properties (i.e., its relative permittivity—dependent on mineralogy, density, temperature and ice content) and surface roughness at wavelength scales (e.g., Ostro et al., 2002). Unfortunately, asteroid surface mineralogies are not well-constrained due to a lack of clear spectral analogs among meteorites, and their surface texture at centimeter-to-decimeter (cm-dm) scales is poorly constrained due to lack of high-resolution surface images.

However, a unique opportunity arises to address the above uncertainties with the recent orbital mission to Asteroid Vesta by NASA's Dawn spacecraft, which conducted the first orbital bistatic radar (BSR) observations of a small-body, using its high-gain communications antenna to transmit and Earth-based ground stations to receive (Palmer et al., 2017). To support accurate interpretation of Dawn's BSR observations, the first dielectric model of Vesta is constructed (Palmer

et al., 2015) by employing a mineralogical analogy with lunar basaltic soils to characterize the dielectric properties of the vestan regolith, adjusted for the temperatures and average surface density inferred from thermal observations by Dawn's Visible and Infrared mapping spectrometer (Capria et al., 2014). Vesta's surface dielectric constant is found to be uniform at ~2.4 at S- (2.3 GHz) and X-band (8.4 GHz) radar frequencies, suggesting that any variability in radar reflectivity can be attributed to variations in surface roughness (Palmer et al., 2015).

Subsequent power spectral analyses of Dawn BSR data reveal substantial radar reflectivity variability and therefore substantial variability in cm-dm surface roughness (Palmer et al., 2017). Unlike the Moon, surface roughness is not correlated with surface age, suggesting impact cratering alone cannot explain Vesta's surface texture. Furthermore, heightened subsurface hydrogen concentration occurring within extensive smoother areas suggests that potential ground-ice presence (accessed by deep, impact-induced fracturing) may have contributed to shaping Vesta's surface.

Finally, the feasibility of conducting a similar opportunistic BSR experiment at other small-bodies and moons is explored for several active and planned missions. Targets smaller than ~100 km in diameter require an onboard ultra-stable oscillator to achieve sufficient frequency stability for accurate power spectral analysis and interpretation of opportunistic BSR data in terms of surface roughness.

TABLE OF CONTENTS

Table of Contents—Continued

CHAPTER

Table of Contents—Continued

CHAPTER

Table of Contents—Continued

LIST OF TABLES

LIST OF FIGURES

CHAPTER I

INTRODUCTION

1. Volatile Occurrence on Asteroids

Planetesimals that accreted in the inner protoplanetary disk were presumed to have been depleted of most if not all of their highly volatile elements during formation (i.e., hydrogen, carbon, nitrogen, oxygen and noble gases)—whether as a result of high temperatures in the inner part of the solar nebula that prevented their condensation from a gas phase (e.g., Boss, 1998; Albarède, 2009); sublimation by high-energy collisions during the process of accretion (e.g., Halliday, 2004; Schlichting, Sari & Yalinewich, 2015); and/or depletion through global heating, melting and degassing of large planetesimals during differentiation, particularly for those lacking atmospheres (e.g., Elkins-Tanton, 2012; Day & Moynier, 2014). Hence, until recently, most inner solar system bodies lacking a substantive atmosphere were assumed completely dry. Direct evidence for surface exposed water-ice, however, has been discovered on the poles of both Mercury (Slade et al., 1992; Lawrence et al., 2013; Deutsch et al., 2017) and the Moon (Li et al., 2018), and widespread hydrated minerals have been observed across the lunar surface (Clark, 2009; Pieters et al., 2009; Sunshine et al., 2009). In addition, water has been discovered in primitive lunar volcanic glasses, suggesting much higher water content in the lunar mantle than previously thought (Saal et al., 2008; Hauri et al., 2011; Hauri et al., 2015; Milliken & Li, 2017), and evidence for mineral transport by aqueous solution has been identified in ancient meteorites that come from otherwise desiccated, differentiated asteroid parent bodies (Treiman, Lanzirotti & Xirouchakis, 2004; Barrat et al., 2011; Shearer et al., 2011; Sarafian et al., 2014; Warren et al., 2014).

Together, these observations suggest that water is far more pervasive throughout the inner solar system than once thought, raising further questions about how and when volatiles were delivered (if not initially accreted), and under what conditions water has been able to survive or be transported. Leading highly-debated hypotheses for a common source of water delivery to the inner solar system include: (1) direct accretion of hydrogen from the inner protoplanetary disk (e.g., Drake & Campins, 2006); (2) inward scattering of icy planetesimals from beyond the "snowline"—the heliocentric distance in the protoplanetary disk beyond which temperatures were sufficiently cool for water to condense and be accreted—during the orbital migration of the gas giant planets (e.g., Morbidelli et al., 2012); (3) asteroidal impacts with hydrated, carbonaceous-chondrite-like composition (e.g., Marty, 2012; Saal et al., 2013; Sarafian et al., 2014; Sarafian et al., 2017); or (4) cometary impacts (e.g., Delsemme, 1998; Hartogh et al., 2011; Lis et al., 2013), although substantial quantities of water delivery by comets have fallen out of favor, as their orbital dynamics prove difficult to generate a sufficiently large influx (Morbidelli et al., 2000), and several comets do not have a matching deuterium/hydrogen ratio with that of Earth's oceans (e.g., Alexander et al., 2012; Altwegg et al., 2015). In the case of airless, desiccated planetary surfaces, an additional process has been hypothesized to explain the distribution of hydrated minerals observed across the Moon: namely, solar-wind implantation of protons that bind with oxygen-rich silicate grains at the regolith surface to form OH- (e.g., Starukhina, 2001; Hasegawa et al., 2003; McCord et al., 2011), which is also expected to occur on other airless, desiccated siliceous bodies (e.g., Sunshine et al., 2009; Rivkin et al., 2018).

Hence, the study of water occurrence (past or present) on and within asteroids provides key insights into the timing, distribution and amount of water gained by the inner solar system, as well as the conditions under which water has survived. With respect to the latter, Schorghofer (2008) modeled ice loss rates in the main asteroid belt, and found that water-ice can survive over the lifetime of the solar system provided that the ice is buried at sufficient depth. Schorghofer (2008) suggests that Small-bodies in the outermost region of the main asteroid belt ($\gtrsim$3.2 AU) are able to host water-ice below one meter of their surface at any latitude if covered by a dusty insolating layer, and objects in the inner main asteroid belt (2-2.5 AU) are able to host buried ice at similar depths at their poles within seasonally or permanently shadowed craters. Schorghofer's (2008) model has therefore established the concept of a "buried snowline," identifying conditions that permit the retention of water-ice in the shallow subsurfaces of airless, otherwise-desiccated asteroids.

One of the most well-studied objects in the main asteroid belt is Asteroid 4 Vesta (hereafter Asteroid Vesta or simply Vesta), owing to its unique spectral signature among asteroids and strong similarity with the spectra of the howardite-eucrite-diogenite (HED) class of meteorites (e.g., McCord et al., 1970; McSween et al., 2013). Asteroid Vesta is the second most massive body in the main belt, and thought to be one of the few protoplanets from the inner solar system that has remained intact, spanning ~500 km in diameter and comprising roughly one-tenth the mass of the asteroid belt. Extensive geochemical, petrological and geochronological studies of the HED meteorites over the decades have also established that their parent-body is fully differentiated with an iron-nickel core, olivine-rich mantle and basaltic crust (e.g., Keil, 2002; McSween et al., 2011; and references therein), and therefore assumed largely depleted of its initial volatile content, as discussed above.

However, year-long orbital observations of Asteroid Vesta by NASA's Dawn spacecraft (Russell et al., 2012) have revealed several lines of evidence for past volatile occurrence on the surface: (1) the widespread presence of OH- bearing minerals across the surface as detected by the onboard Visible and InfraRed mapping spectrometer, VIR (De Sanctis et al., 2012); (2) heightened concentrations of subsurface hydrogen [H] that match the distribution of hydrated mineral distribution, as inferred from observations by the onboard Gamma Ray and Neutron Detector, GRaND (Prettyman et al., 2012); (3) the occurrence of low-albedo, dark material deposits in the same areas (as observed in optical images acquired by the onboard Framing Camera, FC) that are hypothesized to be remnants of carbonaceous chondrite impactors that delivered hydrogen-rich material (Prettyman et al., 2012; Reddy et al., 2012); (4) pitted terrain observed at the bottom of some crater floors from FC images, thought to form through the degassing of volatiles (Denevi et al., 2012); and (5) curvilinear gullies carved into the sides of several crater walls, as observed in FC images, providing geomorphologic evidence for potential transient fluid flow after impact-induced fracturing and heating of hydrous material and/or buried ice in the subsurface (Scully et al., 2015).

To support further characterization of Asteroid Vesta's surface properties, an opportunistic bistatic radar (BSR) experiment has been conducted by the Dawn mission in which the onboard high-gain communications antenna is used to transmit 3.5-cm (X-band, 8.5-GHz) radio waves toward Vesta's surface just before and after occultations, resulting in grazing-incidence forward-scattering of radio waves from Vesta's surface that are then received on Earth by ground stations for analysis (Palmer, Heggy & Kofman, 2017). In the next section, we describe the capability of high-frequency (~1-10 GHz) radar observations to investigate the potential occurrence, past or present, of water occurrence on airless, mostly desiccated planetary bodies.

2. Radar Characterization of Airless, Desiccated Planetary Surfaces

Radar remote sensing is a particularly useful technique for investigating the electrical and centimeter-to-meter textural properties of desiccated, airless planetary surfaces (e.g., Campbell, 2002). Unlike passive methods of remote sensing at visible and infrared wavelengths that measure the naturally reflected or emitted electromagnetic radiation from a target, radar antennas actively transmit energy with a predefined frequency, power and polarization before receiving the backscattered energy, hence not relying on external sources of illumination such as sunlight. Earth-based radar observations of Mercury at S- and X-band frequencies (13-cm, 2.4-GHz; and 3.5-cm, 8.5-GHz; respectively), for instance, have enabled the detection of water-ice deposits (for which $\varepsilon_r \approx 3 + i(3\times10^{-5})$ (Heggy et al., 2012)) in permanently shadowed polar craters due to the high radar brightness contrast of ice compared to surrounding terrain—attributed to subsurface volume scattering within ice deposits that results in a characteristic enhancement of the backscattered radar signal (Harmon & Slade, 1992; Slade, Butler & Muhleman, 1992; Butler, Muhleman & Slade, 1993). On the Moon, evidence for water-ice deposits in permanently shadowed polar craters were similarly inferred from orbital observations by the Clementine bistatic radar experiment at S-band (Nozette et al., 1996), and also by the Mini-RF imaging radar aboard the Lunar Reconnaissance Orbiter at S- and X-bands (Spudis et al., 2013).

In addition to assessing potential water-ice presence, high-resolution radar remote sensing has also been used to map variations in surface roughness at the radar wavelength (centimeter-to-decimeter) scale, which in turn yields insights into the primary geophysical processes (past or present) that have acted to smooth or roughen the Moon's airless, desiccated surface (e.g., Carter, Campbell & Campbell, 2011; Campbell, 2016). One of the primary smoothening mechanisms acting on airless, desiccated planetary surfaces such as the Moon is regolith gardening, the process by which a constant influx of micrometeorites gradually erode multi-meter-scale surface features (e.g., boulders) into progressively smaller fragments through impact-induced fracturing and frictional abrasion. It follows that the smoother the surface at the centimeter-to-decimeter scales observed by radar, the older and more eroded the regolith. Indeed, the youngest craters are observed to exhibit much higher surface roughness than old craters at centimeter to decimeter scales due to the recent excavation and deposition of blocky ejecta that have not yet undergone significant regolith gardening (e.g., Jawin et al., 2014). Another major process that generated smooth surfaces on the Moon was explosive volcanism, which resulted in the formation of fine-grained pyroclastic surficial deposits that are distinct in radar imaging due to their relative smoothness compared to surrounding terrain (e.g., Campbell et al., 2014). Given Asteroid Vesta's similar geologic history to that of the Moon, including differentiation, a possible global magma ocean, and the gardening of regolith by impacts (e.g., Keil, 2002), similar variability of surface roughness might be expected on Vesta's surface.

3. Statement of the Problem

To date, relatively few studies of asteroid surface properties have been conducted using radar remote sensing (e.g., Magri et al., 2001; Benner et al., 2008) since most observations are performed from Earth, making high-resolution radar imaging difficult for such small, distant bodies. Moreover, the accurate interpretation of surface radar backscatter in terms of the physical surface properties of a given target requires disentangling the primary geophysical parameters that can affect the return signal's frequency, power and polarization (Ostro et al., 2002), which for airless, desiccated planetary surfaces include: (1) surface topography; (2) the intrinsic dielectric properties of the surface material (i.e., the relative permittivity, which is dependent primarily on mineralogy, porosity, surface temperature and ice content); and (3) the wavelength-scale roughness of the asteroid's surface. For instance, see the work of Fa & Wieczorek (2012), who infer variations in lunar regolith thickness from 70-cm Earth-based radar observations by first using independent constraints on mineralogy and surface rock abundance to first model the regolith's dielectric properties, surface roughness and buried rock abundance.

Aside from the surface topography of asteroids, which can be accurately modeled from radar observations at decameter resolutions (Benner et al., 2015), the dielectric properties and roughness of asteroid surfaces remain poorly characterized. In particular, a lack of high-resolution multi-spectral observations has limited the ability to unambiguously identify surface mineralogy—and in turn, to identify spectral matches among meteorites (e.g., Burbine et al., 2002; Reddy et al., 2015;

DeMeo et al., 2015)—while a lack of high-resolution optical images impedes accurate assessment of surface roughness.

The Dawn mission, however, has provided the unique opportunity to address each of the above-mentioned uncertainties for Asteroid Vesta due to its high-resolution, year-long orbital observations of the surface (Russell et al., 2012). In the coming chapters, surface mineralogy, density and temperature are inferred from observations by Dawn's Visible and InfraRed mapping spectrometer to construct a dielectric model of the surface of Asteroid Vesta, which is then used as input to analyze the radar observations conducted opportunistically by the Dawn spacecraft to assess surface texture at centimeter to decimeter scales.

4. Research Questions

The following key scientific questions are addressed through the cumulative work presented in this dissertation:

(1) What are the dielectric properties of Asteroid Vesta's desiccated surface material at S- and X-band radar frequencies (2.3 GHz and 8.4 GHz, respectively), adjusted for the temperatures and porosity expected within the first meter of the regolith?

(2) What are the primary physical mechanisms that have shaped the variability of Asteroid Vesta's centimeter-to-decimeter-scale surface roughness as inferred from Dawn BSR observations? Does relative surface roughness correlate with relative surface age, as on the Moon?

(3) Given that all spacecraft are equipped with radio communications antennas, what are the minimum measurement requirements for other planned space missions to assess relative surface roughness on other small-bodies (using the same opportunistic technique as that employed by Dawn at Vesta)?

5. Significance of the Research

In 2011-2012, the Dawn mission acquired the first high-resolution orbital observations of Asteroid Vesta, and presented the unique opportunity to conduct the first orbital bistatic radar observations of a small-body, and therefore to assess its surface dielectric and roughness properties. The research contained within this dissertation presents the first dielectric (i.e., relative permittivity) model of Asteroid Vesta's surface (Palmer et al., 2015), the analysis and interpretation of the first orbital bistatic radar experiment to be conducted at a small-body (Palmer, Heggy & Kofman, 2017), and the first feasibility study for future missions to achieve the same potential roughness characterization of other small-bodies in the solar system. In turn, understanding the magnitude and spatial distribution of surface roughness on planetary bodies provides unique insight into the physical mechanisms that govern the evolution of their surfaces, and into the surface trafficability of such small-bodies in terms of safe landing, anchoring and sampling by future missions.

6. Summary of Chapters

Chapter II presents the "Dielectric Properties of Asteroid Vesta's Surface as Constrained by Dawn VIR Observations," which reports on the first dielectric model of Asteroid Vesta as derived from thermal observations by the Dawn mission's Visible and Infrared (VIR) mapping spectrometer (Palmer et al., 2015). The dielectric properties (i.e., relative permittivity) across the surface of Vesta is found to be uniform at tens-of-kilometer resolution, suggesting that any variability observed at such resolutions of the radar reflectivity of the surface will be indicative of variations in surface roughness at the wavelength-scale (i.e., centimeters to decimeters for ~1-10 GHz-frequency radar observations). The establishment of this dielectric model therefore supports quantitative interpretation of current and future Earth-based and orbital radar observations for small bodies, particularly for determining surface roughness variability. This article was first published by Palmer et al. (2015) in the peer-review scientific journal *Icarus*, and has been reprinted here in accordance with the initial copyright agreement granted to first authors.

Chapter III describes the analysis and interpretation of the first "Orbital Bistatic Radar Observations of Asteroid Vesta by the Dawn Mission," which uses the dielectric model of Vesta's surface from Chapter II in combination with orbital bistatic radar (BSR) observations of Vesta's surface to then infer relative surface roughness across the asteroid. The basic geometry of the opportunistic BSR experiment is depicted in Fig. 1, whereby the high-gain radio communications antenna (HGA) aboard the Dawn spacecraft continuously transmits radiowaves during entries into and exits from occultation of the spacecraft behind the asteroid, from Earth's point of view.

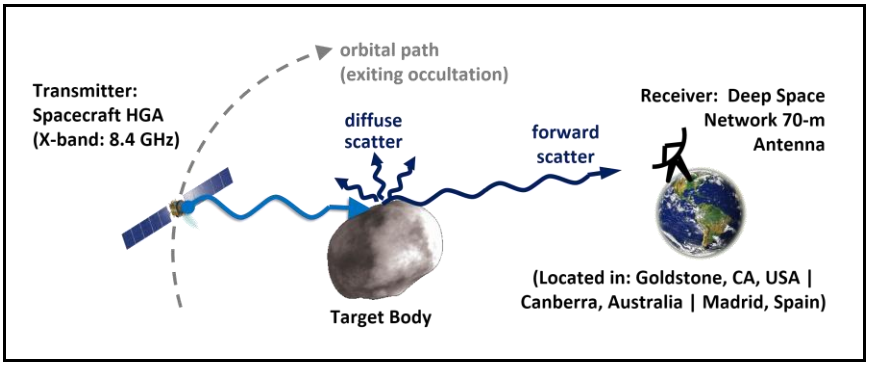

Figure 1. Simplified geometry (not to scale) of an orbital forward-scatter BSR experiment in a polar orbit around the target body. Adapted from Palmer, Heggy & Kofman (2017).

The portion of the signal that scatters from the surface of the asteroid is then received on Earth by one of three 70-meter radio antennas located in Goldstone, California (U.S.), Madrid (Spain) and Canberra (Australia), shown in Fig. 2, which in turn are part of NASA's Deep Space Network (DSN) of Earth-based radio antennas that are used for communications with planetary spacecraft—which include relaying commands, telemetry data and radiometric tracking data (e.g., Taylor, 2009).

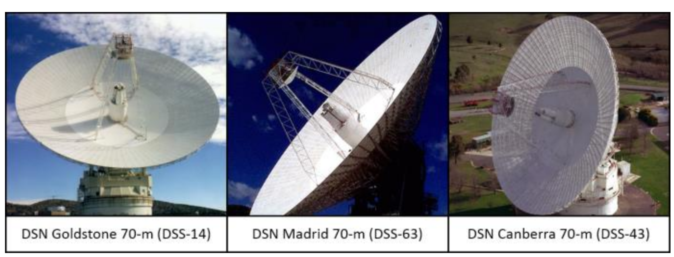

Figure 2. The three largest (70-m) Deep Space Network (DSN) antennas used for communications with planetary spacecraft throughout the solar system. The DSS-14 antenna is located in Goldstone, California (U.S.), DSS-63 in Madrid (Spain) and DSS-43 in Canberra (Australia). Image credit: *NASA.gov*.

Subsequent power spectral analysis of the surface-scattered telemetry radio signal is achieved through the processing steps shown in Fig. 3. Then, by measuring the power of the surface-scattered signal relative to the unimpeded direct signal (i.e., sent directly from the spacecraft to Earth without any occultation by the surface), variability in surface radar reflectivity could be inferred. In light of the surface's dielectric uniformity, these measurements have been interpreted as variability in surface roughness, and suggest that Vesta's surface texture may have been shaped by impact events that accessed potential ground-ice inclusions through heating, melting, and flow along impact-induced fractures. This article was first published in *Nature Communications* by Palmer, Heggy & Kofman (2017), and is reprinted here in accordance with the Creative Commons open copyright agreement.

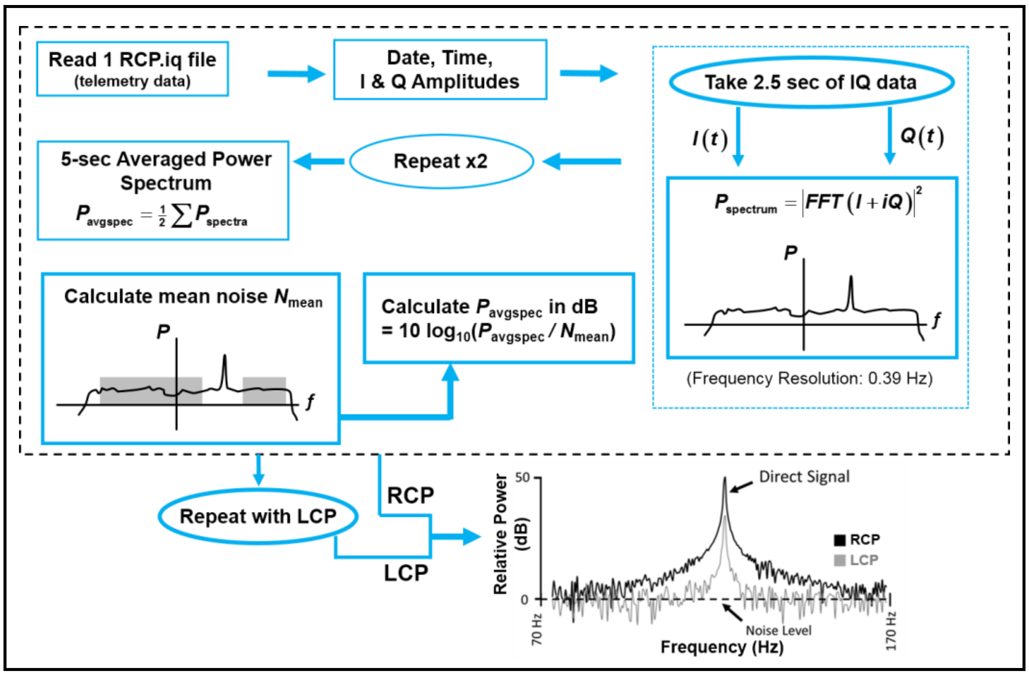

Figure 3. Signal processing steps for in-phase (I) and quadrature (Q) telemetry radio signals received by DSN 70-m antennas. In the case of Dawn BSR observations of Asteroid Vesta, the transmitting polarization was right-hand circular polarization (RCP), and the integration time for the fast-Fourier transform was 2.5 seconds to achieve a frequency resolution of ~0.39 Hz (see Chapter III for specifics).

In Chapter IV, the "Measurement Requirements for Orbital Forward-Scatter Bistatic Radar Observations of Planetary Surfaces" provides the minimum measurement requirements to conduct a successful opportunistic forward-scatter BSR experiment such as that at Vesta using the high-gain radio communications antennas aboard several active and planned planetary missions. Onboard ultra-stable oscillators are determined to be necessary for missions to targets smaller than ~100 km in diameter in order to accurately retrieve relative surface roughness. This work has been submitted to *IEEE Geoscience and Remote Sensing Letters* and is under review.

Chapter V, "Conclusions," presents a summary of key findings and implications from the results of Chapters II-IV, and discusses future opportunities for radar remote sensing to advance the scientific community's understanding of volatile occurrence and its survivability within the inner solar system.

Finally, the Appendix presents perspectives gained from three complementary studies that characterize the dielectric properties of comets and the Moon.

7. References

Albarède, F. (2009). "Volatile accretion history of the terrestrial planets and dynamic implications." *Nature*, **461**(7268), 1227–1233. doi:10.1038/nature08477

Alexander, C. M. O., Bowden, R., Fogel, M. L., Howard, K. T., Herd, C. D. K. & Nittler, L. R. (2012). "The Provenances of Asteroids, and Their Contributions to the Volatile Inventories of the Terrestrial Planets." *Science*, **337**(6095), 721–723. doi:10.1126/science.1223474

Altwegg, K., Balsiger, H., Bar-Nun, A., Berthelier, J. J., Bieler, A., Bochsler, P., Briois, C., Calmonte, U., Combi, M., Keyser, J. D., Eberhardt, P., Fiethe, B., Fuselier, S., Gasc, S., Gombosi, T. I., Hansen, K. C., Hässig, M., Jäckel, A., Kopp, E., Korth, A., LeRoy, L., Mall, U., Marty, B., Mousis, O., Neefs, E., Owen, T., Rème, H., Rubin, M., Sémon, T., Tzou, C.-Y., Waite, H. & Wurz, P. (2015). "67P/Churyumov-Gerasimenko, a Jupiter family comet with a high D/H ratio." *Science*, **347**(6220), 1261952. doi:10.1126/science.1261952

Barrat, J. A., Yamaguchi, A., Bunch, T. E., Bohn, M., Bollinger, C. & Ceuleneer, G. (2011). "Possible fluid–rock interactions on differentiated asteroids recorded in eucritic meteorites." *Geochim. Cosmochim. Acta*, **75**(13), 3839–3852. doi:10.1016/j.gca.2011.04.013

Benner, L. A. M., Busch, M. W., Giorgini, J. D., Taylor, P. A. & Margot, J.-L. (2015). "Radar Observations of Near-Earth and Main-Belt Asteroids." In P. Michel, F. E. DeMeo & W. F. Bottke, eds., *Asteroids IV*, University of Arizona Press. doi:10.2458/azu_uapress_9780816532131-ch009

Benner, L. A. M., Ostro, S. J., Magri, C., Nolan, M. C., Howell, E. S., Giorgini, J. D., Jurgens, R. F., Margot, J.-L., Taylor, P. A., Busch, M. W. & Shepard, M. K. (2008). "Near-Earth asteroid surface roughness depends on compositional class." *Icarus*, **198**(2), 294–304. doi:10.1016/j.icarus.2008.06.010

Boss, A. P. (1998). "Temperatures in Protoplanetary Disks." *Ann. Rev. Earth Planet. Sci.*, **26**(1), 53–80. doi:10.1146/annurev.earth.26.1.53

Burbine, T. H., McCoy, T. J., Meibom, A., Gladman, B. & Keil, K. (2002). "Meteoritic Parent Bodies: Their Number and Identification." In *Asteroids III*, pp. 653–667.

Butler, B. J., Muhleman, D. O. & Slade, M. A. (1993). "Mercury: full-disk radar images and the detection and stability of ice at the North Pole." *J. Geophys. Res.*, **98**(E8), 15003–15023. doi:10.1029/93JE01581

Campbell, B. A. (2002). *Radar Remote Sensing of Planetary Surfaces*, Cambridge University Press.

Campbell, B. A. (2016). "Planetary Geology with Imaging Radar: Insights from Earth-based Lunar Studies, 2001–2015." *Publ. Astron. Soc. Pac.*, **128**(964), 062001. doi:10.1088/1538-3873/128/964/062001

Campbell, B. A., Hawke, B. R., Morgan, G. A., Carter, L. M., Campbell, D. B. & Nolan, M. (2014). "Improved discrimination of volcanic complexes, tectonic features, and regolith properties in Mare Serenitatis from Earth-based radar mapping." *J. Geophys. Res. Planet.*, **119**(2), 313–330. doi:10.1002/2013JE004486

Carter, L. M., Campbell, D. B. & Campbell, B. A. (2011). "Geologic Studies of Planetary Surfaces Using Radar Polarimetric Imaging." *Proc. IEEE*, **99**(5), 770–782. doi:10.1109/JPROC.2010.2099090

Clark, R. N. (2009). "Detection of Adsorbed Water and Hydroxyl on the Moon." *Science*, **326**(5952), 562–564. doi:10.1126/science.1178105

Day, J. M. D. & Moynier, F. (2014). "Evaporative fractionation of volatile stable isotopes and their bearing on the origin of the Moon." *Phil. Trans. R. Soc. A*, **372**(2024), 20130259. doi:10.1098/rsta.2013.0259

DeMeo, F. E., Alexander, C. M. O., Walsh, K. J., Chapman, C. R. & Binzel, R. P. (2015). "The Compositional Structure of the Asteroid Belt." In P. Michel, F. E. DeMeo & W. F.

Bottke, eds., *Asteroids IV*, University of Arizona Press. doi:10.2458/azu_uapress_9780816532131-ch002

Deutsch, A. N., Neumann, G. A. & Head, J. W. (2017). "New evidence for surface water ice in small-scale cold traps and in three large craters at the north polar region of Mercury from the Mercury Laser Altimeter: Surface Water Ice on Mercury." *Geophys. Res. Lett.*, **44**(18), 9233–9241. doi:10.1002/2017GL074723

Drake, M. J. & Campins, H. (2005). "Origin of water on the terrestrial planets." *ACM Proc. IAU Symp.*, **1**(S229), 381–394. doi:10.1017/S1743921305006861

Elkins-Tanton, L. T. (2012). "Magma Oceans in the Inner Solar System." *Ann. Rev. Earth Planet. Sci.*, **40**(1), 113–139. doi:10.1146/annurev-earth-042711-105503

Fa, W. & Wieczorek, M. A. (2012). "Regolith thickness over the lunar nearside: Results from Earth-based 70-cm Arecibo radar observations." *Icarus*, **218**(2), 771–787. doi:10.1016/j.icarus.2012.01.010

Halliday, A. N. (2004). "Mixing, volatile loss and compositional change during impact-driven accretion of the Earth." *Nature*, **427**(6974), 505–509. doi:10.1038/nature02275

Harmon, J. K. & Slade, M. A. (1992). "Radar Mapping of Mercury: Full-Disk Images and Polar Anomalies." *Science*, **258**(5082), 640–643. doi:10.1126/science.258.5082.640

Hasegawa, S. (2003). "Evidence of hydrated and/or hydroxylated minerals on the surface of asteroid 4 Vesta." *Geophys. Res. Lett.*, **30**(21), 2123. doi:10.1029/2003GL018627

Hauri, E. H., Saal, A. E., Rutherford, M. J. & Van Orman, J. A. (2015). "Water in the Moon's interior: Truth and consequences." *Earth Planet. Sci. Lett.*, **409**, 252–264. doi:10.1016/j.epsl.2014.10.053

Hauri, E. H., Weinreich, T., Saal, A. E., Rutherford, M. C. & Van Orman, J. A. (2011). "High Pre-Eruptive Water Contents Preserved in Lunar Melt Inclusions." *Science*, **333**(6039), 213–215. doi:10.1126/science.1204626

Jawin, E. R., Kiefer, W. S., Fassett, C. I., Bussey, D. B. J., Cahill, J. T. S., Dyar, M. D., Lawrence, S. J. & Spudis, P. D. (2014). "The relationship between radar scattering and surface roughness of lunar volcanic features." *J. Geophys. Res. Planet.*, **119**(11), 2331–2348. doi:10.1002/2014JE004668

Keil, K. (2002). "Geological History of Asteroid 4 Vesta: The 'Smallest Terrestrial Planet.'" In *Asteroids III*, pp. 573–584.

Lawrence, D. J., Feldman, W. C., Goldsten, J. O., Maurice, S., Peplowski, P. N., Anderson, B. J., Bazell, D., McNutt, R. L., Nittler, L. R., Prettyman, T. H., Rodgers, D. J., Solomon, S. C. & Weider, S. Z. (2013). "Evidence for Water Ice near Mercury's North Pole from MESSENGER Neutron Spectrometer Measurements." *Science*, **339**(6117), 292–296. doi:10.1126/science.1229953

Li, S., Lucey, P. G., Milliken, R. E., Hayne, P. O., Fisher, E., Williams, J.-P., Hurley, D. M. & Elphic, R. C. (2018). "Direct evidence of surface exposed water ice in the lunar polar regions." *Proc. Natl. Acad. Sci. USA*, **115**(36), 8907–8912. doi:10.1073/pnas.1802345115

Lis, D. C., Biver, N., Bockelée-Morvan, D., Hartogh, P., Bergin, E. A., Blake, G. A., Crovisier, J., Val-Borro, M. de, Jehin, E., Küppers, M., Manfroid, J., Moreno, R., Rengel, M. & Szutowicz, S. (2013). "A Herschel Study of D/H in Water in the Jupiter-family Comet 45P/Honda-Mrkos-Pajdušáková and Prospects for D/H Measurements with CCAT." *Astrophys. J. Lett.*, **774**(1), L3. doi:10.1088/2041-8205/774/1/L3

Magri, C., Consolmagno, G. J., Ostro, S. J., Benner, L. A. M. & Beeney, B. R. (2001). "Radar constraints on asteroid regolith properties using 433 Eros as ground truth." *Meteorit. Planet. Sci.*, **36**(12), 1697–1709. doi:10.1111/j.1945-5100.2001.tb01857.x

Marty, B. (2012). "The origins and concentrations of water, carbon, nitrogen and noble gases on Earth." *Earth Planet. Sci. Lett.*, **313–314**, 56–66. doi:10.1016/j.epsl.2011.10.040

McCord, T. B., Taylor, L. A., Combe, J.-P., Kramer, G., Pieters, C. M., Sunshine, J. M. & Clark, R. N. (2011). "Sources and physical processes responsible for OH/H2O in the lunar soil as revealed by the Moon Mineralogy Mapper (M3)." *J. Geophys. Res. Planet.*, **116**(E6). doi:10.1029/2010JE003711

McSween, H. Y., Binzel, R. P., De Sanctis, M. C., Ammannito, E., Prettyman, T. H., Beck, A. W., Reddy, V., Le Corre, L., Gaffey, M. J., McCord, T. B., Raymond, C. A., Russell, C. T. & the Dawn Science Team. (2013). "Dawn; the Vesta-HED connection; and the geologic context for eucrites, diogenites, and howardites." *Meteorit. Planet. Sci.*, **48**(11), 2090–2104. doi:10.1111/maps.12108

McSween, H. Y., Mittlefehldt, D. W., Beck, A. W., Mayne, R. G. & McCoy, T. J. (2011). "HED Meteorites and Their Relationship to the Geology of Vesta and the Dawn Mission." *Space Sci. Rev.*, **163**(1), 141–174. doi:10.1007/s11214-010-9637-z

Milliken, R. E. & Li, S. (2017). "Remote detection of widespread indigenous water in lunar pyroclastic deposits." *Nat. Geosci.*, **10**(8), 561–565. doi:10.1038/ngeo2993

Morbidelli, A., Chambers, J., Lunine, J. I., Petit, J. M., Robert, F., Valsecchi, G. B. & Cyr, K. E. (2000). "Source regions and timescales for the delivery of water to the Earth." *Meteorit. Planet. Sci.*, **35**(6), 1309–1320. doi:10.1111/j.1945-5100.2000.tb01518.x

Morbidelli, A., Lunine, J. I., O'Brien, D. P., Raymond, S. N. & Walsh, K. J. (2012). "Building Terrestrial Planets." *Ann. Rev. Earth Planet. Sci.*, **40**(1), 251–275. doi:10.1146/annurev-earth-042711-105319

Ostro, S. J., Hudson, R. S., Benner, L. A. M., Giorgini, J. D., Magri, C., Margot, J.-L. & Nolan, M. C. (2002). "Asteroid Radar Astronomy." In *Asteroids III*, pp. 151–168.

Palmer, E. M., Heggy, E., Capria, M. T. & Tosi, F. (2015). "Dielectric properties of Asteroid Vesta's surface as constrained by Dawn VIR observations." *Icarus*, **262**, 93–101. doi:10.1016/j.icarus.2015.08.031

Palmer, E. M., Heggy, E. & Kofman, W. (2017). "Orbital bistatic radar observations of asteroid Vesta by the Dawn mission." *Nat. Commun.*, **8**(409). doi:10.1038/s41467-017-00434-6

Pieters, C. M., Ammannito, E., Blewett, D. T., Denevi, B. W., De Sanctis, M. C., Gaffey, M. J., Le Corre, L., Li, J.-Y., Marchi, S., McCord, T. B., McFadden, L. A., Mittlefehldt, D. W., Nathues, A., Palmer, E., Reddy, V., Raymond, C. A. & Russell, C. T. (2012). "Distinctive space weathering on Vesta from regolith mixing processes." *Nature*, **491**(7422), 79–82. doi:10.1038/nature11534

Pieters, C. M., Goswami, J. N., Clark, R. N., Annadurai, M., Boardman, J., Buratti, B., Combe, J.-P., Dyar, M. D., Green, R., Head, J. W., Hibbitts, C., Hicks, M., Isaacson, P., Klima, R., Kramer, G., Kumar, S., Livo, E., Lundeen, S., Malaret, E., McCord, T., Mustard, J., Nettles, J., Petro, N., Runyon, C., Staid, M., Sunshine, J., Taylor, L. A., Tompkins, S. & Varanasi, P. (2009). "Character and Spatial Distribution of OH/H2O on the Surface of the Moon Seen by M3 on Chandrayaan-1." *Science*, **326**(5952), 568–572. doi:10.1126/science.1178658

Prettyman, T. H., Mittlefehldt, D. W., Yamashita, N., Lawrence, D. J., Beck, A. W., Feldman, W. C., McCoy, T. J., McSween, H. Y., Toplis, M. J., Titus, T. N., Tricarico, P., Reedy, R. C., Hendricks, J. S., Forni, O., Le Corre, L., Li, J.-Y., Mizzon, H., Reddy, V., Raymond, C. A. & Russell, C. T. (2012). "Elemental Mapping by Dawn Reveals Exogenic H in Vesta's Regolith." *Science*, **338**(6104), 242–246. doi:10.1126/science.1225354

Reddy, V., Le Corre, L., O'Brien, D. P., Nathues, A., Cloutis, E. A., Durda, D. D., Bottke, W. F., Bhatt, M. U., Nesvorny, D., Buczkowski, D., Scully, J. E. C., Palmer, E. M., Sierks, H., Mann, P. J., Becker, K. J., Beck, A. W., Mittlefehldt, D., Li, J.-Y., Gaskell, R., Russell, C. T., Gaffey, M. J., McSween, H. Y., McCord, T. B., Combe, J.-P. & Blewett, D. (2012). "Delivery of dark material to Vesta via carbonaceous chondritic impacts." *Icarus*, **221**(2), 544–559. doi:10.1016/j.icarus.2012.08.011

Reddy, V., Dunn, T. L., Thomas, C. A., Moskovitz, N. A. & Burbine, T. H. (2015). "Mineralogy and Surface Composition of Asteroids." In P. Michel, F. E. DeMeo & W. F. Bottke, eds., *Asteroids IV*, University of Arizona Press. doi:10.2458/azu_uapress_9780816532131-ch003

Rivkin, A. S., Howell, E. S., Emery, J. P. & Sunshine, J. (2018). "Evidence for OH or H 2 O on the surface of 433 Eros and 1036 Ganymed." *Icarus*, **304**, 74–82. doi:10.1016/j.icarus.2017.04.006

Russell, C. T., Raymond, C. A., Coradini, A., McSween, H. Y., Zuber, M. T., Nathues, A., De Sanctis, M. C., Jaumann, R., Konopliv, A. S., Preusker, F., Asmar, S. W., Park, R. S., Gaskell, R., Keller, H. U., Mottola, S., Roatsch, T., Scully, J. E. C., Smith, D. E., Tricarico, P., Toplis, M. J., Christensen, U. R., Feldman, W. C., Lawrence, D. J., McCoy, T. J., Prettyman, T. H., Reedy, R. C., Sykes, M. E. & Titus, T. N. (2012). "Dawn at Vesta: Testing the Protoplanetary Paradigm." *Science*, **336**(6082), 684–686. doi:10.1126/science.1219381

Saal, A. E., Hauri, E. H., Cascio, M. L., Orman, J. A. V., Rutherford, M. C. & Cooper, R. F. (2008). "Volatile content of lunar volcanic glasses and the presence of water in the Moon's interior." *Nature*, **454**(7201), 192–195. doi:10.1038/nature07047

Saal, A. E., Hauri, E. H., Van Orman, J. A. & Rutherford, M. J. (2013). "Hydrogen Isotopes in Lunar Volcanic Glasses and Melt Inclusions Reveal a Carbonaceous Chondrite Heritage." *Science*, **340**, 1317–1320. doi:10.1126/science.1235142

Sarafian, A. R., Hauri, E. H., McCubbin, F. M., Lapen, T. J., Berger, E. L., Nielsen, S. G., Marschall, H. R., Gaetani, G. A., Righter, K. & Sarafian, E. (2017a). "Early accretion of water and volatile elements to the inner Solar System: evidence from angrites." *Phil. Trans. R. Soc. A*, **375**(2094). doi:10.1098/rsta.2016.0209

Sarafian, A. R., Nielsen, S. G., Marschall, H. R., Gaetani, G. A., Hauri, E. H., Righter, K. & Sarafian, E. (2017b). "Angrite meteorites record the onset and flux of water to the inner solar system." *Geochim. Cosmochim. Acta*, **212**, 156–166. doi:10.1016/j.gca.2017.06.001

Sarafian, A. R., Nielsen, S. G., Marschall, H. R., McCubbin, F. M. & Monteleone, B. D. (2014). "Early accretion of water in the inner solar system from a carbonaceous chondrite–like source." *Science*, **346**(6209), 623–626. doi:10.1126/science.1256717

Sarafian, A. R., Roden, M. F. & Patiño-Douce, A. E. (2013). "The volatile content of Vesta: Clues from apatite in eucrites." *Meteorit. Planet. Sci.*, **48**(11), 2135–2154. doi:10.1111/maps.12124

Schlichting, H. E., Sari, R. & Yalinewich, A. (2015). "Atmospheric mass loss during planet formation: The importance of planetesimal impacts." *Icarus*, **247**, 81–94. doi:10.1016/j.icarus.2014.09.053

Schorghofer, N. (2008). "The Lifetime of Ice on Main Belt Asteroids." *Astrophys. J.*, **682**(1), 697–705. doi:10.1086/588633

Shearer, C. K., Burger, P. V., Papike, J. J., Sharp, Z. D. & McKeegan, K. D. (2011). "Fluids on differentiated asteroids: Evidence from phosphates in differentiated meteorites GRA 06128 and GRA 06129." *Meteorit. Planet. Sci.*, **46**(9), 1345–1362. doi:10.1111/j.1945-5100.2011.01233.x

Slade, M. A., Butler, B. J. & Muhleman, D. O. (1992). "Mercury Radar Imaging: Evidence for Polar Ice." *Science*, **258**(5082), 635–640. doi:10.1126/science.258.5082.635

Spudis, P. D., Bussey, D. B. J., Baloga, S. M., Cahill, J. T. S., Glaze, L. S., Patterson, G. W., Raney, R. K., Thompson, T. W., Thomson, B. J. & Ustinov, E. A. (2013). "Evidence for water ice on the Moon: Results for anomalous polar craters from the LRO Mini-RF imaging radar." *J. Geophys. Res. Planet.*, **118**(10), 2016–2029. doi:10.1002/jgre.20156

Starukhina, L. (2001). "Water detection on atmosphereless celestial bodies: Alternative explanations of the observations." *J. Geophys. Res. Planet.*, **106**(E7), 14701–14710. doi:10.1029/2000JE001307

Sunshine, J. M., Farnham, T. L., Feaga, L. M., Groussin, O., Merlin, F., Milliken, R. E. & A'Hearn, M. F. (2009). "Temporal and Spatial Variability of Lunar Hydration As Observed by the Deep Impact Spacecraft." *Science*, **326**(5952), 565–568. doi:10.1126/science.1179788

Taylor, J. (2009). *Dawn Telecommunications* (DESCANSO Article No. 13), Pasadena, California: NASA Jet Propulsion Laboratory, California Institute of Technology.

Treiman, A. H., Lanzirotti, A. & Xirouchakis, D. (2004). "Ancient water on asteroid 4 Vesta: evidence from a quartz veinlet in the Serra de Magé eucrite meteorite." *Earth Planet. Sci. Lett.*, **219**(3–4), 189–199. doi:10.1016/S0012-821X(04)00004-4

Warren, P. H., Rubin, A. E., Isa, J., Gessler, N., Ahn, I. & Choi, B.-G. (2014). "Northwest Africa 5738: Multistage fluid-driven secondary alteration in an extraordinarily evolved eucrite." *Geochim. Cosmochim. Acta*, **141**, 199–227. doi:10.1016/j.gca.2014.06.008

CHAPTER II

DIELECTRIC PROPERTIES OF ASTEROID VESTA'S SURFACE AS CONSTRAINED BY DAWN VIR OBSERVATIONS

Palmer, E. M., Heggy, E., Capria, M. T. & Tosi, F. (2015). *Icarus*, **262**, 93–101.
doi:10.1016/j.icarus.2015.08.031

1. Abstract

Earth and orbital-based radar observations of asteroids provide a unique opportunity to characterize surface roughness and the dielectric properties of their surfaces (i.e., their relative permittivity), as well as potentially explore some of their shallow subsurface physical properties. If the dielectric and topographic properties of asteroid's surfaces are defined, one can constrain their surface textural characteristics as well as potential subsurface volatile enrichment using the observed radar backscatter. To achieve this objective, we establish the first dielectric model of asteroid Vesta for the case of a dry, volatile-poor regolith—employing an analogy to the dielectric properties of lunar soil, and adjusted for the surface densities and temperatures deduced from Dawn's Visible and InfraRed mapping spectrometer (VIR). Our model suggests that the real part of the dielectric constant (i.e., real permittivity) at the surface of Vesta is relatively constant, ranging from 2.3 to 2.5 from the night- to day-side of Vesta, while the loss tangent shows slight variation as a function of diurnal temperature, ranging from 6×10^{-3} to 8×10^{-3}. We estimate the surface porosity to be ~55% in the upper meter of the regolith, as derived from VIR observations. This is ~12% higher than previous estimation of porosity derived from previous Earth-based S- (2.3 GHz) and X-band (8.4 GHz) radar observations. We suggest that the radar backscattering properties of asteroid Vesta will be mainly driven by the changes in surface roughness rather than potential dielectric variations in the upper regolith in the S- and X-band.

2. Introduction

NASA's Dawn mission is targeting two uniquely large asteroids for orbital investigation, Vesta and Ceres, which are thought to be remnant building blocks of the terrestrial planets (Russell et al., 2011). The structural and textural properties of asteroids are observed primarily using Earth-based radar, and provide insight into the processes that shaped their surfaces: whether through impact cratering, lava flows, or stress fracturing as a result of the diurnal thermal erosion arising from the expansion and contraction of volatiles embedded in the surface material. The first target of the Dawn mission, Vesta, was expected to have depleted its volatile content long ago through global melting, differentiation, and later regolith gardening by impacts from smaller bodies (Russell et al., 2011). However, multiple observations from Dawn's year-long orbital mission point to the ephemeral presence of volatiles: localized hydrogen concentrations in regions thought to contain impactor-delivered hydrated materials (Prettyman et al., 2012; Reddy et al., 2012), widespread hydroxyl absorption bands across the surface (De Sanctis et al., 2012b), pitted terrain in some crater floors, thought to be caused by the degassing of subsurface volatiles (Denevi et al., 2012), and gullies in crater walls that are morphologically consistent with formation by transient fluid flow (Scully et al., 2015).

Given radar's ability to resolve a target's overall shape and centimeter- to decimeter-scale surface roughness, and its ability to assess the potential presence of ice through polarimetric ratios (e.g., Thompson, Ustinov & Heggy, 2011; Thompson et al., 2012), radar is a particularly useful technique for aiding in the volatile investigation of Vesta's surface and that of other small bodies. Earth-based and orbital radar studies of the Moon, for example, have revealed potential sites of ice concentration at the poles (e.g., Spudis et al., 2010), while Earth-based radar observations of Mercury have provided the first detection of water ice in permanently shadowed craters (Slade, Butler & Muhleman, 1992). For asteroids, Earth-based radar is predominantly used for detection purposes, yielding shape, spin and qualitative surface roughness from delay-Doppler imaging (Ostro et al., 2002). Vesta has likewise been observed at a number of radar frequencies: the X-band (8.4 GHz) at Goldstone and S-band (2.3 GHz) at Arecibo (e.g., Mitchell et al., 1996), as well as the Ku- (15 GHz) and C-bands (4.9 GHz) with the Very Large Array (VLA) (Johnston et al., 1989).

The results of such radar observations, however, are difficult to translate into quantifiable surface physical properties, as the power and polarization of the returned radar backscatter are affected by the observing geometry (which is easily constrained) and by three intrinsic factors of the surface: (1) variations in the surface topography, (2) variations in surface roughness, and (3) variations in the surface's complex dielectric properties (i.e., its relative permittivity)—which describes the radar reflectivity and absorptivity of a material, and is primarily dependent on the mineralogy, bulk density, temperature and volatile content of the surface material (e.g., Heggy et al., 2001; Paillou et al., 2006; Heggy & Palmer et al., 2012). While the effect of the surface topography of small bodies can be modeled from a shape model (which in turn can be derived from speckle interferometry—i.e., using the interference pattern produced by to model the meter-scale topography of the body—photometric lightcurves or stereoscopic images), surface roughness and surface dielectric properties remain poorly characterized. As a consequence, when measuring the radar backscatter from the surface of a small body, it is challenging to determine whether backscatter variations are caused by variations in surface roughness or variation in the surface's dielectric properties. The ability to construct a quantifiable surface roughness map, and subsequently to identify regions that are smooth at decimeter scales, is critical to the success of future small-body landing missions (e.g., Asphaug 2006) and future sampling experiments (ElShafie & Heggy, 2013).

This difficulty is exemplified by Mitchell et al. (1996), who used radar Doppler spectra to qualitatively infer that Vesta's surface is overall rougher than the Moon at both decimeter and centimeter scales. While they used a shape model (derived from speckle interferometry) to constrain the topographic component of the total radar backscatter, they did not estimate the backscatter contribution that arises from potential variations in the surface's dielectric properties—which are widely used to assess the textural and compositional uncertainties of a surface (e.g., Boisson et al., 2009 & 2011). On the Moon, the ability to quantify dielectric properties has proven significant for identifying distinctions between the two types of lunar terrain, the highlands and the lunar *maria* (Fa & Wieczorek, 2012).

One study that attempts to estimate the dielectric properties of Vesta's surface is conducted by Johnston et al. (1989), who find that the Ku- and C-band microwave emissions from Vesta are in disagreement with those expected of a rotating blackbody. They suggest that the asteroid may be covered by a thin layer of dust that decreases microwave reflectivity, thereby increasing the body's microwave brightness. When estimating the thickness of this layer, they rely on dielectric mixing models of generic powdered rock (discussed by Campbell & Ulrichs (1969)), and suggest a depth of

6 cm when assuming a value of 2.9 for the real part of the relative dielectric constant ε' and assuming 1.5×10^{-2} for the loss tangent tan δ—where ε' relates to the material's reflectivity and tan δ to the material's attenuation of energy. Johnston et al.'s (1989) value of ε', however, is inconsistent with dielectric laboratory measurements of powdered basaltic samples near the same bulk density of 1.00 g cm^{-3} (e.g., Campbell & Ulrichs, 1969; Alvarez, 1974). When considered alongside the study of Mitchell et al. (1996), both results suggest that there is a substantial ambiguity regarding the textural and dielectric properties of Vesta's surface, as well as in the method used to quantify them from Earth-based radar observation.

With the Dawn mission, however, an opportunity arises to address this deficiency. In this study, thermal observations by Dawn's Visible and InfraRed (VIR) mapping spectrometer are used to constrain the bulk density and temperatures of the surface, which are the main parameters that determine the surface's dielectric properties for a desiccated planetary regolith (Thompson, Ustinov & Heggy, 2011). Our dielectric model is constructed specifically for the dry, volatile-poor case of Vesta's surface, given that the highest hydrogen concentration observed by Dawn's GRaND instrument is 400 ppm or 0.04 wt.% (Prettyman et al., 2012), which is well below the radar detectability limit of at least 10% of ice content (for which solid water-ice has $\varepsilon' \approx 3.1$) mixed in basaltic desiccated lunar-like soils (Fa, Wieczorek & Heggy, 2011). This model allows us to assess the expected range of dielectric properties arising from potential surface compositional variations (as described by De Sanctis et al., 2012a & 2013), as well as from variations in surface temperature and density (as described by Tosi et al., 2014 & Capria et al., 2014). It should be noted, however, that water-ice may exist below the depths that are observed by GRaND, i.e., below ~1 m. Furthermore, the size of GRaND's footprint covers ~10% of the asteroid's surface (Prettyman et al., 2012), such that localized ice deposits may also be present at shallower depths that are not resolved by GRaND. Hence, the dielectric model of a desiccated Vestan surface is representative of low hydrogen concentrations on the global scale.

Since the dielectric properties of asteroid analog materials have yet to be measured in the laboratory, we use existing dielectric studies of lunar soil samples to serve as suitable analogs to Vesta's upper regolith material. The compositional analogy between Vesta's surface material and basaltic lunar soil is addressed in Sections 2.1 and 2.2, and the assumptions and limitations of the resulting surface dielectric model are considered in Sections 2.3 and 2.4. Section 3 contains the results of the dielectric model for Vesta's surface, and includes suggested validation sites where the dielectric constant of Vesta's surface may be estimated from future in-situ radar observations. In Section 4, the implications of our findings are discussed for existing and future Earth- and space-based radar studies of Vesta and other asteroids, with emphasis on volatile detectability. Overall, this dielectric model is an essential step toward retrieving quantifiable surface roughness from radar backscatter measurements by Earth-based and orbital S- and X-band radar observations (e.g., Mitchell et al., 1996; Nolan et al., 2005), which will develop understanding of the processes that govern Vesta's surface texture, as well as support the planning of potential future landing and sampling experiments, such as NASA's Origins-Spectral Interpretation-Resource Identification-Security-Regolith Explorer, OSIRIS-REx (Lauretta et al., 2014).

3. Dielectric Model Construction and Parameter Constraint

The dielectric properties of a material describes the intrinsic mechanisms by which the material reflects and attenuates the electric field component of the incident radar wave, and is quantified by the complex relative dielectric constant, i.e., complex relative permittivity ($\varepsilon_r = \varepsilon_r' + i\varepsilon_r''$). For brevity, the relative dielectric constant ε_r (a dimensionless quantity) is hereon referred to as the dielectric constant. As previously mentioned, the real part of the dielectric constant, ε', relates to the reflectivity of the material, while the ratio of the imaginary part to the real part ($\varepsilon''/\varepsilon'$) is termed the loss tangent (tan δ), and quantifies the loss of energy during transmission through a given material (such as Vesta's regolith). For small desiccated terrestrial bodies, including the Moon and Mercury, the dielectric properties of the surface mainly depend on the material's (1) mineralogy, (2) bulk density, (3) diurnal surface temperature, (4) potential volatile content (e.g., Heggy & Palmer et al., 2012), and (5) frequency, which falls in the range of 2–8 GHz for Earth-based radar observations. In the following sections, the first four of these geophysical parameters are constrained for the material of Vesta's upper regolith using observations by the Dawn VIR spectrometer. In Section 3, these constraints are utilized to construct a numerical model of ε' and tan δ for the general case of a volatile-poor, dry surface and shallow subsurface of Vesta.

3.1. Surface Mineralogy

Vesta has been identified as the parent body of basaltic, achondritic meteorites (howardites, eucrites and diogenites; "HEDs") through extensive meteoritic studies and Earth-based spectral observations of asteroids (Takeda, 1997; Hiroi, Pieters & Takeda, 1994). As confirmed by hyperspectral observations from Dawn's VIR instrument (De Sanctis et al., 2012a & 2013), the composition of Vesta's upper regolith is analogous to that of howardite—a brecciated material formed by clasts of eucrite and diogenite in varying ratios.

The surface contains a heterogeneous distribution of eucrite-rich versus diogenite-rich howardite (e.g., De Sanctis et al., 2013), where the primary mineralogical difference between eucrites and diogenites is in the pyroxene composition and content. Eucrites are primarily composed of low-Ca pyroxene and plagioclase, while diogenites contain a high abundance of low-Ca, Mg-rich pyroxene with only minor amounts of plagioclase (e.g., Burbine et al., 2001).

The above-described surface mineralogy is expected to provide minimal dielectric variation on the surface of Vesta. For instance, dielectric measurements of lunar samples by Olhoeft and Strangway (1975)—consisting of the same major minerals as HEDs at varying concentrations—suggest that the real part of the dielectric constant (ε') is mainly a function of the bulk density, and shows no substantial variation with composition among the lunar basaltic minerals commonly found in HEDs. While the loss tangent of lunar samples varies with ilmenite content (Carrier, Olhoeft & Mendell, 1991), howardite, eucrite and diogenite samples in the NASA Johnson Space Center's HED meteorite compendium each contain only minor, accessory amounts of ilmenite ($\leq$ 1.5%) (Righter & Garber, 2011). The above suggests that Vesta's surface can be expected to be dielectrically homogeneous when considering the effect of composition on the dielectric properties of the regolith. Furthermore, given the extensive gardening of regolith by meteoritic impacts, the upper few meters of the Vestan regolith are also expected to be compositionally homogeneous with depth (Pieters et al., 2012) and hence the effect of composition on vertical dielectric variation in the first few meters can be neglected.

3.2. Compositional Analogy to Lunar Soil

While Vesta's surface mineralogy is consistent with howarditic dust, howardite has yet to be dielectrically characterized through laboratory study. In order to estimate Vesta's dielectric properties for given conditions of surface density and temperature, one must identify an analog material that has been sufficiently dielectrically characterized under Vesta's relevant surface conditions.

We hypothesize that basaltic lunar soil is the most suitable compositional analog to the Vestan regolith. Both lunar soil and regolithic howardites are brecciated basalts—gardened by meteoritic impacts and composed primarily of pyroxenes and plagioclase (Papike, Taylor & Simon, 1991; Warren et al., 2009)—and originate from airless, desiccated regoliths unlike Earth or martian basalts. Furthermore, lunar soil samples have been measured extensively in the laboratory for dielectric variation over a wide range of radar frequencies, for various bulk densities (e.g., Olhoeft & Strangway, 1975), at low temperatures, and in vacuum, relevant to planetary conditions (e.g., Alvarez, 1974).

Lunar soil and regolithic howardite differ in their minor mineralogy (Cartwright et al., 2013), but unless one such mineral has a significantly high dielectric constant (e.g., iron oxide minerals) compared to that of the major host minerals, its presence does not measurably alter the bulk material's dielectric constant (Campbell et al., 2002). Ilmenite content in lunar soils, for example, will increase the loss tangent of the material with increasing volume fraction (Carrier, Olhoeft & Mendell, 1991). Among the collection of HED meteorites curated by NASA Johnson Space Center (JSC), however, total ilmenite content is less than 1.5% and is typically found as only an accessory mineral in HED meteorites (Righter & Garber, 2011). The lunar samples selected for this study (Section 2.3) are also low in ilmenite content (<1.5%) (Meyer, 2010a, 2010b; Hill et al., 2007), further supporting the analogy between the dielectric properties of lunar soil with that of Vesta's surface material.

Vesta's regolith also undergoes different space weathering than on the Moon, such that Vesta's regolith has a lower noble gas content (Cartwright et al., 2013), and lacks nanophase iron (Pieters et al., 2012). Noble gas content, however, provides a negligible contribution to the dielectric properties of a soil (Olhoeft & Strangway, 1975), and Barmatz et al. (2012) find no dependence of dielectric properties on the fraction of nanophase iron in lunar soil samples.

For the construction of the dielectric model of Vesta's surface, we hence conclude that basaltic lunar soil is a suitable analog to the bulk composition of Vesta's upper regolith.

3.3. Surface Density and Diurnal Temperature Variation

As discussed above for Vesta's surface, the spatial and temporal variation of the dielectric constant is expected to be primarily dependent on bulk density and secondarily dependent on temperature. In order to constrain the surface density and diurnal temperature variation of Vesta's regolith, we use the results of Capria et al. (2014), who model heat transfer in the upper 50 meters of Vesta's regolith by balancing solar input energy with output surface radiation. The Capria et al. (2014) thermophysical model accounts for (1) the thermal conductivity profile of the upper regolith (which depends on the best-fit density profile and temperature profile in the subsurface), as well as (2) the local sub-pixel surface topography (which suppresses the output surface radiation with increasingly rough terrain, and leads to an increase in local surface temperature).

Capria et al. (2014) ultimately deduce surface densities that provide the best fits between theoretical diurnal surface temperatures, and ones directly retrieved from VIR observations (Tosi et al., 2014). Their results are expressed as a map of regionally-averaged thermal inertia values, which quantify the resistance of a material to variations in its diurnal temperature (Capria et al., 2014). Regions with the most diurnal temperature change correspond to surfaces of low thermal inertia, which can be explained by fine, low-density material. While VIR is only sensitive to temperatures $\geq$180 K (Tosi et al., 2014), the thermophysical model of Capria et al. (2014) estimates the full range of day-to-night surface temperatures throughout a diurnal cycle. Temperatures retrieved from VIR observations ($\geq$ 180 K) are used to constrain daytime temperatures, while ESA's Herschel IR observations provide constraints on cooler and nighttime temperatures (Leyrat et al., 2012). Capria et al.'s (2014) thermophysical model additionally provides a best-fit surface density for each modeled region of Vesta's surface.

On average, Capria et al. (2014) find a best-fit surface density of ~1.30 g cm^{-3}, with local variations on the order of $\pm$ 0.10 g cm^{-3}. For the purpose of this study, in which surface bulk density and surface temperatures are used as input to the surface dielectric model, Capria (this study) provides a global map of theoretical surface temperatures for a given time in Vesta's rotation (Figure 1) using the globally-averaged surface density of 1.30 g cm^{-3}. A full description of the procedure for determining best-fit surface densities and diurnal temperature curves is detailed by Capria et al. (2014).

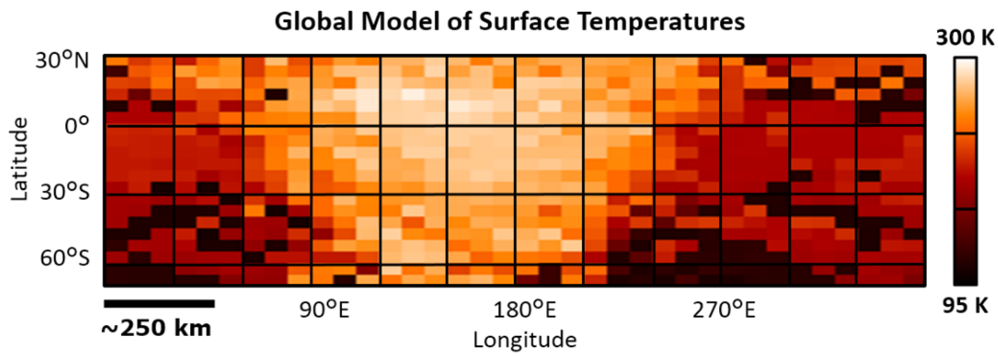

Figure 1. Global model of surface temperatures on Vesta. The map has a resolution of 5° latitude by 10° longitude per pixel. The map corresponds to an average best-fit surface density of 1.30 g cm^{-3} with a sub-solar point of (26.7°S, 160.6°E) at a Vesta-Sun distance of ~2.1 AU. Modeled temperatures range from 98 to 280 K, where those below 180 K bear the most uncertainty, on the order of tens of K. Results are given from 70°S to 30°N due to the limited availability of albedo values derived from *Approach Phase* data.

3.4. Dielectric Properties of Vestan Analog Material

In Section 2.2, we proposed basaltic lunar soil to be a suitable compositional analog to Vesta's surface material, and in Section 2.3 used VIR observations to determine a range of surface bulk densities and temperatures over which to provide an estimate of the dielectric properties (the relative permittivity) of Vesta's upper regolith. Three dielectric studies that sufficiently meet our criteria for relevant measurement conditions are those of Alvarez (1974), Frisillo, Olhoeft & Strangway (1975), and Bussey (1979), who each conducted dielectric laboratory studies on basaltic lunar fines from Apollo 17 (samples 74241, 72441 and 70051, respectively) under vacuum to ensure a totally desiccated sample, at temperatures below 300 K, and with sample bulk densities between ~1.30 g cm^{-3} and ~1.80 g cm^{-3}. Unfortunately, few other Apollo lunar soil samples were protected against atmospheric moisture contamination, which measurably alters the dielectric constant (Olhoeft, Strangway & Pearce, 1975; Heggy et al., 2001), and few were measured in vacuum conditions, limiting the use of additional lunar sample dielectric studies for the Vestan case.

While the dielectric measurements of Alvarez (1974), Frisillo, Olhoeft & Strangway (1975) and Bussey (1979) have each been conducted at frequencies below the 2–8 GHz range as used by Earth-based radar observations, desiccated basalts that lack iron-oxide minerals are non-dispersive dielectric materials over the MF, HF, VHF, UHF and SHF radio frequency range, with no observed relaxations over 0.1 MHz to 8 GHz when performing a dielectric spectroscopic characterization (Carrier, Olhoeft & Mendell, 1991; Heggy et al., 2007; Brouet et al., 2014). Since (1) the modal content of ilmenite, an iron oxide mineral common in lunar regolith, is less than 1.5% in each of the three lunar soil samples, and also in each of the HED meteorites in the NASA JSC collection, and (2) samples are totally desiccated, there is no sufficient presence of conductive ions to cause a measurable frequency dependence behavior in both the real and imaginary part of the dielectric constant as measured across the dipolar polarization regime of the electromagnetic spectrum. One can therefore safely apply the dielectric measurements of Alvarez (1974) at 0.1 MHz, of Frisillo, Olhoeft & Strangway (1975) at 0.1 MHz, and of Bussey (1979) at 1.6 GHz to S- (2.3 GHz) and X-band (8.4 GHz) radar frequencies.

Table 1 summarizes the dielectric measurements of the three selected lunar soil samples. Alvarez (1974) compacted soil sample 74241 to a bulk density of 1.38 g cm^{-3}, and under vacuum conditions, measured ε' and tan δ at successive temperatures of 100, 298 and 373 K. The procedure was repeated when the sample was compacted to 1.61 g cm^{-3}. At each given temperature, ε' and tan δ were measured in the frequency range of 30 Hz to 0.1 MHz. Values reported in Table 1, and used in the construction of our dielectric model, correspond to those measured at the maximum frequency of 0.1 MHz, at which ε' ranges from 2.18 to 2.42, and tan δ ranges from 1.2×10^{-2} to 1.7×10^{-2}.

The dielectric measurements of Frisillo, Olhoeft & Strangway (1975) were conducted similarly on lunar soil sample 72441 at sample bulk densities of 1.56, 1.65 and 1.80 g cm^{-3}. Each measurement of ε' and tan δ were conducted under vacuum, over the frequency range of 100 Hz to 0.1 MHz, and at temperatures of 298, 323, and 373 K. Their measurements yielded ε' between 3.04 and 3.27, and tan δ between 4×10^{-3} and 7×10^{-3}. Again, values of ε' and tan δ reported in Table 1 correspond to the maximum frequency of measurement by Frisillo, Olhoeft & Strangway (1975) at 0.1 MHz.

Table 1. Dielectric properties of lunar soil samples used as compositional analogs to model the dielectric properties of Vesta's surface.

Sample	Reference	Frequency	Bulk Density (g cm^{-3})	Temperature (K)	ε'	tan δ	Ilmenite Content (wt.%)
74241	Alvarez (1974)	100 kHz	1.38	100	2.18	0.012	1.3 [a]
			1.38	298	2.20	0.014	1.3
			1.38	373	2.28	0.016	1.3
			1.61	100	2.34	0.012	1.3
			1.61	298	2.38	0.015	1.3
			1.61	373	2.42	0.017	1.3
72441	Frisillo, Olhoeft & Strangway (1975)	100 kHz	1.56	298	3.04	0.004	0.3 [b]
			1.56	323	3.05	0.004	0.3
			1.56	373	3.09	0.005	
			1.65	298	3.13	0.004	0.3
			1.65	323	3.13	0.005	0.3
			1.65	373	3.16	0.006	
			1.8	298	3.27	0.005	0.3
			1.8	323	3.27	0.005	0.3
			1.8	373	3.28	0.005	
70051	Bussey (1979)	1.6 GHz	1.6	173	3.30	0.005	2.8 [c]
			1.6	232	3.34	0.006	2.8
			1.6	296	3.42	0.007	2.8
			1.6	373	3.42	0.008	2.8

[a] Meyer (2010a)
[b] Meyer (2010b)
[c] Hill et al. (2007)

In the third study, Bussey (1979) measured the dielectric properties of sample 70051 at a fixed bulk density of ~1.60 g cm^{-3} over the frequency range of 500 MHz to 10 GHz, and at temperatures of 173, 232, 296 and 373 K under vacuum. The dielectric properties reported in Table 1, however, correspond to measurements at 1.6 GHz rather than 10 GHz, as Bussey (1979) states that measurements above this threshold were unreliable due to instrumental error. Bussey's (1979) measurements of ε' and tan δ for sample 70051 range from 3.30 to 3.42 and 5×10^{-3} to 8×10^{-3}, respectively.

In order to extrapolate the measurements of Alvarez (1974), Frisillo, Olhoeft & Strangway (1975) and Bussey (1979) to the relevant densities and temperatures of Vesta's regolith, we apply an iterative, multivariable least-squares fit to the data in Table 1 to determine empirical formulas for both the real part ε' of the dielectric constant and the loss tangent tan δ of the lunar samples as functions of bulk density and temperature (Markwardt, 2009). We fit a power-law to the density dependence of ε', and find a minor dependence of ε' on temperature, consistent with dielectric laboratory measurements of other lunar samples (e.g., Olhoeft & Strangway, 1975). The loss tangent of the lunar samples follows an exponential dependence on temperature, and exhibits no apparent density dependence between 1.38 g cm^{-3} and 1.80 g cm^{-3} among the three selected lunar samples.

The resulting best-fit empirical formulas to the dielectric properties of the three selected lunar soil samples are as follows:

$$\varepsilon'(\rho, T) = (1.85 \pm 0.02)^{\rho} + (8 \pm 1)\times 10^{-4} T \tag{1}$$

$$\tan\delta(T) = (5.1 \pm 0.2)\times 10^{-3} \exp\{(1.7 \pm 0.2)\times 10^{-3} T\} \tag{2}$$

where ε' is the real part of the dielectric constant of dry, basaltic soil that lacks significant iron-oxide content; tan δ is its loss tangent; T (K) is the soil's temperature; and ρ (g cm^{-3}) is the bulk density of the soil. This dielectric model is applicable over the range of ~1.20 g cm^{-3} to 1.80 g cm^{-3} for desiccated basaltic soil, as constrained by the range of bulk densities measured in the dielectric studies of Alvarez (1974), Frisillo, Olhoeft & Strangway (1975) and Bussey (1979). The base of the exponent (1.85) in Equation 1 is comparable to that reported by Olhoeft & Strangway (1975), who compiled 92 measurements of the dielectric constant vs. density of lunar samples, and found the base of the exponent to be 1.93 ± 0.17. Notably, their selection criteria were less strict, as they included many studies of lunar soils that were measured under ambient atmosphere, and therefore exposed to moisture contamination, which measurably impacts both ε' and tan δ (Olhoeft, Strangway & Pearce, 1975; Heggy et al., 2001). The small temperature dependence and lack of density dependence in the loss tangent (Equation 2) also agree with the findings of Olhoeft & Strangway (1975). Using these empirical formulas as estimates for the dielectric properties of Vesta's surface, maps of ε' and tan δ are constructed for a given time in the asteroid's rotation (displayed in Figure 2) and use, as inputs, the modeled surface temperatures of Vesta from Figure 1, which range from 98 to 280 K, and the average best-fit surface bulk density of 1.30 g cm^{-3}.

4. Dielectric Model of a Volatile-Free Surface

4.1. Average Near-Surface Dielectric Properties

Figure 2 shows the resulting global model of ε' (top panel) and tan δ (bottom panel) for Vesta's surface at a spatial resolution of 5° latitude by 10° longitude per pixel. Along the equator, this corresponds to a spatial resolution of ~5 by 10 km/pixel. Illumination conditions during the *Approach Phase* of the Dawn mission limit the derivation of surface albedos to latitudes between 70°S and 30°N (Li et al., 2013), and thereby confine both the thermal inertia calculations of Capria et al. (2014) and the dielectric model in this study to the same latitude range.

For S- and X-band radar observations, we report two sets of dielectric properties: (1) those of the surface and near-surface (i.e. ~1-2 wavelengths deep), which corresponds to the surface average bulk density of ~1.30 g cm^{-3}, and (2) the dielectric properties in the potential case of penetration depth of up to ~10 wavelengths, which corresponds to the upper meter of regolith (Campbell, 2002; Thompson, Ustinov & Heggy, 2011). We use the same subsurface density-depth profile that was hypothesized in the thermophysical model of Capria et al. (2014), which is that of the lunar regolith given by Carrier, Olhoeft & Mendell (1991). This yields a maximum bulk density of ~1.80 g cm^{-3} at one meter depth.

Using these two bulk densities as inputs to Equation 1, and accounting for the VIR observed range of diurnal temperatures at the surface ranging from 98 to 280 K, ε' is calculated to vary from 2.31 to 2.47 at the surface, and to vary from ~3.10 to 3.25 at one meter depth. For the loss tangent, the diurnal effect leads to a range of 6×10^{-3} to 8×10^{-3} respectively between the night and day side.

In regions of anomalously high or low thermal inertia values, which Capria et al. (2014) attribute mainly to a difference in surface bulk density (± 0.10 g cm^{-3}), ε' is expected to deviate ≤ 9% from the mean, based on the empirical model in Equation 1. At the relatively coarse spatial resolution of both the temperature and associated dielectric maps, these deviations are smoothed out, and the average surface density of 1.30 g cm^{-3} can be considered uniform in the construction of our surface dielectric model.

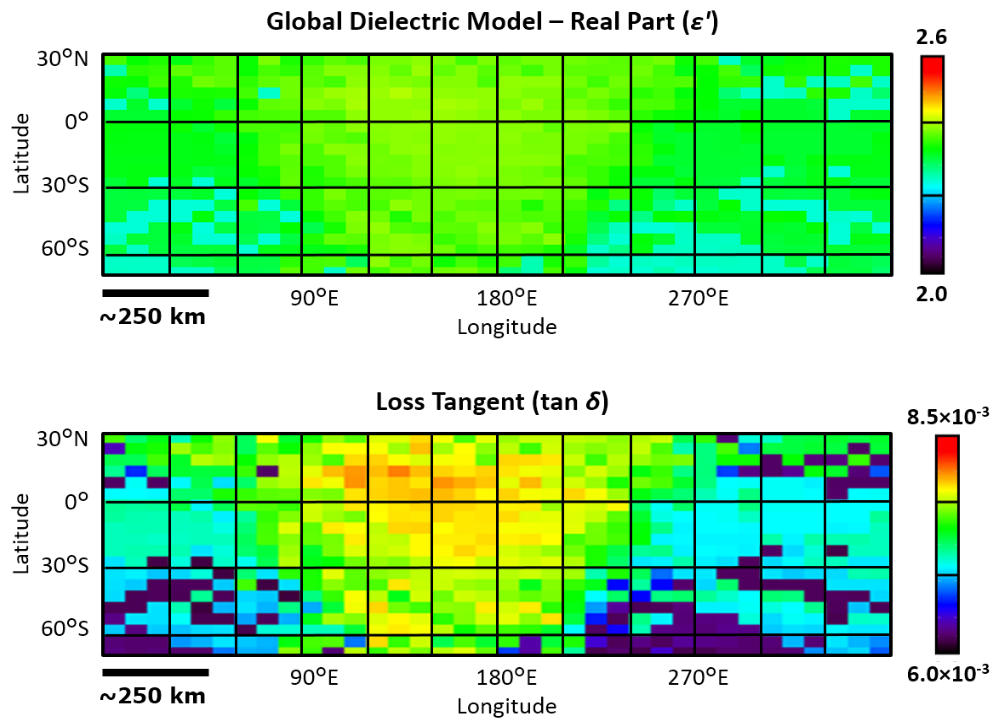

Figure 2. Global dielectric model of ε' (top) and tan δ (bottom) on Vesta's surface. Results are applicable at S- and X-band frequencies (2.3 GHz and 8.4 GHz, respectively), where each map has a resolution of 5° latitude by 10° longitude per pixel. Calculations assume a best-fit surface density of 1.30 g cm^{-3}. The sub-solar point is at (26.7°S, 160.6°E) with a Vesta-Sun distance of ~2.1 AU. Results are evaluated between 70°S and 30°N due to the availability of *Approach Phase* data, where ε' ranges between 2.3 and 2.5, and tan δ from 6.0×10^{-3} to 8.3×10^{-3}. In areas of lower thermal inertia (potentially lower density) below the resolution of this map, our model suggests ε' ~ 2.2 to 2.3, and in areas of higher thermal inertia (higher density), ε' ~ 2.3 to 2.5.

4.2. Vesta's Surface Dielectric Calibration Sites

In order to provide means for future validation of this dielectric model, four sites of ~1 km^2 are identified on the Vestan surface that have low roughness at ~20 m resolution, as defined from high-resolution imagery acquired by Dawn's framing camera (FC) during Low-Altitude Mapping Orbit (LAMO). Figure 3 shows the high-resolution framing camera images of the validation sites and their locations with respect to Vesta's global map. Figure 4 shows surface temperatures in each location as retrieved from VIR thermal imagery, as well as their surface dielectric properties as assessed from our empirical model in Equations 1 and 2.

Each site is consistent with a location of accumulation of fine-grained material, and is, furthermore, likely to be texturally smooth to the scale of meters (Jaumann et al., 2012). Radar backscatter from planetary regolith depends on both the surface roughness and the material's dielectric constant (e.g., Fa, Wieczorek & Heggy, 2011; Hagfors, 1964), hence by selecting sites of low surface roughness—characteristically flat, crater-free and smooth (i.e. lacking shadows)—this minimizes the ambiguity associated with deriving the surface's dielectric properties from the observed radar backscatter, as they must be disentangled from the scattering effects of surface roughness using inversion models (Tabatabaeenejad & Moghaddam, 2009). While Earth-based radar observations of Vesta are constrained to an imaging resolution on the order of 10-100 km (Nolan et al., 2005), and are thereby unable to resolve such sites, future flyby and orbital missions to Vesta, for instance, can estimate the surface's dielectric constant from bistatic radar observations of the backscatter from these low-roughness locations (e.g., Simpson, 2011).

Site 4 is located in a region consistent with ponded (i.e., flat, fine-grained) crater ejecta material (labeled "Zone B" in Figure 3), and is centered on (22°S, 268°E) based on longitudes expressed in the Dawn Claudia coordinate system (Russell et al., 2012; Roatsch et al., 2012; Li et al., 2013). Surface temperatures in Zone B were retrieved from two VIR infrared images (~170 m/pixel resolution) that overlapped Site 4, and range from ~210-265 K. Using the average best-fit surface density of Capria et al. (2014) and the lunar density-depth profile of Carrier, Olhoeft & Mendell (1991), our dielectric model suggests that at the surface, ε' is relatively constant at 2.4, and tan $\delta \sim 7.6\times10^{-3}$ to 8.0×10^{-3}. For the upper meter of regolith, ε' is relatively constant at ~3.2 with the same loss tangent as at the surface due to its density invariance.

Calibration Sites 1-3 are located on the southwestern terrace in the wall of Marcia crater, designated "Zone A" in Figure 3. Surface temperatures within Zone A were retrieved from two VIR infrared images (~170 m/pixel resolution) that overlapped the sites, and range from ~220-255 K. De Sanctis et al. (2015) describe the observed temperatures of this region in detail as inferred from VIR, and Capria et al. (2014) find that the region's thermal inertia is slightly higher when compared to the global average for Vesta—potentially indicative of higher local surface density (on the order of ~1.32 g cm^{-3}) or coarser regolith. Figure 4 shows Sites 1-3 in the case of the average surface density of 1.30 g cm^{-3}, for which $\varepsilon' \sim 2.43$ to 2.46 at the surface and ε' is relatively constant at ~3.2 in the upper meter of Vesta's regolith; tan δ ~

7.5×10^{-3} to 7.9×10^{-3} at both depths. If the local surface density is ~0.02 g cm^{-3} higher than the average, ε' at the surface is expected to be only ~1% greater than the global average at the surface.

5. Implications for Characterizing Vesta's Surface from Radar Observations

The first implication of this study pertains to constraining the ambiguities of Vesta's surface dielectric properties (i.e., surface relative permittivity) as assessed from Earth- and space-based radar backscatter measurements. For example, the received radar circular polarization ratio (CPR) describes the ratio between left- and right-hand polarizations of a surface's backscattered signal, and is often used to infer surface roughness and volatile enrichment (e.g., Thompson, Ustinov & Heggy, 2011; Thompson et al., 2012). Variations in the surface dielectric constant can also impact the CPR measurements and hence compromise the detectability of potential volatile presence (Fa, Wieczorek & Heggy, 2011). The dielectric model presented in this study suggests that the dielectric constant of Vesta's surface varies minimally with temperature, hence we conclude that observed CPRs will be primarily driven by surface roughness at the scale of the radar wavelength (Thompson et al., 2011). For regions with higher or lower values of thermal inertia relative to the average (such as within Marcia crater, and indicative of a difference in either regolith coarseness or surface density), ε' is expected to differ by no more than ~9% from regional values, therefore not inducing a measurable change in CPR based on the analytical polarimetric radar scattering model established by Fa, Wieczorek & Heggy (2011). We therefore expect that observed variations in the CPR of Vesta's surface will correspond to changes in surface roughness rather than in dielectric properties.

The second implication of this study pertains to estimating the porosity of the upper meter of the Vestan regolith, which can be constrained by measuring the dielectric constant from radar observations. This is of particular interest for future landing and sample return missions to asteroids, as exemplified by NASA's OSIRIS-REx sample-return mission to asteroid Bennu (Lauretta et al., 2014), since the accurate determination of near-surface porosity is essential to identifying locations of low hardness in the regolith, whether to maximize the stability of platform anchoring or to optimize drilling rates for subsurface excavation (ElShafie & Heggy, 2013). Previous estimation of the dielectric constant of the Vestan regolith was conducted by Johnston et al. (1989), whose observations suggested a value of $\varepsilon' = 2.9$ and $\tan\delta = 1.5\times10^{-2}$ for the upper 6 cm of the regolith.

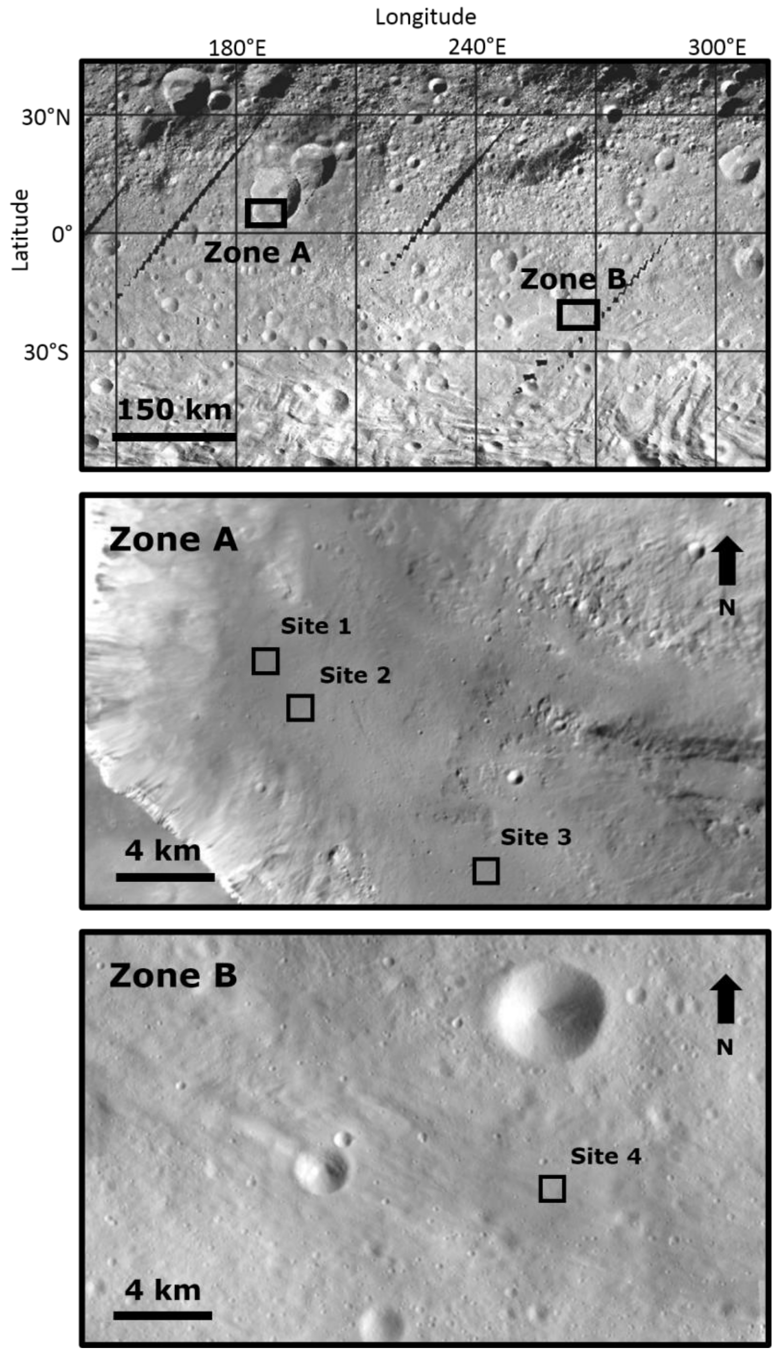

Figure 3. Potential dielectric calibration sites on Vesta's surface. The top-most image is a mosaic map of high-resolution FC images obtained at ~20 m/pixel—centered on (10°S, 230°E) in the Claudia crater coordinate system—and provides broader context for the location of the suggested calibration sites. Zone A (middle image) contains Sites 1-3 and is centered on (5°N, 187°E). Zone B (bottom image) contains Site 4 and is centered on (22°S, 265°E). Each site is characterized by a lack of shadows, and is consistent with a location of accumulation of fine-grained material. Future flyby or orbital radar observations of these low-roughness sites may be used to estimate the surface's dielectric constant.

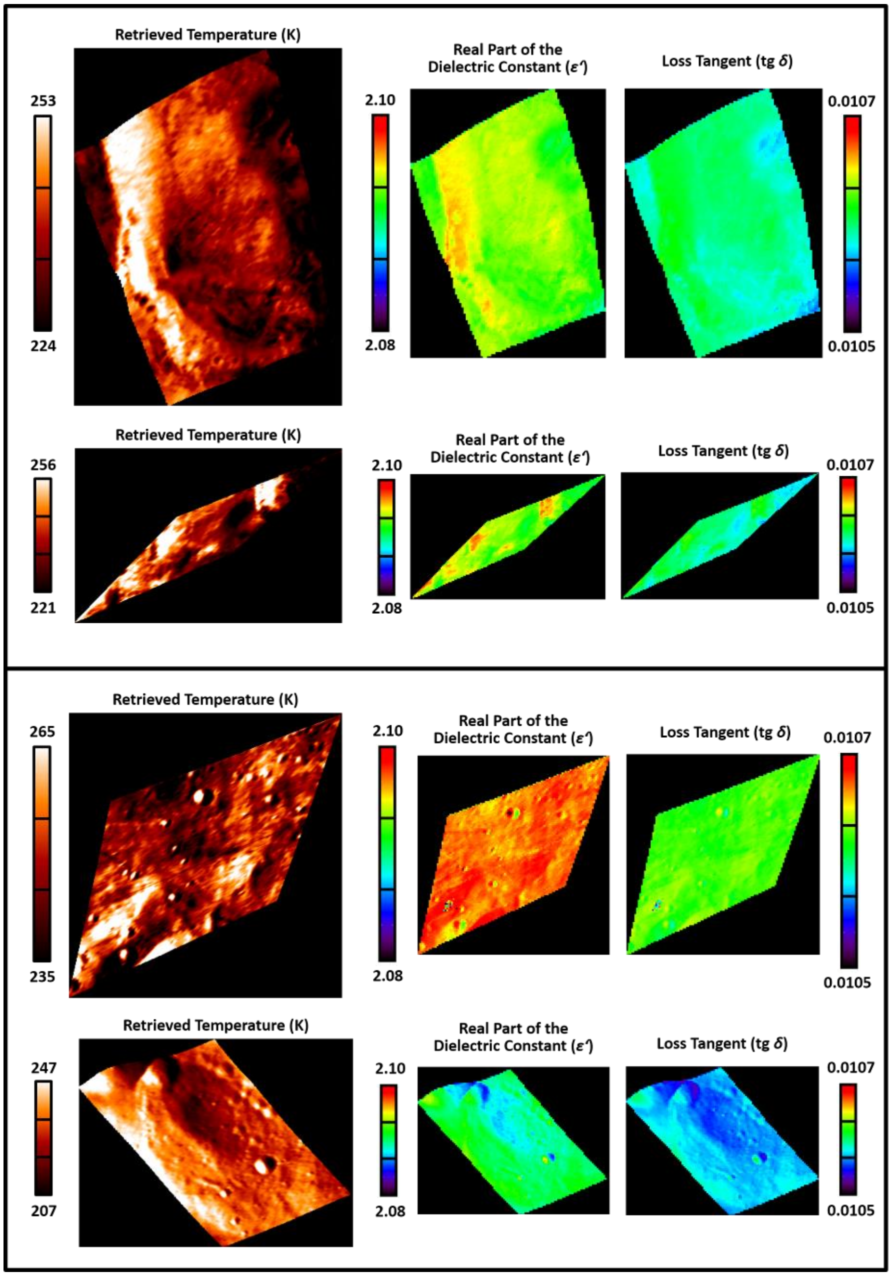

Figure 4. Surface dielectric model of each calibration site. Surface temperatures (left column) were retrieved from four VIR thermal images that overlapped the suggested calibration sites. Each thermal image was acquired in the Vestan morning during High-Altitude Mapping Orbit at a resolution of ~170 m/pixel. In order from top to bottom, the central coordinate of each VIR image is: (3°N, 151°E), containing Sites 1-3; (6°N, 158°E), containing Site 1; (23°S, 268°E), containing Site 4; and (18°S, 266°E), containing Site 4. Corresponding estimates of ε' and tan δ (right column) are calculated for each VIR temperature image with a surface density of 1.30 g cm^{-3}. If local surface density is as high as 1.32 g cm^{-3} in Sites 1-3, as indicated by regionally higher thermal inertia, our dielectric model suggests that ε' is only ~1% greater than the surface average at the same temperatures.

Our analysis, on the other hand, suggests $\varepsilon' \sim 2.3$ to 2.5 at the surface and tan $\delta \sim 6.0\times10^{-3}$ to 8.3×10^{-3}. While Johnston et al. (1989) similarly adopt a lunar analogy for the textural and physical properties of Vesta's upper regolith, their dielectric constant would require a near-surface bulk density of ~1.60 g cm^{-3} to achieve $\varepsilon' = 2.9$, based on the density-dependence of the dielectric constant of the lunar sample used in this study at T = 280 K (Equation 1). Assuming a solid basalt crustal density of ~2.90 g cm^{-3} for Vesta (Raymond et al., 2011), and using our dielectric model to derive bulk density from Johnston et al.'s (1989) estimation of ε', their results suggest a near-surface porosity of ~43%, whereas the best-fit surface bulk density of 1.30 g cm^{-3} (Capria et al., 2014) suggests a porosity of ~55%. The latter is consistent with estimation by Magri et al. (2001), who use hyperspectral and radar observations of asteroid Eros as ground-truth to then estimate near-surface porosities on other small bodies; they find a near-surface porosity of $\sim 59\%^{+19}_{-11}$ for Vesta.

6. Conclusions and Future Work

We have established a surface dielectric model (i.e., the surface's relative permittivity) for the case of a volatile-free upper regolith on Vesta. This model depends on the bulk density and temperature of the upper regolith material as constrained by VIR observations, and the hypothesis that lunar basaltic soil is a suitable compositional analog to Vesta's regolith, as supported by Cartwright et al. (2013). At the surface, our model suggests that ε' ranges from ~2.3 to 2.5 and tan δ from 6×10^{-3} to 8×10^{-3} in the X- and S- radar frequency bands; at one-meter depth, using a lunar density-depth profile, ε' is expected to be ~3.2. For those regions of the Vestan surface exhibiting higher or lower thermal inertia than the global average (Capria et al., 2014), ε' varies less than ±9% from the global average of ~2.4 at the surface, and ±3% from ~3.2 at one meter depth. This implies a near-surface bulk porosity ranging from 55% to 59% and decreasing to ~37% at one meter depth.

It is crucial to obtain accurate assessment of the surface's dielectric properties for asteroids and icy moons from future orbital radar missions to constrain the near-surface mechanical properties (e.g., porosity, density and compressive strength), and subsequently minimize risks associated with future landing, trafficability and coring activities for sample collection and analysis. For instance, passive bistatic radar observations are proposed to be part of Ganymede science observations in the JUICE mission, with the intent to characterize the surface's roughness, dielectric properties and surface porosities (Grasset et al., 2013). We suggest that the radar backscattering properties of asteroid Vesta will be mainly driven by the changes in surface roughness rather than potential dielectric variations in the upper regolith in the S- and X-band.

Future work will consist of combining opportunistic radar observations by Dawn's communications antenna with our dielectric model of Vesta's surface in order to produce surface roughness maps, which in turn can be used to help identify the various cratering processes that have shaped the surface.

7. Acknowledgements

The authors acknowledge Prof. Christopher Russell from UCLA for useful discussions, and also the Dawn Science, Instrument and Operations Teams for their support. Part of this research was carried out at the Jet Propulsion Laboratory, California Institute of Technology, under a contract with the National Aeronautics and Space Administration and was supported in part by the NASA Planetary Geology and Geophysics Program under grant NNXZ08AKA2G. VIR is funded by the Italian Space Agency (ASI) and was developed under the leadership of INAF-Istituto di Astrofisica e Planetologia Spaziali, Rome-Italy. Palmer was funded by a graduate student research award from UCLA.

8. References

Alvarez, R. (1974). "Dielectric comparison of lunar and terrestrial fines at lunar conditions." *J. Geophys. Res.*, **79**(35), 5453–5457. doi:10.1029/JB079i035p05453

Asphaug, E. (2006). "Adventures in Near-Earth Object Exploration." *Science*, **312**(5778), 1328–1329. doi:10.1126/science.1128496

Boisson, J., Heggy, E., Clifford, S. M., Frigeri, A., Plaut, J. J., Farrell, W. M., Putzig, N. E., Picardi, G., Orosei, R., Lognonné, P. & Gurnett, D. A. (2009). "Sounding the subsurface of Athabasca Valles using MARSIS radar data: Exploring the volcanic and fluvial hypotheses for the origin of the rafted plate terrain." *J. Geophys. Res. Planet.*, **114**(E8). doi:10.1029/2008JE003299

Boisson, J., Heggy, E., Clifford, S. M., Yoshikawa, K., Anglade, A. & Lognonné, P. (2011). "Radar sounding of temperate permafrost in Alaska: Analogy to the Martian midlatitude to high-latitude ice-rich terrains." *J. Geophys. Res. Planet.*, **116**(E11). doi:10.1029/2010JE003768

Brouet, Y., Levasseur-Regourd, A. C., Encrenaz, P. & Gulkis, S. (2014). "Permittivity of porous granular matter, in relation with Rosetta cometary mission." *Planet. Space Sci.*, **103**, 143–152. doi:10.1016/j.pss.2014.08.012

Burbine, T. H., Buchanan, P. C., Binzel, R. P., Bus, S. J., Hiroi, T., Hinrichs, J. L., Meibom, A. & McCoy, T. J. (2001). "Vesta, Vestoids, and the howardite, eucrite, diogenite group: Relationships and the origin of spectral differences." *Meteorit. Planet. Sci.*, **36**(6), 761–781. doi:10.1111/j.1945-5100.2001.tb01915.x

Campbell, B. A. (2002). *Radar Remote Sensing of Planetary Surfaces*, Cambridge University Press.

Campbell, M. J. & Ulrichs, J. (1969). "Electrical properties of rocks and their significance for lunar radar observations." *J. Geophys. Res.*, **74**(25), 5867–5881. doi:10.1029/JB074i025p05867

Capria, M. T., Tosi, F., De Sanctis, M. C., Capaccioni, F., Ammannito, E., Frigeri, A., Zambon, F., Fonte, S., Palomba, E., Turrini, D., Titus, T. N., Schröder, S. E., Toplis, M., Li, J.-Y., Combe, J.-P., Raymond, C. A. & Russell, C. T. (2014). "Vesta surface thermal properties map." *Geophys. Res. Lett.*, **41**(5), 1438–1443. doi:10.1002/2013GL059026

Carrier, W. D., Olhoeft, G. R. & Mendell, W. (1991). "Physical Properties of the Lunar Surface." In G. Heiken, D. Vaniman & B. M. French, eds., *The Lunar Sourcebook*, New York, NY: Cambridge University Press, pp. 475–594.

Cartwright, J. A., Ott, U., Mittlefehldt, D. W., Herrin, J. S., Herrmann, S., Mertzman, S. A., Mertzman, K. R., Peng, Z. X. & Quinn, J. E. (2013). "The quest for regolithic howardites. Part 1: Two trends uncovered using noble gases." *Geochim. Cosmochim. Acta*, **105**, 395–421. doi:10.1016/j.gca.2012.11.047

De Sanctis, M. C., Ammannito, E., Capria, M. T., Capaccioni, F., Combe, J.-P., Frigeri, A., Longobardo, A., Magni, G., Marchi, S., McCord, T. B., Palomba, E., Tosi, F., Zambon, F., Carraro, F., Fonte, S., Li, Y. J., McFadden, L. A., Mittlefehldt, D. W., Pieters, C. M., Jaumann, R., Stephan, K., Raymond, C. A. & Russell, C. T. (2013). "Vesta's mineralogical composition as revealed by the visible and infrared spectrometer on Dawn." *Meteorit. Planet. Sci.*, **48**(11), 2166–2184. doi:10.1111/maps.12138

De Sanctis, M. C., Ammannito, E., Capria, M. T., Tosi, F., Capaccioni, F., Zambon, F., Carraro, F., Fonte, S., Frigeri, A., Jaumann, R., Magni, G., Marchi, S., McCord, T. B., McFadden, L. A., McSween, H. Y., Mittlefehldt, D. W., Nathues, A., Palomba, E., Pieters, C. M., Raymond, C. A., Russell, C. T., Toplis, M. J. & Turrini, D. (2012a). "Spectroscopic Characterization of Mineralogy and Its Diversity Across Vesta." *Science*, **336**(6082), 697–700. doi:10.1126/science.1219270

De Sanctis, M. C., Combe, J.-P., Ammannito, E., Palomba, E., Longobardo, A., McCord, T. B., Marchi, S., Capaccioni, F., Capria, M. T., Mittlefehldt, D. W., Pieters, C. M., Sunshine, J., Tosi, F., Zambon, F., Carraro, F., Fonte, S., Frigeri, A., Magni, G., Raymond, C. A., Russell, C. T. & Turrini, D. (2012b). "Detection of Widespread Hydrated Materials on Vesta by the VIR Imaging Spectrometer On Board the *Dawn* Mission." *Astrophys. J.*, **758**(2), L36. doi:10.1088/2041-8205/758/2/L36

De Sanctis, M. C., Frigeri, A., Ammannito, E., Tosi, F., Marchi, S., Zambon, F., Raymond, C. A. & Russell, C. T. (2015). "Mineralogy of Marcia, the youngest large crater of Vesta: Character and distribution of pyroxenes and hydrated material." *Icarus*, **248**, 392–406. doi:10.1016/j.icarus.2014.10.051

Denevi, B. W., Blewett, D. T., Buczkowski, D. L., Capaccioni, F., Capria, M. T., De Sanctis, M. C., Garry, W. B., Gaskell, R. W., Le Corre, L., Li, J.-Y., Marchi, S., McCoy, T. J., Nathues, A., O'Brien, D. P., Petro, N. E., Pieters, C. M., Preusker, F., Raymond, C. A., Reddy, V., Russell, C. T., Schenk, P., Scully, J. E. C., Sunshine, J. M., Tosi, F., Williams, D. A. & Wyrick, D. (2012). "Pitted Terrain on Vesta and Implications for the Presence of Volatiles." *Science*, **338**(6104), 246–249. doi:10.1126/science.1225374

ElShafie, A. & Heggy, E. (2013). "Dielectric and hardness measurements of planetary analog rocks in support of in-situ subsurface sampling." *Planet. Space Sci.*, **86**, 150–154. doi:10.1016/j.pss.2013.02.003

Fa, W. & Wieczorek, M. A. (2012). "Regolith thickness over the lunar nearside: Results from Earth-based 70-cm Arecibo radar observations." *Icarus*, **218**(2), 771–787. doi:10.1016/j.icarus.2012.01.010

Fa, W., Wieczorek, M. A. & Heggy, E. (2011). "Modeling polarimetric radar scattering from the lunar surface: Study on the effect of physical properties of the regolith layer." *J. Geophys. Res.*, **116**(E3). doi:10.1029/2010JE003649

Grasset, O., Dougherty, M. K., Coustenis, A., Bunce, E. J., Erd, C., Titov, D., Blanc, M., Coates, A., Drossart, P., Fletcher, L. N., Hussmann, H., Jaumann, R., Krupp, N., Lebreton, J.-P., Prieto-Ballesteros, O., Tortora, P., Tosi, F. & Van Hoolst, T. (2013). "JUpiter ICy moons Explorer (JUICE): An ESA mission to orbit Ganymede and to characterise the Jupiter system." *Planet. Space Sci.*, **78**, 1–21. doi:10.1016/j.pss.2012.12.002

Hagfors, T. (1964). "Backscattering from an undulating surface with applications to radar returns from the Moon." *J. Geophys. Res.*, **69**(18), 3779–3784. doi:10.1029/JZ069i018p03779

Heggy, E. (2001). "On Water Detection in the Martian Subsurface Using Sounding Radar." *Icarus*, **154**(2), 244–257. doi:10.1006/icar.2001.6717

Heggy, E., Clifford, S. M., Younsi, A., Miane, J. L., Carley, R. & Morris, R. V. (2007). "On the Dielectric Properties of Dust and Ice-Dust Mixtures: Experimental Characterization of the Martian Polar Layered Deposits Analog Materials," *Lun. Planet. Sci. Conf.*, Abstract #1756.

Heggy, E., Palmer, E. M., Kofman, W., Clifford, S. M., Righter, K. & Hérique, A. (2012). "Radar properties of comets: Parametric dielectric modeling of Comet 67P/Churyumov–Gerasimenko." *Icarus*, **221**(2), 925–939. doi:10.1016/j.icarus.2012.09.023

Hill, E., Mellin, M. J., Deane, B., Liu, Y. & Taylor, L. A. (2007). "Apollo sample 70051 and high- and low-Ti lunar soil simulants MLS-1A and JSC-1A: Implications for future lunar exploration." *J. Geophys. Res.*, **112**(E2). doi:10.1029/2006JE002767

Hiroi, T., Pieters, C. M. & Takeda, H. (1994). "Grain size of the surface regolith of asteroid 4 Vesta estimated from its reflectance spectrum in comparison with HED meteorites." *Meteorit. Planet. Sci.*, **29**(3), 394–396. doi:10.1111/j.1945-5100.1994.tb00603.x

Jaumann, R., Williams, D. A., Buczkowski, D. L., Yingst, R. A., Preusker, F., Hiesinger, H., Schmedemann, N., Kneissl, T., Vincent, J. B., Blewett, D. T., Buratti, B. J., Carsenty, U., Denevi, B. W., De Sanctis, M. C., Garry, W. B., Keller, H. U., Kersten, E., Krohn, K., Li, J.-Y., Marchi, S., Matz, K. D., McCord, T. B., McSween, H. Y., Mest, S. C., Mittlefehldt, D. W., Mottola, S., Nathues, A., Neukum, G., O'Brien, D. P., Pieters, C. M., Prettyman, T. H., Raymond, C. A., Roatsch, T., Russell, C. T., Schenk, P., Schmidt, B. E., Scholten, F., Stephan, K., Sykes, M. V., Tricarico, P., Wagner, R., Zuber, M. T. & Sierks, H. (2012). "Vesta's Shape and Morphology." *Science*, **336**(6082), 687–690. doi:10.1126/science.1219122

Johnston, K. J., Lamphear, E. J., Webster, W. J., Lowman, P. D., Seidelmann, P. K., Kaplan, G. H., Wade, C. M. & Hobbs, R. W. (1989). "The microwave spectra of the asteroids Pallas, Vesta, and Hygiea." *Astrophys. J.*, **98**, 335. doi:10.1086/115150

Lauretta, D. S., Bartels, A. E., Barucci, M. A., Bierhaus, E. B., Binzel, R. P., Bottke, W. F., Campins, H., Chesley, S. R., Clark, B. C., Clark, B. E., Cloutis, E. A., Connolly, H. C., Crombie, M. K., Delbó, M., Dworkin, J. P., Emery, J. P., Glavin, D. P., Hamilton, V. E., Hergenrother, C. W., Johnson, C. L., Keller, L. P., Michel, P., Nolan, M. C., Sandford, S. A., Scheeres, D. J., Simon, A. A., Sutter, B. M., Vokrouhlický, D. & Walsh, K. J. (2015). "The OSIRIS-REx target asteroid (101955) Bennu: Constraints on its physical, geological, and dynamical nature from astronomical observations." *Meteorit. Planet. Sci.*, **50**(4), 834–849. doi:10.1111/maps.12353

Leyrat, C., Barucci, A., Mueller, T., O'Rourke, L., Valtchanov, I. & Fornasier, S. (2012). "Thermal properties of (4) Vesta derived from *Herschel* measurements." *Astron. Astrophys.*, **539**, A154. doi:10.1051/0004-6361/201117793

Li, J.-Y., Le Corre, L., Schröder, S. E., Reddy, V., Denevi, B. W., Buratti, B. J., Mottola, S., Hoffmann, M., Gutierrez-Marques, P., Nathues, A., Russell, C. T. & Raymond, C. A. (2013). "Global photometric properties of Asteroid (4) Vesta observed with Dawn Framing Camera." *Icarus*, **226**(2), 1252–1274. doi:10.1016/j.icarus.2013.08.011

Magri, C., Consolmagno, G. J., Ostro, S. J., Benner, L. A. M. & Beeney, B. R. (2001). "Radar constraints on asteroid regolith properties using 433 Eros as ground truth." *Meteorit. Planet. Sci.*, **36**(12), 1697–1709. doi:10.1111/j.1945-5100.2001.tb01857.x

Markwardt, C. B. (2009). Non-linear Least Squares Fitting in IDL with MPFIT. *Astron. Data Anal. Sys. XVIII, ASP Conf. Ser.,* **411**, 251.

Meyer, C. (2010a). 74241: Lunar Sample Compendium. Johnson Space Center, Houston, Texas. http://curator.jsc.nasa.gov/lunar/lsc/

Meyer, C. (2010b). 72441: Lunar Sample Compendium. Johnson Space Center, Houston, Texas. http://curator.jsc.nasa.gov/lunar/lsc/

Nolan, M. C., E. S. Howell, C. Magri, S. J. Ostro, J. D. Giorgini, D. B. Campbell, J.-L. Margot and S. Hudson (2005). Arecibo Radar Imaging of 4 Vesta (abstract), DPS Meeting #37, American Astronomical Society, Cambridge, England.

Olhoeft, G. R., D. W. Strangway and G. W. Pearce (1975). Effects of water on electrical properties of lunar fines. *Proc. 6th Lunar Sci. Conf.*, pp. 3333-3342.

Ostro, S. J., Hudson, R. S., Benner, L. A. M., Giorgini, J. D., Magri, C., Margot, J.-L. & Nolan, M. C. (2002). "Asteroid Radar Astronomy." In *Asteroids III*, pp. 151–168.

Paillou, P., Lasne, Y., Heggy, E., Malézieux, J.-M. & Ruffié, G. (2006). "A study of P-band synthetic aperture radar applicability and performance for Mars exploration: Imaging subsurface geology and detecting shallow moisture." *J. Geophys. Res.*, **111**(E6). doi:10.1029/2005JE002528

Papike, J., Taylor, L. & Simon, S. (1991). Lunar Minerals, in *The Lunar Sourcebook*, edited by Heiken, G. H., D. T. Vaniman and B. M. French (Eds.), pp. 121-182, Cambridge University Press: New York, NY.

Pieters, C. M., Ammannito, E., Blewett, D. T., Denevi, B. W., De Sanctis, M. C., Gaffey, M. J., Le Corre, L., Li, J.-Y., Marchi, S., McCord, T. B., McFadden, L. A., Mittlefehldt, D. W., Nathues, A., Palmer, E., Reddy, V., Raymond, C. A. & Russell, C. T. (2012). "Distinctive space weathering on Vesta from regolith mixing processes." *Nature*, **491**(7422), 79–82. doi:10.1038/nature11534

Prettyman, T. H., Mittlefehldt, D. W., Yamashita, N., Lawrence, D. J., Beck, A. W., Feldman, W. C., McCoy, T. J., McSween, H. Y., Toplis, M. J., Titus, T. N., Tricarico, P., Reedy, R. C., Hendricks, J. S., Forni, O., Le Corre, L., Li, J.-Y., Mizzon, H., Reddy, V., Raymond, C. A. & Russell, C. T. (2012). "Elemental Mapping by Dawn Reveals Exogenic H in Vesta's Regolith." *Science*, **338**(6104), 242–246. doi:10.1126/science.1225354

Reddy, V., Le Corre, L., O'Brien, D. P., Nathues, A., Cloutis, E. A., Durda, D. D., Bottke, W. F., Bhatt, M. U., Nesvorny, D., Buczkowski, D., Scully, J. E. C., Palmer, E. M., Sierks, H., Mann, P. J., Becker, K. J., Beck, A. W., Mittlefehldt, D., Li, J.-Y., Gaskell, R., Russell, C. T., Gaffey, M. J., McSween, H. Y., McCord, T. B., Combe, J.-P. & Blewett, D. (2012). "Delivery of dark material to Vesta via carbonaceous chondritic impacts." *Icarus*, **221**(2), 544–559. doi:10.1016/j.icarus.2012.08.011

Righter, K. & Garber, J. (2011). The HED Compendium. Johnson Space Center, Houston, Texas. http://curator.jsc.nasa.gov/antmet/hed/

Roatsch, T., Kersten, E., Matz, K.-D., Preusker, F., Scholten, F., Jaumann, R., Raymond, C. A. & Russell, C. T. (2012). "High resolution Vesta High Altitude Mapping Orbit (HAMO) Atlas derived from Dawn framing camera images." *Planet. Space Sci.*, **73**(1), 283–286. doi:10.1016/j.pss.2012.08.021

Russell, C. T. & Raymond, C. A. (2011). "The Dawn Mission to Vesta and Ceres." *Space Sci. Rev.*, **163**(1–4), 3–23. doi:10.1007/s11214-011-9836-2

Russell, C. T., Raymond, C. A., Coradini, A., McSween, H. Y., Zuber, M. T., Nathues, A., De Sanctis, M. C., Jaumann, R., Konopliv, A. S., Preusker, F., Asmar, S. W., Park, R. S., Gaskell, R., Keller, H. U., Mottola, S., Roatsch, T., Scully, J. E. C., Smith, D. E., Tricarico, P., Toplis, M. J., Christensen, U. R., Feldman, W. C., Lawrence, D. J., McCoy, T. J., Prettyman, T. H., Reedy, R. C., Sykes, M. E. & Titus, T. N. (2012). "Dawn at Vesta: Testing the Protoplanetary Paradigm." *Science*, **336**(6082), 684–686. doi:10.1126/science.1219381

Scully, J. E. C., Russell, C. T., Yin, A., Jaumann, R., Carey, E., Castillo-Rogez, J., McSween, H. Y., Raymond, C. A., Reddy, V. & Le Corre, L. (2015). "Geomorphological evidence for transient water flow on Vesta." *Earth Planet. Sci. Lett.*, **411**, 151–163. doi:10.1016/j.epsl.2014.12.004

Simpson, R. A., Tyler, G. L., Pätzold, M., Häusler, B., Asmar, S. W. & Sultan-Salem, A. K. (2011). "Polarization in Bistatic Radar Probing of Planetary Surfaces: Application to Mars Express Data." *Proc. IEEE*, **99**(5), 858–874. doi:10.1109/JPROC.2011.2106190

Slade, M. A., Butler, B. J. & Muhleman, D. O. (1992). "Mercury Radar Imaging: Evidence for Polar Ice." *Science*, **258**(5082), 635–640.

Spudis, P. D., Bussey, D. B. J., Baloga, S. M., Butler, B. J., Carl, D., Carter, L. M., Chakraborty, M., Elphic, R. C., Gillis-Davis, J. J., Goswami, J. N., Heggy, E., Hillyard, M., Jensen, R., Kirk, R. L., LaVallee, D., McKerracher, P., Neish, C. D., Nozette, S., Nylund, S., Palsetia, M., Patterson, W., Robinson, M. S., Raney, R. K., Schulze, R. C., Sequeira, H., Skura, J., Thompson, T. W., Thomson, B. J., Ustinov, E. A. & Winters, H. L. (2010). "Initial results for the north pole of the Moon from Mini-SAR, Chandrayaan-1 mission." *Geophys. Res. Lett.*, **37**, L06204. doi:10.1029/2009GL042259

Strangway, D. W. & Olhoeft, G. R. (1977). "Electrical Properties of Planetary Surfaces." *Phil. Trans. R. Soc. A*, **285**(1327), 441–450. doi:10.1098/rsta.1977.0086

Tabatabaeenejad, A. & Moghaddam, M. (2009). "Inversion of Subsurface Properties of Layered Dielectric Structures With Random Slightly Rough Interfaces Using the Method of Simulated Annealing." *IEEE. T. Geosci. Remote*, **47**(7), 2035–2046. doi:10.1109/TGRS.2008.2011982

Takeda, H. (1997). "Mineralogical records of early planetary processes on the howardite, eucrite, diogenite parent body with reference to Vesta." *Meteorit. Planet. Sci.*, **32**(6), 841–853. doi:10.1111/j.1945-5100.1997.tb01574.x

Thompson, T. W., Ustinov, E. A. & Heggy, E. (2011). "Modeling radar scattering from icy lunar regoliths at 13 cm and 4 cm wavelengths." *J. Geophys. Res.*, **116**(E1). doi:10.1029/2009JE003368

Thomson, B. J., Bussey, D. B. J., Neish, C. D., Cahill, J. T. S., Heggy, E., Kirk, R. L., Patterson, G. W., Raney, R. K., Spudis, P. D., Thompson, T. W. & Ustinov, E. A. (2012). "An upper limit for ice in Shackleton crater as revealed by LRO Mini-RF orbital radar." *Geophys. Res. Lett.*, **39**, L14201. doi:10.1029/2012GL052119

Tosi, F., Capria, M. T., De Sanctis, M. C., Combe, J.-P., Zambon, F., Nathues, A., Schröder, S. E., Li, J.-Y., Palomba, E., Longobardo, A., Blewett, D. T., Denevi, B. W., Palmer, E., Capaccioni, F., Ammannito, E., Titus, T. M., Mittlefehldt, D. W., Sunshine, J. M., Russell, C. T. & Raymond, C. A. (2014). "Thermal measurements of dark and bright surface features on Vesta as derived from Dawn/VIR." *Icarus*, **240**, 36–57. doi:10.1016/j.icarus.2014.03.017

Warren, P. H., Kallemeyn, G. W., Huber, H., Ulff-Møller, F. & Choe, W. (2009). "Siderophile and other geochemical constraints on mixing relationships among HED-meteoritic breccias." *Geochim. Cosmochim. Acta*, **73**(19), 5918–5943. doi:10.1016/j.gca.2009.06.030

CHAPTER III

ORBITAL BISTATIC RADAR OBSERVATIONS OF ASTEROID VESTA BY THE DAWN MISSION

Palmer, E. M., Heggy, E. & Kofman, W. (2017). *Nature Communications*, **8**(1).
doi:10.1038/s41467-017-00434-6

1. Abstract

We present the first orbital bistatic radar observations of a small-body during occultation by the Dawn spacecraft at Asteroid Vesta. The radar forward-scattering properties of different reflection sites are used to assess the textural properties of Vesta's surface at centimeter-to-decimeter scales and are compared to subsurface hydrogen concentrations observed by GRaND, assessing potential volatile occurrence in the surface and shallow subsurface. We observe significant differences in surface radar reflectivity, implying substantial spatial variations in centimeter- to decimeter-scale surface roughness. Our results suggest that unlike the Moon, Vesta's surface roughness variations cannot be explained by cratering processes only. In particular, the occurrence of large smoother terrains (over hundreds of square kilometers) that are correlated with heightened hydrogen concentration suggest that potential ground-ice presence may have contributed to the formation of Vesta's current surface texture. Our observations are in concurrence with geomorphological evidence of transient water flow from Dawn Framing Camera images.

2. Introduction

Using the communications antenna aboard the NASA Dawn spacecraft, we conducted the first orbital bistatic radar (BSR) observations of a small body at Asteroid Vesta at grazing incidence angles during entry and exit from occultations. In this configuration, Dawn's high-gain telecommunications antenna (HGA) transmitted X-band (8.4 GHz) radio waves during its orbit of Vesta, while the Deep Space Network (DSN) 70-meter antennas received the signal on Earth. Dawn's orbital trajectory was designed to ensure that the spacecraft's HGA communications antenna would almost constantly be in the line of sight with ground stations on Earth (Thomas & Makowski, 2012), but on occasion, the spacecraft inevitably passed into occultation behind Vesta—lasting as briefly as 5 minutes or as long as 33 minutes. By continuously transmitting basic telemetry data from Dawn's antennas during these events, the opportunity arose to observe surface reflections of HGA-transmitted radar waves from Vesta's surface.

Over the past decades, orbital BSR experiments have been used to assess the textural (and in some cases, dielectric—i.e., relative permittivity) properties of the surfaces of terrestrial bodies such as Mercury (Butler, Muhleman & Slade, 1993), Venus (Simpson et al., 2009), the Moon (Tyler et al., 1967; Nozette et al., 1996; Patterson et al., 2017), Mars (Fjeldbo, Kliore & Seidel, 1972; Simpson & Tyler, 2001) Saturn's moon Titan (Pérez-Ayúcar et al., 2006) and now Comet 67P/CG (Pätzold et al., 2007). In contrast to most orbital BSR experiments, Dawn's HGA beam intersected Vesta's surface at grazing angles of incidence near 89° and in a microgravity environment with substantial variability in its gravity field (Konopliv et al., 2014), leading to a low and variable orbital velocity and hence a more challenging detection of the Doppler-shifted surface echo (hereafter simply referred to as the "surface echo"). While the Mars Global Surveyor (MGS), for instance, orbited at ~3,400 m s^{-1} with respect to Mars' rotating surface during its BSR experiment, Dawn orbited Vesta at a relative velocity of only ~200 m s^{-1}. A high orbital velocity like that of the MGS results in a large Doppler shift between surface-reflected echoes and the direct signal, which greatly simplifies the need to distinguish the two peaks during spectral analysis. In the case of Dawn's BSR observations of Vesta, however, much shorter averaging time and higher frequency resolution is needed to distinguish surface echoes (Willis & Griffiths, 2007).

Through radar power spectral signal analysis of each surface echo, we assess relative surface roughness at centimeter to decimeter scales on Vesta and address its application to understanding the textural evolution of the surface. This is accomplished by measuring the radar cross section σ of each area that is illuminated by the radar lobe of Dawn's HGA (hereafter referred to as the "site" or the "echo site"), which quantifies the cross-sectional surface area that—if equally scattering in all directions—would reflect the echo power measured at the receiver. Hence, larger values of σ are associated with stronger echoes. In turn, echo strength depends on the roughness of the surface at wavelength scales, the angle of incidence, and the intrinsic reflective and absorptive (dielectric) properties of Vesta's surface material at radar wavelengths. Assuming each surface echo is measured at the same angle of incidence and is reflected from equal surface area, we normalize σ to the site of strongest reflection and use estimated dielectric properties of the surface material to assess relative centimeter- to decimeter-scale surface roughness on Vesta with respect to a given reference site.

Through the comparison of relative surface roughness with estimated surface ages of geologic units based on two crater counting methods (Williams et al., 2014), we assess the physical processes that shaped Vesta's surface roughness at the same scales as done previously for the Moon (e.g., Thompson, Ustinov & Heggy, 2011). In turn, surface roughness provides insight into the shock history of the body (Campbell et al., 2010) and identification of fracturing mechanisms such as those resulting from thermal erosion caused by diurnal expansion and contraction of volatiles within the surface host rocks (Shepard et al., 2001). The comparison of relative roughness with observations of subsurface hydrogen concentration [H] from Dawn's Gamma Ray and Neutron Detector (GRaND; Prettyman et al., 2012); with hydrated material distribution from Dawn's Visible and Infrared Mapping Spectrometer (VIR; De Sanctis et al., 2012); and with surface thermal inertia and associated multi-meter-scale topography modeled from VIR data (Capria et al., 2014) enable further investigation into the relationship between volatile presence and centimeter- to decimeter-scale surface roughness. Characterizing the roughness properties of Vesta's surface and of other small bodies is also key to assessing landing, anchoring, sampling and surface trafficability in future missions (ElShafie & Heggy, 2013).

Given the low risk, low operational constraints and opportunistic nature of the orbital BSR experiment by Dawn, other planetary missions can conduct similar observations even in the case of unlikely major science payload failure. Orbital BSR can also be used to constrain ambiguities associated with surface roughness and potentially surface dielectric properties of other small bodies as is proposed for the JUpiter ICy Moons Explorer (JUICE) mission at Ganymede (Grasset et al., 2013). In our study of Dawn's bistatic radar observations of Asteroid Vesta, we successfully detect radar echoes from Vesta's surface, and find significant variations of radar reflectivity across the surface—where stronger surface echoes suggest smoother surfaces. Unlike the Moon, however, Vesta's surface roughness variations cannot be explained by cratering only—particularly where smoother areas overlap areas of heightened hydrogen concentration, suggesting that volatile-involved processes have also contributed to shaping the surface of Vesta.

3. Results

3.1. Observation Geometry and Measurement Requirements

During the BSR experiment at Vesta, the HGA aboard Dawn is used to transmit telemetry data at X-band radar frequency (8.435 GHz, 3.55 cm wavelength) while the three 70-m DSN antennas at Goldstone (US), Canberra (Australia) and Madrid (Spain)—which have similar receiving characteristics (Supplementary Table 1)—are used to receive (Supplementary Fig. 1) (Taylor, 2009). Throughout the Dawn mission, the HGA continuously transmits right-hand circularly polarized (RCP) radio waves with a beamwidth of ~1.6°. The transmission frequency of the HGA is typically driven by the highly stable DSN uplink signal, as this allows for accurate Doppler and range tracking measurements (Taylor, 2009; Thomas & Makowsky, 2011; Konopliv et al., 2014). When the uplink signal is not available—as anticipated in the minutes preceding and following an occultation of Dawn behind Vesta—the transmission frequency is instead driven by an internal auxiliary oscillator on board the spacecraft (Taylor, 2009; Thomas & Makowsky, 2011). While the onboard oscillator generates too much Doppler noise to be used for gravity science to measure the absolute Doppler shift of the direct signal (Konopliv et al., 2012), its frequency is sufficiently stable over the integration time of BSR measurements—a few seconds rather than one minute—to measure the relative Doppler shift between the surface echo and direct signal, which are equally affected by slow Doppler changes. Due to the opportunistic nature of the experiment, the HGA also remains in a fixed orientation pointed toward Earth throughout each BSR observation (Thomas & Makowski, 2012). As a consequence, Dawn's transmitted radio waves scatter from Vesta's surface just before and after each occultation of the Dawn spacecraft behind Vesta, resulting in surface echoes at high grazing incidence angles of ~89°.

The spacecraft's trajectory is also designed to ensure that Dawn's solar panels are constantly illuminated by sunlight. This geometry allows the primary observation instruments to have maximized visibility of Vesta's sunlit surface throughout each orbit (Thomas & Makowski, 2012). As a consequence, while Dawn is in a polar orbit around Vesta (Russell &

Raymond, 2012), the sites intercepted by the spacecraft's HGA beam yield surface echoes at mid-latitudes between 30°S and 45°N (Supplementary Fig. 2).

In contrast to previous planetary BSR observations performed for large bodies, with incidence angles between ~0° and ~80°, the surface reflections from Dawn's BSR experiment are almost entirely in the regime of forward scattering by which the polarization of a circularly transmitted wave is conserved in major part even after reflection from the target's surface (e.g., Harmon, 2008). As a consequence, we cannot employ the typical method of measuring the circular polarization ratio (CPR) to evaluate surface roughness or the dielectric constant (i.e., relative permittivity) from surface echoes (e.g., Simpson et al., 2011), and instead develop a method to derive relative surface roughness by measuring the relative strength of reflected power from each echo site.

While DSN station operators record receiver system temperatures as part of standard calibration procedures (Simpson et al., 2011), this information was not included with the raw BSR dataset, as these were acquired during the downlink of engineering-only telemetry. Since radar data acquired by the DSN are not calibrated in absolute voltage, we instead calibrate the received power to theoretical received power derived from known orbital geometry and transmitter and receiver specifications. While each of the 70-m DSN antennas are held to the same measurement requirements (listed in Supplementary Table 1), we observe a decrease of ~10% in the direct signal's ratio of measured to theoretical power over the course of a 33-minute occultation, and differences in the ratio by as much as 24% from orbit to orbit. Fluctuations in the received power are attributed to variations in the pointing accuracy of the HGA aboard Dawn, since one of the four reaction wheels aboard the spacecraft—used to counteract pointing errors—failed prior to rendezvous with Vesta. We minimize the effect of variable pointing accuracy by measuring the direct signal within a few seconds of the occultation echo observation. A full description of our error analysis is provided in the Methods section.

As previously mentioned, in additional contrast to other planetary BSR experiments, Dawn also has a relatively slow orbital velocity (~200 m s^{-1}) with respect to Vesta's surface. Since the relative motions of the target surface, the transmitter, and the receiver determine the Doppler shift that separates surface echoes from the frequency of directly transmitted radar waves, we therefore expect a small Doppler shift from Dawn's BSR experiment at Vesta. As a result, a frequency resolution of a few Hz is necessary to resolve surface Doppler shifted echoes from the direct signal in the received power-frequency spectra. To optimize the tradeoff between signal-to-noise ratio (SNR), frequency drift and spectral resolution, our final spectra are each averaged over two windows of 2.5-second integration time. Each spectrum is separated by a 1-second time interval in Fig. 2.

3.2. Orbital BSR Observations

Our analysis begins with the calculation of the expected differential Doppler shift between the direct signal and surface reflections. This is compared with the observed differential Doppler shift in the power spectra to confirm the detection of surface echoes. From the power spectrum of each echo, we measure radar cross sections of Vesta's surface and finally estimate the relative surface roughness of each echo site.

The differential Doppler shift δf between the direct signal and surface echo is attributed to the rotation of Vesta and the relative orbital motion of the Dawn spacecraft (see Supplementary Tables 2 and 3). Following the procedure for planetary bistatic radar experiments (Simpson et al., 1993), theoretical δf is calculated for occultation entry of orbit 355. The surface echo is determined to have a Doppler-shifted frequency within ~2 to 20 Hz of that of the direct signal when considering uncertainties in (1) the ephemeris position of the spacecraft (Krening, Semenov & Acton, 2012); (2) the orbital velocity of the spacecraft due to deviations in the gravity field from the homogeneous model; (3) the precise latitude and longitude of the echo site center, given the large area that is illuminated by the HGA beam at grazing incidence; and (4) the estimated radius (and subsequent rotational velocity) of the echo site, due to surface topography that is illuminated within the large radar footprint.

The theoretical value of $\delta f \sim 2$ Hz is therefore the lower limit of the differential Doppler shift between the surface echo and direct signal, under the assumptions that (1) the position and rotational velocity of the echo site on Vesta are well-represented by a point on the surface, and (2) Dawn's orbital velocity is constant. Our calculation is consistent with the expectation of a small frequency separation due to Dawn's low orbital velocity that is orders of magnitude smaller than observed in typical orbital BSR experiments at larger planetary bodies—such as for the orbital BSR experiment by the Mars Global Surveyor spacecraft, which detected radar reflections from the martian surface that were separated by as much as 10 kHz from the received direct signal (Simpson & Tyler, 2001).

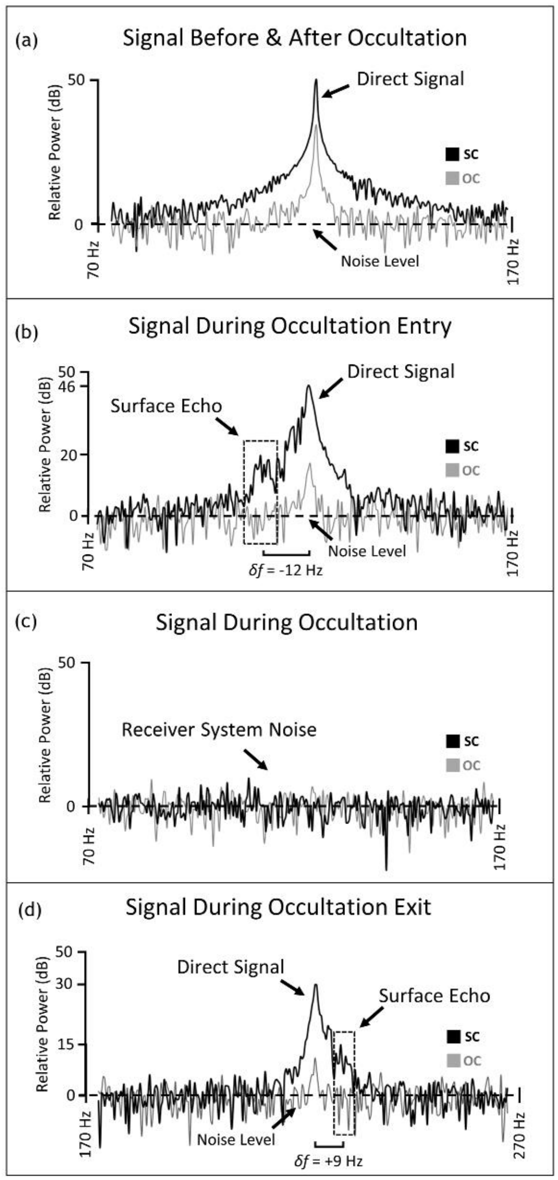

Figure 1. Typical progression of received radar signal over the course of an occultation. The frequency spectra show power received in the same-sense circular (SC) and opposite-sense circular (OC) polarization (a) before/after occultation, (b) during entry into occultation, (c) during occultation, and (d) during exit from occultation of orbit 355. All surface echoes during occultation entry are Doppler shifted to lower frequencies than the direct signal, while all surface echoes during occultation exit exhibit Doppler shifts to higher frequencies than the direct signal.

Figures 1 and 2 show the temporal progression of received power spectra from BSR observations during orbit 355. In Fig. 1, black spectra have the same-sense circular (SC) polarization as the transmitted wave, RCP, while gray spectra correspond to the power received with opposite-sense circular (OC) polarization, LCP.

Figure 1(a) shows the direct signal prior to occultation at its peak strength of 50 dB relative to the noise level. The presence of measurable LCP power in the direct signal indicates imperfection in the transmitting antenna and the high sensitivity of the 70-m DSN receivers, as the power in LCP is ~2.5% of (~16 dB below) the power measured in RCP. Panel (b) shows a typical power spectrum during Dawn's entrance into occultation behind Vesta. Most of the direct signal is still visible to the receiver on Earth, while a secondary peak (the surface echo) emerges with a relative Doppler shift δf of –12 Hz with respect to the direct signal. The LCP component is now ~28 dB below the RCP peak, potentially because the main lobe of the antenna has become partially obstructed by Vesta's surface.

Panel (c) shows typical RCP and LCP spectra observed amid full occultation of Dawn behind Vesta, and consist solely of receiver system noise. In the final panel (d), Dawn has partially exited from occultation behind Vesta. Most of the direct signal is again in the line of sight with the receiver, while a secondary surface echo peak is observed with a relative Doppler shifted frequency +9 Hz higher than that of the direct signal. The LCP component is again ~28 dB weaker than the received RCP power, potentially due to partial obstruction of the antenna lobe.

The observed δf of –12 Hz during occultation entry is consistent with our calculated range of theoretical δf values between ~2 and 20 Hz, where the upper limit of theoretical δf is attributed to uncertainties in the precise position and velocity of the spacecraft, and in the location and subsequent radius and rotational velocity of each echo site. Furthermore, the direct signal has a frequency width of ~10 Hz at 31 dB below the peak at full strength, such that the secondary peak of an emerging surface echo is not observable until the direct signal has been sufficiently weakened behind Vesta or when δf is greater than half the frequency width of the diminishing direct signal.

This observation is further emphasized in Fig. 2(a), which shows the progression of RCP power spectra over the course of 16 seconds during Dawn's gradual entry into occultation behind Vesta during orbit 355. The lowest plotted spectrum is the same as that of panel (a) in Fig. 1, showing the direct signal prior to occultation. With each successive second (indicated by the next higher, vertically offset spectrum), direct signal power decreases as the HGA boresight passes behind Vesta's horizon, while reflections from the surface emerge at a lower frequency until the topmost spectrum at which point the spacecraft is completely obscured by Vesta; only receiver noise is detected. Fig. 2(b) shows the same temporal progression for occultation exit. The lowest spectrum shows the first moment of observable surface echo after occultation, and progresses to the top spectrum at which point the direct signal is fully in the line of sight with the receiver.

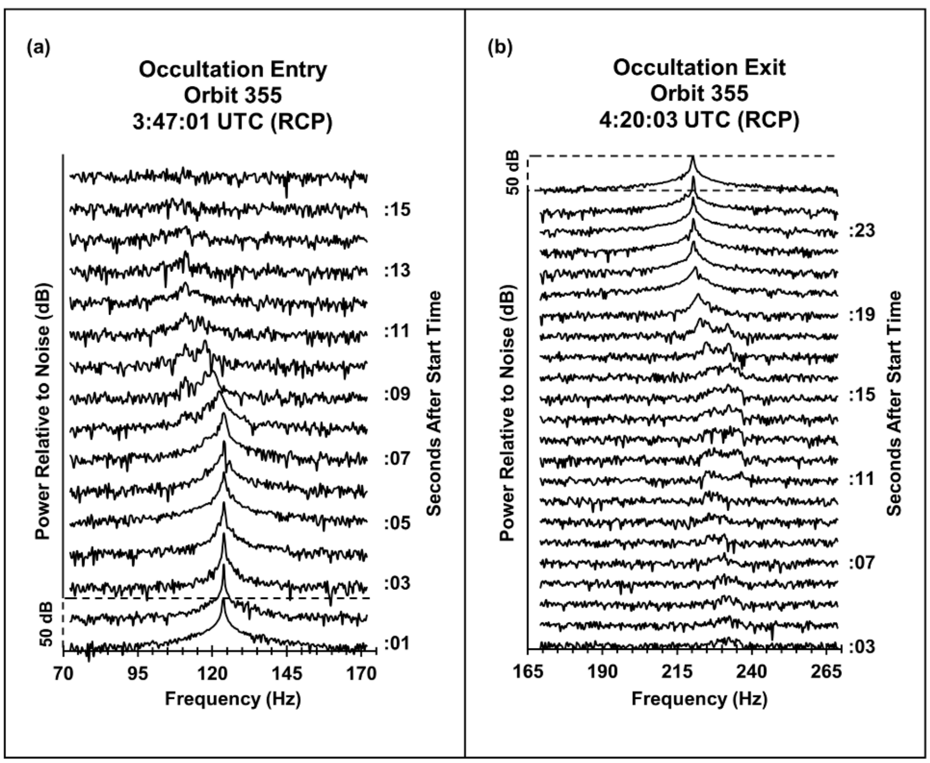

Figure 2. Progression of received radar signal throughout entrance into and exit from occultation during orbit 355. Occultation entry (a) spans ~16 seconds while occultation exit (b) spans ~25 seconds. Each spectrum is generated from two averages of 2.5-second integrated spectra, corresponding to a total of 5 seconds of radar data that start at each listed timestamp. Spectra are vertically offset for display purposes, where each successively higher spectrum corresponds to a step forward by 1 second.

Another consequence of radar reflections at high grazing incidence angle is that the polarization of the transmitted RCP waves are conserved in the forward-scatter direction (e.g., Harmon, 2008). Since surface echoes do not contain a measurable LCP component, their spectra are excluded from Fig. 2. For reference, plots of the received null LCP power spectra are provided in Supplementary Fig. 3 during entry and exit from occultation of orbit 355.

In total, 20 cases of surface echoes are detected at mid-latitudes, 14 of which (1) reflect from sites with minimal topographic variability and (2) are sufficiently distinguishable from the direct signal to allow for characterization of the surface's scattering properties in these regions. The radar-illuminated sites of the 14 echoes are plotted in Fig. 3(a) on an equirectangular projection of Vesta's surface. High-resolution images of the smoothest and roughest observed echo sites are provided in Supplementary Fig. 5.

Vesta's surface radar properties are explored hereafter using the forward-scatter radar cross section σ with units of km^2. This parameter quantifies the cross-sectional surface area of a perfectly isotropic scatterer that would reflect the same echo power that is measured at Earth. For a given acquisition geometry, σ depends on the surface's dielectric and roughness properties at the radar wavelength, and is determined from the ratio of received echo power to transmitted power (Willis & Griffiths, 2007). Typically, σ is normalized to the surface area illuminated at each echo site (σ^0) and directly compared with backscatter measurements from other observations of the target surface (e.g., Mitchell et al., 1996) or of other planetary bodies. However, due to the ambiguity associated with topographic shadowing effects at grazing incidence and lack of directly comparable measurements in the forward-scattering regime, each σ measured at Vesta is instead assumed to have (1) approximately equal area illuminated during echo reflection and (2) approximately equal power incident on the surface at 89°. Forward-scatter σ is then normalized to σ_{max}, i.e. that of the site with maximum observed echo power. The resulting differences in relative forward-scatter radar cross sections (σ/σ_{max}) are then used to infer variations in roughness at centimeter to decimeter scales across the surface of Vesta.

Figure 3(a) shows the resulting distribution of (σ/σ_{max}) on Vesta, where the reference site for $\sigma_{max} = 3588 \pm 200$ km^2 is located northwest of Caparronia crater (occultation exit of orbit 406). Values of (σ/σ_{max}) range from –16.3 ± 0.5 dB at the site of weakest measured echo power, to zero dB at the σ_{max} reference site.

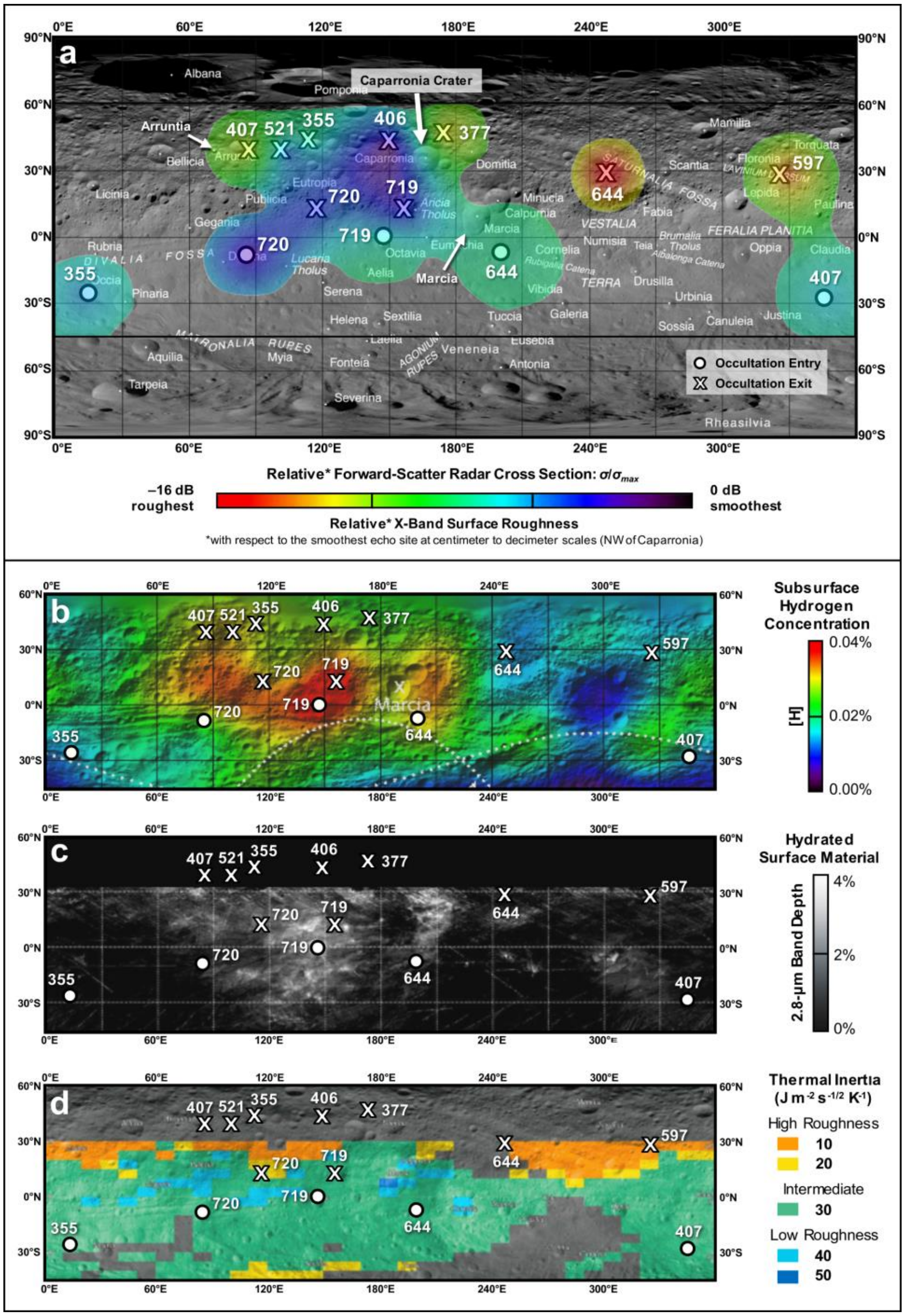

Figure 3. Comparison of BSR results with observations by the GRaND and VIR instruments aboard Dawn. Map (a) shows the distribution of relative radar cross section interpolated between echo sites and overlain upon an equirectangular projection of Vesta's surface; (b) shows subsurface hydrogen concentration to a depth of a few decimeters (Prettyman et al., 2012); (c) shows the distribution of hydrated material at the surface (De Sanctis et al., 2012); and (d) shows the surface's thermal inertia and multi-meter-scale topography modeled from VIR thermal observations (Capria et al., 2014). O's and X's mark locations where BSR surface echoes have been detected during the associated orbit number.

The intrinsic reflective and absorptive (i.e., dielectric) properties of Vesta's surface material, as estimated from Dawn's Visible and Infrared Spectrometer (VIR) observations, are found to be constant throughout the upper regolith in S- (2.3 GHz) and X-band (8.4 GHz) (Palmer et al., 2015). For our sites which have minimum topographic variability, changes in (σ/σ_{max}) are therefore attributed to spatial variations in surface roughness at centimeter to decimeter scales across Vesta. Radar echoes received from smoother sites reflect strongly in the forward direction and hence exhibit the strongest measured power in the regime of forward scatter, whereas weaker echoes are observed when reflected from rougher surfaces (Willis & Griffiths, 2007). Echo sites with the highest (σ/σ_{max}) ratios (blue in Fig. 3) therefore correspond to the smoothest observed surfaces on Vesta and sites with the lowest ratio (in red) represent the roughest observed surfaces. Table 1 contains measurements of (σ/σ_{max}) for all surface echoes, including brief descriptions of the terrain associated with each reflection site (Williams, Yingst & Garry, 2014).

4. Discussion

Vesta is presumed to have been largely depleted of volatiles during its differentiation (Russell & Raymond, 2012) but recent observations by Dawn's Gamma Ray and Neutron Detector (GRaND) and Visible and Infrared Mapping Spectrometer (VIR) suggest the potential introduction of hydrated material through meteoritic impacts (Prettyman et al., 2012; Reddy et al., 2012). Fig. 3 shows the comparison of (a) the spatial distribution of relative forward-scatter radar cross section (σ/σ_{max})—inversely proportional to centimeter- to decimeter-scale surface roughness—with (b) the distribution of hydrogen concentration [H] measured by GRaND at a depth of a few centimeter to decimeters (Prettyman et al., 2012); (c) the distribution of hydrated surface material by VIR (De Sanctis et al., 2012); and (d) thermal inertia and multi-meter-scale topography modeled from VIR thermal observations (Capria et al., 2012).

All echo sites within ±28° latitude from the equator have (σ/σ_{max}) > –7 dB, [H] > 0.015% and overlap regions with hydrated surface material, suggesting that the smoothest observed terrains at centimeter and decimeter scales (relative to the smoothest reference site, which is observed northwest of Caparronia crater) are correlated with heightened hydrogen concentration near Vesta's equator. While hydrogen concentration, in turn, has been correlated with the presence of low-albedo

Table 1. Forward-scatter radar cross sections σ of Vesta's surface measured at each echo site from high-incidence bistatic radar surface reflections

Orbit No.	Occultation Date & Stage	Time at Receiver HH:MM:SS (UTC)	Surface Echo Location (Lat., Lon.)	Terrain (Williams et al., 2014)	[1] σ (km^2)	[2] σ/σ_{max} (dB)
355	24 DEC 2011 Entry	3:47:09	(25°S, 13°E)	Rheasilvia smooth terrain (rst)	1361 ± 19	–4.2 ± 0.2
355	24 DEC 2011 Exit	4:20:19	(43°N, 115°E)	Northern cratered trough terrain (nctt)	823 ± 16	–6.4 ± 0.3
377	28 DEC 2011 Exit	5:26:29	(46°N, 173°E)	nctt	262 ± 15	–11.4 ± 0.3
406	02 JAN 2012 Exit	13:11:48	(40°N, 149°E)	nctt	3588 ± 200	0 (reference value[2] for site with maximum surface echo strength)
407	02 JAN 2012 Entry	17:06:36	(26°S, 346°E)	rst	1124 ± 17	–5.0 ± 0.3
407	02 JAN 2012 Exit	17:38:17	(39°N, 87°E)	Dark material near Arruntia crater	280 ± 12	–11.1 ± 0.3
521	23 JAN 2012 Exit	16:21:05	(38°N, 104°E)	nctt	1539 ± 27	–3.7 ± 0.3
597	06 FEB 2012 Exit	15:10:12	(29°N, 328°E)	Lavinium Dorsum	156 ± 13	–13.6 ± 0.4
644	15 FEB 2012 Entry	6:10:47	(7°S, 204°E)	Marcia crater ejecta	782 ± 21	–6.6 ± 0.3
644	15 FEB 2012 Exit	6:27:29	(29°N, 247°E)	Saturnalia Fossae	84 ± 8	–16.3 ± 0.5
719	29 FEB 2012 Entry	0:39:44	(0°N, 148°E)	Octavia crater	971 ± 87	–5.7 ± 0.5
719	29 FEB 2012 Exit	0:45:13	(13°N, 156°E)	Cratered highlands near Aricia Tholus	2369 ± 115	–1.8 ± 0.3
720	29 FEB 2012 Entry	4:59:51	(7°S, 86°E)	Divalia Fossae	3012 ± 43	–0.8 ± 0.2
720	29 FEB 2012 Exit	5:10:37	(13°N, 118°E)	Cratered highlands	2080 ± 42	–2.4 ± 0.3

[a] Smaller values of the forward-scatter radar cross section σ are attributed to weaker radar reflections from Vesta's surface. Weaker radar reflections suggest rougher surfaces at the scale of centimeters to decimeters.

[b] The largest radar cross section σmax was measured from surface echoes located northwest of Caparronia crater, which is therefore the smoothest observed echo site at centimeter and decimeter scales. Decreasing values of (σ/σ_{max}) are associated with progressively rougher surfaces at centimeter and decimeter scales

surficial deposits of hydrated material ("dark material") (Prettyman et al., 2012), these deposits are proposed to have the mineralogical composition of carbonaceous chondrites (Reddy et al., 2012), which have indistinguishable dielectric properties from that of the surrounding lunar-like regolith—specifically, ε' is estimated to be ~2.4 for Vesta's basaltic regolith (Palmer et al., 2015), ε' ~ 2.6 as measured for porous ordinary chondrites (Heggy & Palmer et al., 2012), and ε' ~ 2.6 to 2.9 as measured for porous carbonaceous chondrites (Hérique et al., 2016). Hence, the observed correlation of radar reflectivity with hydrogen concentration is due to textural variation and not in the dielectric properties of the surface.

The regolith should otherwise be particularly rough at the centimeter-to-decimeter scale in these geologic units—the cratered highlands, ejecta blankets of Octavia and Marcia crater, ejecta material from Rheasilvia, and Divalia Fossae (Williams, Yingst & Garry, 2014)—in the absence of smoothing erosional processes such as the melting, run-off and recrystallization of water ice after an impact, suggesting the potential presence of subsurface volatiles at these echo sites. The occurrence of heightened [H] with rougher surfaces such as in the northern cratered trough terrain northeast of Caparronia crater potentially results from the following sequence: (1) initial smoothing due to impacts that induce ground-ice melting, run-off and re-crystallization of buried ice; and then (2) subsequent fracturing due to thermal erosion that is caused by the expansion and contraction of remnant volatile inclusions within the breccias and impactites that constitute a large fraction of the regolith's surface and shallow subsurface (i.e. the first meter), due to significant diurnal temperature fluctuations. This hypothesized mechanism is further supported by the observation of gullies and flow features on crater walls from Dawn Framing Camera (FC) images that suggest transitional melting of ground-ice during the post-impact process (Scully et al., 2015). Above 30°N, roughness is observed to lessen with increasing [H], suggesting less fracturing occurring from thermal erosion at higher latitudes, which is consistent with minimal solar illumination at northern latitudes due to seasonal shadowing during Dawn's orbit of Vesta (e.g., Capria et al., 2015).

On the Moon, there is a strong correlation between the surface age of geologic units and their radar backscatter properties, implying that impact cratering is the dominant process that governs the texture of the lunar regolith at centimeter to decimeter scales (Thompson et al., 1974). Younger units, especially crater ejecta, are rough at centimeter and decimeter scales due to the presence of shocked and fractured meter and centimeter sized fragments from impacts; over time, older cratered surfaces are covered with a layer of fine debris that buries rock fragments, therefore appearing smooth at the surface to radar at centimeter and decimeter scales (Thompson et al., 1974). However, we do not observe the same correlation on Vesta between relative surface roughness and relative surface ages. Williams et al. (2014) studied the chronology of Vesta's various geologic units through crater counting methods and developed two models for surfaces ages: one extrapolated from lunar-derived chronology, and the other from models of asteroid belt dynamics. In Supplementary Fig. 4 we plot the approximate surface age of each echo site's geologic unit for each chronology against their observed relative radar cross section (σ/σ_{max}) values, but we find no observable correlation of radar scattering properties with surface age, suggesting that cratering cannot be the only process shaping Vesta's surface texture.

The lack of observable correlation between cratering and radar-wavelength surface texture is further evidenced by high-resolution Dawn FC images of Vesta at the sites of strongest and weakest BSR surface echo reflections—i.e. the smoothest and roughest sites observed by BSR, respectively, at centimeter to decimeter scales. Panel (a) of Supplementary Fig. 5 shows a regional view of the smoothest echo site at 66 m/pixel resolution on the left, and a subset of the echo site at 18 m/pixel resolution on the right. Panel (b) shows the roughest echo site at 62 m/pixel and 22 m/pixel. We do not observe a correlation between surface topography at the scale of meters to tens of meters with the centimeter-to-decimeter scale surface roughness that is observed by Dawn's BSR investigation.

Together, these observations suggest that unlike the Moon, impact cratering processes cannot solely explain Vesta's surface roughness, and that fracturing arising from subsurface volatile occurrence may have contributed to the formation of the current surface texture. This is further supported by the thermal inertia map of Vesta's surface in Fig. 3(d), which also shows no correlation between BSR-derived centimeter- to decimeter-scale roughness and the multi-meter-scale topography that is derived during the process of thermal inertia modeling (Capria et al., 2014).

In total, we have identified 10 probable sites for potential shallow subsurface volatile occurrence that include occultation entry during orbits 644, 719 and 720, and occultation exit during orbits 355, 406, 407, 521, 719 and 720. Each corresponds to sites with the smoothest to intermediate surface roughness on Vesta—and exhibit heightened subsurface hydrogen concentrations between 0.025% and 0.04% as observed by GRaND (Prettyman et al., 2012).

With regard to future landing and sample collection missions on asteroids (ElShafie & Heggy, 2013), the observed variation of centimeter- to decimeter-scale surface roughness across Vesta further emphasizes the importance of these opportunistic observations to be systematically carried out to support safe landing, proper anchoring and optimized collection of potentially volatile-enriched samples. BSR observations constrain the spatial variability of surface roughness on small bodies and can thereby support safe trafficability—especially for equatorial regions as are observed on Vesta, which are frequently considered for landing and sampling return sites (ElShafie & Heggy, 2013). While topographic maps derived from orbital observations provide first-order information about large-scale obstacles, high-resolution orbital bistatic radar observations yield information about surface roughness at centimeter to decimeter scales that cannot be derived from Earth-based observations. On Vesta, no correlation is observed between topographic elevation and the distribution of surface roughness.

In summary, the orbital BSR experiment at Asteroid Vesta emphasizes the importance of utilizing standard communications antennas aboard spacecraft to derive constraints on surface roughness at sub-topographic scales. In our future work, we will apply the same analysis to BSR observations of icy asteroid Ceres, the second target of the Dawn mission to understand potential subsurface volatile occurrence.

5. Methods

5.1. Experimental Constraints and Data Selection

During the bistatic radar (BSR) experiment at Vesta, the Dawn spacecraft's high-gain communications antenna (HGA) was used to transmit telemetry data at X-band radar frequency (8.435 GHz, 3.55 cm wavelength) in right-hand circular polarization (RCP), while the three 70-m Deep Space Network (DSN) antennas on Earth—at Goldstone (US), Canberra (Australia) or Madrid (Spain)—were used to receive (Taylor, 2009). The three receiving systems have the same measurement requirements in terms of noise temperature, antenna gain, pointing loss and polarization loss as listed in Supplementary Table 1. In two-way coherent downlink mode, Dawn's transmission frequency is driven by the DSN's uplink frequency and yields a Doppler stability ($\Delta f / f$) of 10^{-12} over 60-second measurements, i.e. a frequency drift of ~0.0001 Hz s^{-1} (Thomas & Makowski, 2012). In one-way or non-coherent downlink mode—used when the uplink signal is expected to be unavailable, such as the minutes preceding and following an occultation—the transmission frequency is driven by an onboard internal auxiliary oscillator with a maximum frequency drift of 0.05 Hz s^{-1} (Chen et al., 2000). One-way downlink mode contains too much Doppler noise to be used for gravity science (Konopliv et al., 2012) but is sufficiently stable for BSR measurements since they are integrated over a much shorter timespan—a few seconds, as opposed to one minute for gravity science measurements—and because we are measuring the relative Doppler shift between the surface echo and direct signal, which are equally affected by slow Doppler changes.

Dawn's HGA was almost constantly pointed at ground stations on Earth for communication (Thomas & Makowski, 2012), so by continuously transmitting basic telemetry information, we had the opportunity to observe surface reflections of the radar signal just before and after each occultation of the Dawn spacecraft behind Vesta at highly oblique incident angles of ~89° as depicted in Supplementary Fig. 1, similar to geometry of the BSR experiment at Mars by the Mars Global Surveyor (Tyler et al., 2001). In order to analyze the resulting bistatic radar data, we selected occultations that occurred specifically during Dawn's lowest-altitude mapping orbit (LAMO) around Vesta, and using the HGA to ensure the strongest observable surface echoes. During LAMO, there were 16 unique orbits during which an occultation occurred, and therefore 16 individual entries and 16 individual exits.

Out of these events, several were discarded based on the following criteria: (1) if the radar amplitude data files containing RCP and LCP were copies of each other; (2) if the direct (carrier) signal's power did not consistently exhibit 50 dB strength before or after its occultation; (3) if the surface echo was indistinguishable from the noise (i.e. $< \sim 3$ dB); (4) if the window of occultation entry or exit was so brief that the signal disappeared faster than our temporal resolution (e.g., if the carrier dropped by 30 dB within a few seconds, and usually showed no indication of a measurable surface echo); (5) if the δf was too small to distinguish the surface echo's power from that of the carrier; or (6) if the surface echo occurs in a region of high topographic variability with respect to the incident HGA beam size, which is assessed below. In all, 5 entries and 9 exits passed our criteria for analysis and measurement of σ (km^2) and σ/σ_{max} (dB). The following sections describe the method used to process and analyze the resulting BSR data. Supplementary Table 1 summarizes the acquisition parameters of the BSR experiment.

5.2. Processing DSN BSR Data

Radio waves received by the DSN 70-meter antennas are recorded as amplitude (voltage) versus time, and are collected in two channels: right- and left-hand circular polarization (RCP and LCP). Within each channel, amplitude data is recorded in two components, in-phase I and quadrature Q, which correspond to the real and imaginary parts of the complex voltage, respectively.

The raw modulated telemetry data collected at the DSN antenna is sampled at a rate of 16 kHz. In addition, a Doppler shift correction is applied to the X-band receiving frequency in order to counteract the calculated Doppler shift induced by Dawn's orbit around Vesta. However, the DSN utilizes a local oscillator to subtract the ephemeride Doppler shifting, and what persists is a low frequency component of error, which we observe is as much as 300 Hz. The offset frequency of the carrier signal is observed to decrease as the spacecraft moves further away from Earth during occultation entry—and as expected, increases as the spacecraft moves closer toward Earth after leaving occultation. Given that most of the BSR observations of occultations were conducted in one-way mode, the accuracy of the predicted receiving frequency was also diminished in the time leading up to and following these unique orbital geometries. Hence, when radar amplitude data is plotted against time, a change is observed in the overall envelope frequency of the sinusoidal amplitudes over the course of, for example, one minute, during which the carrier signal may shift from 200 Hz to 100 Hz. Notably, this frequency offset does not impact the relative Doppler shift between the surface echo and direct signal.

To seek surface echoes, the DSN I-and-Q amplitude time series data is converted into the frequency domain by taking the complex fast Fourier transform. The power frequency spectrum is generated in voltage-squared per Hz such that:

$$P_{\mathrm{spec}} = \frac{1}{t_{\mathrm{spec}}} \left| \mathrm{FFT}\left(A_I + iA_Q\right) \right|^2 \tag{1}$$

The duration t_{spec} over which to generate each power spectrum is selected only after assessing the theoretical Doppler separation δf between the direct signal and any surface echoes, as this dictates the frequency resolution necessary to accurately distinguish each surface echo. Background noise is smoothed by averaging power spectra together, but surface echo strength may be diminished in the process. The latter occurs when spectra are averaged over times that lack a surface echo signal or while the echo has changed in frequency. The final parameters used to generate power spectra are outlined at the end of the following section.

5.3. Calculating the Differential Doppler Shift

In order to verify the detection of surface reflections within BSR power spectra, the theoretical differential Doppler shift δf is calculated between the direct signal and grazing surface-reflected echoes, and compared with measured values. Theoretical δf is estimated from the known positions and line-of-sight velocities between (1) the Dawn spacecraft (D) at the time of transmission; (2) the center coordinate of the radar-illuminated surface on Vesta (Vpt) when the signal reaches the surface; and (3) the receiving antenna on Earth (E) after accounting for light travel time; each of which are each extracted from the reconstructed trajectory of Dawn's orbit that is provided in SPICE ephemeride data (Krening, Semenov & Acton, 2012).

For occultation entry during orbit 355, Supplementary Fig. 2 shows the instantaneous total velocities v of Dawn, the surface point of reflection on Vesta (hereafter referred to as "the echo site" or "the site"), and the receiving antenna on Earth within the bistatic plane—defined as the plane containing all three bodies at a given moment (Willis & Griffiths, 2007). All positions and velocities of D, Vpt and E are obtained with respect to Vesta's inertial frame of reference, such that the origin of the Cartesian coordinate system is Vesta's center of gravity and Vesta's equator defines the xy-plane. The individual components of each body's instantaneous velocity is listed in Supplementary Table 2 for occultation entry during orbit 355, where each velocity v_A is given in m s^{-1} along the line of sight with respect to the position $\hat{r}_B$. Velocity components are defined to be positive if body A is moving toward target B, and negative if away. For example, the notation $v_D\ \hat{r}_{Vpt} =$ -82.2 m s^{-1} (column 2, row 4) indicates that Dawn is traveling away from the echo site at a speed of 82.2 m s^{-1}.

The differential Doppler shift δf between the surface echo and direct signal is calculated by:

$$\delta f = \Delta f_{\text{echo}} - \Delta f_{\text{direct}} \tag{2}$$

where the absolute Doppler shift Δf of the direct signal or surface echo depends on the relative velocity of the transmitting and receiving bodies along their line of sight as described by Simpson (1993). Supplementary Table 3 shows the mathematical definition and calculation of individual contributions to the total theoretical differential Doppler shift (δf_{total}) between the surface echo and direct signal, which are the result of motions along the line of sight between Dawn and Earth (column 1), Dawn's orbital motion around Vesta (column 2), and Vesta's rotation (column 3).

The absolute Doppler shift of the direct signal $\Delta f_{\mathrm{direct}}$ is first calculated from the combination of Dawn's instantaneous line-of-sight velocity toward the receiving antenna on Earth ($v_D\ \hat{r}_E$), and Earth's line-of-sight velocity toward Dawn's position ($v_E\ \hat{r}_D$). The differential Doppler shift due to Dawn's orbital motion ($\delta f_{\mathrm{orbit}}$) is then calculated from the Doppler shift contributed by $v_D\ \hat{r}_{Vpt}$ and its difference from $\Delta f_{\mathrm{direct}}$. In turn, the differential Doppler shift contributed by the rotation of Vpt ($\delta f_{\mathrm{rotation}}$) on Vesta's surface is calculated from the Doppler shift contributed by $v_{Vpt}\ \hat{r}_D$ and $v_{Vpt}\ \hat{r}_E$ and their difference from $\Delta f_{\mathrm{direct}}$. The combined Doppler shift contributions of $\delta f_{\mathrm{orbit}}$ and $\delta f_{\mathrm{rotation}}$ yield the total theoretical $\delta f_{\mathrm{total}}$, which is calculated to range from ~2 Hz, as listed in Supplementary Table 3, to as much as 20 Hz when considering uncertainties in spacecraft position and Vesta's rotational velocity (detailed further below in our error analysis). Hence, the surface echo during occultation entry of orbit 355 is calculated to have a frequency shift that ranges from ~2 to 20 Hz higher or lower than that of the received direct signal.

This calculation confirms that in the configuration of grazing incidence during occultation observations of Vesta by Dawn, and due to the spacecraft's low orbital velocity of 200 m s^{-1}, the frequency separation δf between surface echoes and the direct signal will be small. Higher frequency spectral resolution is therefore necessary to distinguish the Doppler shifted surface echoes from the direct signal at Vesta. However, this requires longer integration time of the observation. We chose 2.5-second integration time to obtain a frequency spectral resolution of ~0.4 Hz as a tradeoff between SNR, frequency drift and resolution. Our final frequency spectral analysis averages two 2.5-second looks, and repeats this calculation shifting the start time of the averaging by 1 second. The resulting spectra are exemplified for occultation entry and exit during orbit 355 in Supplementary Fig. 3, which shows the power received in both RCP (reproduced from Fig. 2) and in LCP.

5.4. *Calculating the Radar Cross Section at High Incidence*

In order to assess the surface's geophysical properties that contribute to the observed surface echoes, the radar cross section σ of Vesta's surface is calculated in m^2 from the bistatic radar equation (Willis & Griffiths, 2007). This parameter is defined as the effective surface area that isotropically scatters the same amount of power as the echo site on Vesta, such that larger values of σ are associated with stronger surface echoes. Assuming (1) each echo site has approximately the same surface area illuminated by radar and (2) are observed at the same geometry (89° incidence), relative differences in σ imply differences in geophysical properties of the surface.

The latter assumption is supported by excluding surface echoes that occurred in regions of high topographic variability with respect to the incident HGA beam diameter, where the illuminated surface area is estimated using a first-order spherical approximation to Vesta's surface. Notably, this approximation excludes the effects of shadowing and diffraction, which are difficult to quantify at grazing incidence, and does not account for deviations of Vesta's shape from the sphere within the large area illuminated by the HGA beam. Our first-order estimation yields an elongated radar footprint of ~51 km along the line-of-sight between Dawn's HGA and Earth's receiving antenna, and ~11 km in diameter perpendicular to the line-of-sight. Topographic variability is assessed by calculating the root-mean-square height h_{rms} using elevations from Vesta's digital terrain model (Preusker et al., 2016) within an 11.5° by 11.5° grid (~51 km x 51 km) centered on each echo site's coordinates, and must be sufficiently smaller than the incident 11-km beam diameter. Calculated h_{rms} range from 0.002 km to 0.13 km. All but one echo site had h_{rms} < 0.11 km (i.e. topographic variability of 1% of the incident beam diameter). The echo site of occultation entry during orbit 377 exceeded this criteria and is therefore excluded from the following analyses.

Since HGA transmissions are measured continuously throughout the minutes that precede and follow an occultation of the spacecraft behind Vesta, only engineering data is included in the raw telemetry, and DSN receiver calibration measurements are not included with the raw radar dataset. Because the BSR data are not calibrated in absolute voltage, calculating σ therefore requires calibrating the measured power to a known reference. This is made possible by calculating the theoretical received power of the direct signal $P_{\mathrm{r\,dir|calc}}$ in watts, and comparing with measured received power $P_{\mathrm{r\ dir|meas}}$ in data units. $P_{\mathrm{r\ dir|calc}}$ is calculated from the one-way radar equation and depends on the transmitted power P_t, gain of the transmitting G_t and receiving G_r antennas, the distance R_{DE} between the transmitter aboard Dawn and the receiving antenna on Earth, and summed losses L. The one-way radar equation for $P_{\mathrm{r\ dir|calc}}$ [W] is then as follows (Willis & Griffiths, 2007):

$$P_{\mathrm{r\ dir|calc}} = \frac{P_t G_t G_r \lambda^2}{(4\pi R_{DE})^2 L} \tag{3}$$

where the nominal range of each parameter—except for time-dependent R_{DE}—is provided in Supplementary Table 1. Note that losses contributed by the DSN 70-m antennas are published in the telecommunications parameters of the Deep Space 1 mission (Taylor et al., 2001).

$P_{\mathrm{r\ dir|meas}}$ is evaluated by measuring the area under the curve in non-logarithmic units during a time when the direct signal is not obstructed by Vesta. Since the data is discrete, $P_{\mathrm{r\ dir|meas}}$ is the sum of the power in each frequency bin multiplied by the width of each frequency bin (subtracted by the noise power in the same bandwidth):

$$P_{\mathrm{r\ dir|meas}} = \left(\sum P_i \cdot \Delta f_{\mathrm{step}}\right) - \overline{P_N} \cdot f_{BW} \tag{4}$$

where frequency step Δf_{step} is the spectral resolution of ~0.4 Hz, as previously determined when calculating the differential Doppler shift; P_i is the non-logarithmic power in data units of each discrete point measured within a 10-Hz bandwidth (f_{BW}) of the direct signal peak; and $\overline{P_N}$ is the average noise power (data units/Hz) in the spectrum. The conversion factor between watts and power measured from BSR data units is therefore:

$$C_{\mathrm{ToWatts}} = \frac{P_{\mathrm{r\ dir|calc}}[\mathrm{Watts}]}{P_{\mathrm{r\ dir|meas}}[\mathrm{Data\ Units}]} \tag{5}$$

and the bistatic radar equation, solved for σ, is then:

$$\sigma_{(\mathrm{m}^2)} = \frac{(4\pi)^3 R_t^2 R_r^2 L}{G_t G_r \lambda^2}\left(\frac{P_{\mathrm{r\ echo|meas}}}{(1 - X_{P_t})P_t}\right) \tag{6}$$

where X_{Pt} is the fraction of incident power that has been reduced due to partial obstruction of the HGA beam by Vesta's surface, and $P_{\mathrm{r\ echo|meas}}$[W] = $P_{\mathrm{r\ echo|meas}}$[Data Units] × C_{ToWatts}. By measuring the received direct signal $P_{\mathrm{r\ dir|meas}}$ at a time close to each measured surface echo—10 seconds before a given occultation entry, and 10 seconds after an occultation exit—we minimize variations in the transmitting and receiving system characteristics, including changes in the HGA's pointing accuracy, and potential differences in DSN receiver losses due to the use of different receiving stations with different system temperatures and atmospheric conditions. Hence, the measurement of the radar cross section σ (m^2) becomes independent of P_t, G_t, G_r, L and λ, such that:

$$\sigma_{(m^2)} = \frac{(4\pi)^3 R_{DVpt}{}^2 R_{EVpt}{}^2}{(1-X_{P_t}) R_{DE}{}^2} \left(\frac{P_{\text{r echo|meas}}}{P_{\text{r dir|meas}}} \right) \tag{7}$$

where R_{DVpt} is the distance between the transmitter aboard Dawn and the echo site on Vesta's surface at the time of the observed surface echo; R_{EVpt} is the distance between the receiving antenna on Earth and the echo site at the time of the observed surface echo; and R_{DE} is the distance between Dawn's HGA and the receiver on Earth at the time when $P_{\text{r dir|meas}}$ is measured (10 seconds before occultation entries, and 10 seconds after occultation exits).

Typically, the radar cross section is then normalized to the areal extent illuminated by the radar (σ^0), and is reported in regime of diffuse backscatter due to the use of Earth-based radar antennas as both transmitter and receiver for many observations (e.g., Mitchell et al., 1996)—where at increasingly high angles of incidence, the diffuse component of radar backscatter dominates the received signal (Thompson, Ustinov & Heggy, 2011). BSR observations at Vesta are conducted in the forward scatter regime, however, whereby radar waves predominantly scatter in the forward direction and almost entirely within the plane of incidence (Willis & Griffiths, 2007). In this regime, the polarization of a circularly transmitted wave is also conserved in major part even after reflection from the target's surface (Harmon, 2008). Dawn's measurements of σ^0 on Vesta's surface are therefore not directly comparable with those observed in the backscatter regime on other planetary bodies.

While the lack of comparability might be overcome by deriving surface roughness from σ^0, two sources of uncertainty remain: (1) the absolute surface area contributing to forward-scattered surface echoes is difficult to quantify due to the effects of shadowing and multiple scattering that become important at such high, grazing incidence (Tyler et al., 2001); and (2) there is no appropriate scattering model to address the impact of wavelength-scale surface roughness on radar reflections at grazing angles of incidence approaching 90° (Ogilvy, 1991).

Instead, we calculate relative σ across Vesta's surface with respect to the strongest observed surface reflection σ_{max} by measuring σ when the direct signal is ~25 dB above the noise level for all surface echoes, and employ the assumption that the illuminated surface area is approximately equal for each site. Since incident power is also assumed equal for all surface echoes (and therefore X_{Pt} assumed constant for Equations 6 and 7), we estimate that at least 50% of the HGA beam is obscured behind Vesta's surface (X_{Pt} = 0.5) and report σ (km^2) as a lower limit for each echo site.

Under the above assumptions of equal incident power and equal surface area illuminated at 89° incidence, the relative strengths of surface echo reflections (σ/σ_{max}) can then be attributed to differences in the relative reflectivity of the surface material itself or variations in the roughness of the surface at the scale of the radar wavelength (Thompson, Ustinov & Heggy, 2011; Simpson et al., 2011). Potentially greater obstruction of the incident power would result in an increase of σ (km^2), but assuming equal obstruction for all surface echoes, this does not change the relative radar cross section (σ/σ_{max}).

5.5. Uncertainty in the Differential Doppler Shift

The primary sources of uncertainty in theoretical δf include the positions and velocities of (1) the spacecraft and (2) the radar-illuminated surface echo site on Vesta as listed in Supplementary Table 4. We assume that uncertainty in the position and velocity of Earth is negligible at such distances. For a given parameter $Y \pm \sigma_y$ that depends on multiple variables $X_i \pm \sigma_{x,i}$, we calculate σ_y by summing in quadrature the partial derivative of each contributing variable (∂X_i / ∂Y) multiplied by its uncertainty $\sigma_{x,i}$.

The position of the Dawn spacecraft is provided in Cartesian coordinates from SPICE ephemerides with an uncertainty of ±3 m in the radial, along-track and cross-track directions from the reconstructed trajectory of LAMO (Krening, Semenov & Acton, 2012), while the error in the position of the echo site on Vesta's surface is calculated from (1) uncertainty in the radius of the echo site from Vesta's center ± ~0.5 km—due to topography within the large surface area illuminated by the HGA beam at grazing incidence—and (2) uncertainty in the latitude and longitude of the echo site center by ± ~0.2°. Uncertainties in the geodetic coordinates of the echo site are then converted to Cartesian coordinates at a height above or below a reference triaxial ellipsoid—which is defined using the best-fit ellipsoid derived from Hubble light-curve observations of Vesta, where R_x = 289 km, R_y = 280 km and R_z = 229 km (Thomas et al., 1997; Krening, Semenov & Acton, 2012). Uncertainties in the x, y and z coordinates of the echo site for occultation entry of orbit 355 are on the order of ~0.7 km for the occultation entry of orbit 355.

With regard to spacecraft velocity, the SPICE ephemerides containing Dawn's state vector were released by the optical navigation team in 2012 (Krening, Semenov & Acton, 2012) before the peer-reviewed publication of Vesta's gravitational solution in 2014 (Konopliv et al., 2014). Hence, Dawn's reconstructed trajectory does not include variations in orbital velocity due to the heterogeneous gravity field that exhibits accelerations between –1000 mGal and +2000 mGal (–1 cm s^{-2} and +2 cm s^{-2}) relative to the homogeneous model (Konopliv et al., 2014). Since each frequency spectrum produced in our BSR analysis is averaged over 5-second observations, unpredicted gravitational accelerations contribute –5 to +10 cm s^{-1} uncertainty in Dawn's velocity vector.

The rotational velocity of the echo site on Vesta's surface depends on the distance of the site from Vesta's center and the rotation period, the latter of which is known to high precision (Konopliv et al., 2014). Given the large extent of surface area illuminated by the HGA beam on Vesta, we use the radius at the center of the echo site to calculate a representative rotational velocity. During occultation entry of orbit 355, uncertainty of ±0.5 km in the radius yields an uncertainty of ±16 cm s^{-1} in the echo site's rotational velocity.

Using the above-derived uncertainties in the positions and velocities of each body, we calculate the propagation of error into each line-of-sight velocity between Dawn, the surface echo site on Vesta, and the antenna on Earth that contribute to the calculation of theoretical δf. Uncertainty in the velocity of body A projected along the line of site with body B ($v_A\, \hat{r}_B$) is calculated from the propagation of error in (1) the velocity vector of A, (2) the position of A, and (3) the position of B. Hence, the theoretical differential Doppler shift is calculated to range between ~2 and 20 Hz, and is consistent the observed δf of –12 Hz (Fig. 1b) for the surface echo measured during orbit 355, occultation entry.

5.6. *Uncertainty in the Absolute and Relative Radar Cross Section*

The primary sources of uncertainty in the radar cross section include (1) HGA pointing error, (2) uncertainty in the measurement of received power, (3) uncertainty in the position of the Dawn spacecraft, and (4) uncertainty in the position of the echo site center—where the latter two uncertainties have been previously quantified above.

When outside of occultation, the measured power received from the direct signal $P_{\mathrm{r\ dir|meas}}$ varies as a result of HGA antenna pointing inaccuracy due to unpredicted uneven gravitational torques on the spacecraft's large solar panels while in Vesta's microgravity environment (Kennedy et al., 2013). The spacecraft's reaction wheels are used to counteract accumulated spacecraft pointing errors, but one of the four wheels failed prior to Dawn's arrival at Vesta (Kennedy et al., 2013). Furthermore, corrections only occurred once every 1-3 days during LAMO, such that antenna pointing error increased steadily from zero to ~0.4° between corrections, and even exceeded 1.0° on a few occasions (Kennedy et al., 2013). To quantify fluctuations in the direct signal power on the order of tens of seconds near the time of each surface echo observation, we measure the variation of $P_{\mathrm{r\ dir|meas}}$ over 30 seconds preceding an occultation entry (and over 30 seconds following an occultation exit). We find that $P_{\mathrm{r\ dir|meas}}$ varies less than ±2% for 11 of the 14 occultation observations but as much as ±8% before occultation entry of orbit 719.

The standard error in the measurement of $P_{\mathrm{r\ echo|meas}}$ and $P_{\mathrm{r\ dir|meas}}$ are quantified by deviations of noise power from the mean. We compute the standard deviation of noise in a given spectrum over frequencies where no signal is present (from –6 kHz to –1 kHz and from 1 kHz to 6 kHz), and find that the standard deviation of a given spectrum ranges from ~$0.14\overline{P_N}$ to $0.17\overline{P_N}$. We use the upper limit of $0.17\overline{P_N}$ as a conservative estimate for all uncertainties in power measurement.

Together, the above errors in HGA antenna pointing, measurement of received power, spacecraft position and echo site position amount to uncertainties in σ (km^2) that range from

1% to 10% depending on the surface echo—see Table 1. Subsequent error in the relative radar cross section (σ/σ_{max}) range from zero dB for the strongest surface echo reflection to ±0.5 dB for the weakest surface echo reflection.

6. Data Availability

Raw telemetry data from Dawn's orbital bistatic radar (BSR) experiment at Vesta were generated from receiver output at stations of the NASA Deep Space Network (DSN) and are managed by the NASA Jet Propulsion Laboratory of the California Institute of Technology. The unprocessed time-domain BSR amplitude data used in this study are available upon request from the corresponding author.

7. Acknowledgements

The authors thank the NASA JPL Radar Tracking Group for acquiring Dawn's bistatic radar data, with special thanks to Daniel Kahan and Sami Asmar for many helpful discussions about the resulting data product. Dr. Mahta Moghaddam (USC) is greatly appreciated for sharing her expertise in bistatic radar surface scattering during the final stages of the manuscript. We also thank Dr. Steven Joy (UCLA) for providing us with ephemeris data from SPICE kernels and Dawn PI Dr. Christopher Russell (UCLA) for enabling this experiment. Lastly, we thank Deputy PI Dr. Carol Raymond (JPL) and the Dawn Operations Team for their support throughout the experiment. Palmer was previously funded as a graduate student by UCLA, the California Institute of Technology and Western Michigan University. This work is currently funded through USC under the NASA Planetary Geology and Geophysics program (WBS 811073.02.01.07.05).

8. References

Butler, B. J., Muhleman, D. O. & Slade, M. A. (1993). "Mercury: full-disk radar images and the detection and stability of ice at the North Pole." *J. Geophys. Res.*, **98**(E8), 15003. doi:10.1029/93JE01581

Campbell, B. A., Carter, L. M., Campbell, D. B., Nolan, M., Chandler, J., Ghent, R. R., Ray Hawke, B., Anderson, R. F. & Wells, K. (2010). "Earth-based 12.6-cm wavelength radar mapping of the Moon: New views of impact melt distribution and mare physical properties.” *Icarus*, **208**(2), 565–573. doi:10.1016/j.icarus.2010.03.011

Capria, M. T., Tosi, F., De Sanctis, M. C., Capaccioni, F., Ammannito, E., Frigeri, A., Zambon, F., Fonte, S., Palomba, E., Turrini, D., Titus, T. N., Schröder, S. E., Toplis, M., Li, J.-Y., Combe, J.-P., Raymond, C. A. & Russell, C. T. (2014). “Vesta surface thermal properties map.” *Geophys. Res. Lett.*, **41**(5), 1438–1443. doi:10.1002/2013GL059026

Chen, C.-C., Makovsky, A., Shambayati, S., Taylor, F. H., Herman, M. I., Zingales, S. H., Siemsen, K. & Nuckolls, C. (2000). *Small Deep Space Transponder (SDST) DS1 Technology Validation Report* (JPL Publication 00-10 No. 11), Pasadena, California: Jet Propulsion Laboratory, California Institute of Technology.

De Sanctis, M. C., Combe, J.-P., Ammannito, E., Palomba, E., Longobardo, A., McCord, T. B., Marchi, S., Capaccioni, F., Capria, M. T., Mittlefehldt, D. W., Pieters, C. M., Sunshine, J., Tosi, F., Zambon, F., Carraro, F., Fonte, S., Frigeri, A., Magni, G., Raymond, C. A., Russell, C. T. & Turrini, D. (2012). “Detection of Widespread Hydrated Minerals on Vesta by the VIR Imaging Spectrometer On Board the Dawn Mission.” *Astrophys. J.*, **758**(2), L36. doi:10.1088/2041-8205/758/2/L36

ElShafie, A. & Heggy, E. (2013). “Dielectric and hardness measurements of planetary analog rocks in support of in-situ subsurface sampling.” *Planet. Space Sci.*, **86**, 150–154. doi:10.1016/j.pss.2013.02.003

Fjeldbo, G., Kliore, A. & Seidel, B. (1972). “Bistatic radar measurements of the surface of Mars with Mariner 1969.” *Icarus*, **16**(3), 502–508. doi:10.1016/0019-1035(72)90096-6

Grasset, O., Dougherty, M. K., Coustenis, A., Bunce, E. J., Erd, C., Titov, D., Blanc, M., Coates, A., Drossart, P., Fletcher, L. N., Hussmann, H., Jaumann, R., Krupp, N., Lebreton, J.-P., Prieto-Ballesteros, O., Tortora, P., Tosi, F. & Van Hoolst, T. (2013). “JUpiter ICy moons Explorer (JUICE): An ESA mission to orbit Ganymede and to characterise the Jupiter system.” *Planet. Space Sci.*, **78**, 1–21. doi:10.1016/j.pss.2012.12.002

Harmon, J. K. (2008). “Radar Imaging of Mercury.” In A. Balogh, L. Ksanfomality & R. von Steiger, eds., *Mercury*, New York, NY: Springer New York, pp. 125–167. doi:10.1007/978-0-387-77539-5_7

Heggy, E., Palmer, E. M., Kofman, W., Clifford, S. M., Righter, K. & Hérique, A. (2012). "Radar properties of comets: Parametric dielectric modeling of Comet 67P/Churyumov-Gerasimenko." *Icarus*, **221**(2), 925–939. doi:10.1016/j.icarus.2012.09.023

Herique, A., Kofman, W., Beck, P., Bonal, L., Buttarazzi, I., Heggy, E., Lasue, J., Levasseur-Regourd, A. C., Quirico, E. & Zine, S. (2016). "Cosmochemical implications of CONSERT permittivity characterization of 67P/CG." *Mon. Not. R. Astron. Soc.*, **462**(5), S516–S532. doi:10.1093/mnras/stx040

Kennedy, B., Abrahamson, M., Ardito, A., Han, D., Haw, R., Mastrodemos, N., Nandi, S., Park, R. & Vaughan, A. (2013). "Dawn Orbit Determination Team: Trajectory and Gravity Prediction Performance during Vesta Science Phases." In S. Tanygin, R. S. Park, T. F. Starchville, Jr. & L. K. Newman, eds., *Advances in the Astronautical Sciences: Spaceflight Mechanics 2013*, Vol. 148, Kauai, Hawaii: Univelt Inc., pp. 2231-2250 (AAS 13–345).

Konopliv, A. S., Asmar, S. W., Bills, B. G., Mastrodemos, N., Park, R. S., Raymond, C. A., Smith, D. E. & Zuber, M. T. (2012). "The Dawn Gravity Investigation at Vesta and Ceres." In C. Russell & C. Raymond, eds., *The Dawn Mission to Minor Planets 4 Vesta and 1 Ceres*, New York, NY: Springer New York, pp. 461-486. doi:10.1007/978-1-4614-4903-4_15

Konopliv, A. S., Asmar, S. W., Park, R. S., Bills, B. G., Centinello, F., Chamberlin, A. B., Ermakov, A., Gaskell, R. W., Rambaux, N., Raymond, C. A., Russell, C. T., Smith, D. E., Tricarico, P. & Zuber, M. T. (2014). "The Vesta gravity field, spin pole and rotation period, landmark positions, and ephemeris from the Dawn tracking and optical data." *Icarus*, **240**, 103–117. doi:10.1016/j.icarus.2013.09.005

Krening, S. C., Semenov, B. V. & Acton, C. H. (2012). "DAWN SPICE KERNELS V1.0, DAWN-M/A-SPICE-6-V1.0," NASA Planetary Data System.

Mitchell, D. L., Ostro, S. J., Hudson, R. S., Rosema, K. D., Campbell, D. B., Vélez, R., Chandler, J. F., Shapiro, I. I., Giorgini, J. D. & Yeomans, D. K. (1996). "Radar Observations of Asteroids 1 Ceres, 2 Pallas, and 4 Vesta." *Icarus*, **124**(1), 113–133. doi:10.1006/icar.1996.0193

Nozette, S., Lichtenberg, C. L., Spudis, P., Bonner, R., Ort, W., Malaret, E., Robinson, M. & Shoemaker, E. M. (1996). "The Clementine Bistatic Radar Experiment." *Science*, **274**(5292), 1495–1498. doi:10.1126/science.274.5292.1495

Ogilvy, J. A. (Ed.). (1991). *Theory of Wave Scattering From Random Rough Surfaces,* Bristol, England: Adam Hilger.

Palmer, E. M., Heggy, E., Capria, M. T. & Tosi, F. (2015). "Dielectric properties of Asteroid Vesta's surface as constrained by Dawn VIR observations." *Icarus*, **262**, 93–101. doi:10.1016/j.icarus.2015.08.031

Patterson, G. W., Stickle, A. M., Turner, F. S., Jensen, J. R., Bussey, D. B. J., Spudis, P., Espiritu, R. C., Schulze, R. C., Yocky, D. A., Wahl, D. E., Zimmerman, M., Cahill, J. T. S., Nolan, M., Carter, L., Neish, C. D., Raney, R. K., Thomson, B. J., Kirk, R., Thompson, T. W., Tise, B. L., Erteza, I. A. & Jakowatz, C. V. (2017). "Bistatic radar observations of the Moon using Mini-RF on LRO and the Arecibo Observatory." *Icarus*, **283**, 2–19. doi:10.1016/j.icarus.2016.05.017

Pätzold, M., Häusler, B., Aksnes, K., Anderson, J. D., Asmar, S. W., Barriot, J.-P., Bird, M. K., Boehnhardt, H., Eidel, W., Grün, E., Ip, W. H., Marouf, E., Morley, T., Neubauer, F. M., Rickman, H., Thomas, N., Tsurutani, B. T., Wallis, M. K., Wickramasinghe, N. C., Mysen, E., Olson, O., Remus, S., Tellmann, S., Andert, T., Carone, L., Fels, M., Stanzel, C., Audenrieth-Kersten, I., Gahr, A., Müller, A.-L., Stupar, D. & Walter, C. (2007). "Rosetta Radio Science Investigations (RSI)." *Space Sci. Rev.*, **128**(1–4), 599–627. doi:10.1007/s11214-006-9117-7

Pérez-Ayúcar, M., Lorenz, R. D., Floury, N., Prieto-Cerdeira, R. & Lebreton, J.-P. (2006). "Bistatic observations of Titan's surface with the Huygens probe radio signal." *J. Geophys. Res. Planet.*, **111**(E7). doi:10.1029/2005JE002613

Prettyman, T. H., Mittlefehldt, D. W., Yamashita, N., Lawrence, D. J., Beck, A. W., Feldman, W. C., McCoy, T. J., McSween, H. Y., Toplis, M. J., Titus, T. N., Tricarico, P., Reedy, R. C., Hendricks, J. S., Forni, O., Le Corre, L., Li, J.-Y., Mizzon, H., Reddy, V., Raymond, C. A. & Russell, C. T. (2012). "Elemental Mapping by Dawn Reveals Exogenic H in Vesta's Regolith." *Science*, **338**(6104), 242–246. doi:10.1126/science.1225354

Preusker, F., Scholten, F., Matz, K.-D., Jaumann, R., Raymond, C. A. & Russell, C. T. (2016). "DAWN FC2 DERIVED VESTA DTM SPG V1.0, DAWN-A-FC2-5-VESTADTMSPG-V1.0," NASA Planetary Data System.

Reddy, V., Le Corre, L., O'Brien, D. P., Nathues, A., Cloutis, E. A., Durda, D. D., Bottke, W. F., Bhatt, M. U., Nesvorny, D., Buczkowski, D., Scully, J. E. C., Palmer, E. M., Sierks, H., Mann, P. J., Becker, K. J., Beck, A. W., Mittlefehldt, D., Li, J.-Y., Gaskell, R., Russell, C. T., Gaffey, M. J., McSween, H. Y., McCord, T. B., Combe, J.-P. & Blewett, D. (2012). "Delivery of dark material to Vesta via carbonaceous chondritic impacts." *Icarus*, **221**(2), 544–559. doi:10.1016/j.icarus.2012.08.011

Russell, C. T. & Raymond, C. A. (2012). "The Dawn Mission to Vesta and Ceres." In C. Russell & C. Raymond, eds., *The Dawn Mission to Minor Planets 4 Vesta and 1 Ceres*, New York, NY: Springer New York, pp. 3–23. doi:10.1007/978-1-4614-4903-4_2

Scully, J. E. C., Russell, C. T., Yin, A., Jaumann, R., Carey, E., Castillo-Rogez, J., McSween, H. Y., Raymond, C. A., Reddy, V. & Le Corre, L. (2015). "Geomorphological evidence for transient water flow on Vesta." *Earth Planet. Sci. Lett.*, **411**, 151–163. doi:10.1016/j.epsl.2014.12.004

Shepard, M. K., Campbell, B. A., Bulmer, M. H., Farr, T. G., Gaddis, L. R. & Plaut, J. J. (2001). "The roughness of natural terrain: A planetary and remote sensing perspective." *Journal of Geophysical Research: Planets*, **106**(E12), 32777–32795. doi:10.1029/2000JE001429

Simpson, R. & Tyler, G. L. (2001). "Mars Global Surveyor Bistatic Radar Probing of the MPL/DS2 Target Area." *Icarus*, **152**(1), 70–74. doi:10.1006/icar.2001.6629

Simpson, R. A. (1993). "Spacecraft studies of planetary surfaces using bistatic radar." *IEEE T. Geosci. Remote*, **31**(2), 465–482. doi:10.1109/36.214923

Simpson, R. A., Tyler, G. L., Häusler, B., Mattei, R. & Pätzold, M. (2009). "Venus Express bistatic radar: High-elevation anomalous reflectivity." *J. Geophys. Res.*, **114**. doi:10.1029/2008JE003156

Simpson, R. A., Tyler, G. L., Pätzold, M., Häusler, B., Asmar, S. W. & Sultan-Salem, A. K. (2011). "Polarization in Bistatic Radar Probing of Planetary Surfaces: Application to Mars Express Data." *Proc. IEEE*, **99**(5), 858–874. doi:10.1109/JPROC.2011.2106190

Taylor, J. (2009). *Dawn Telecommunications* (DESCANSO Article No. 13), Pasadena, California: NASA Jet Propulsion Laboratory, California Institute of Technology.

Taylor, J., Fernández, M. M., Alamanac, A. I. B. & Cheung, K.-M. (2001). *Deep Space 1 Telecommunications* (DESCANSO Article No. 2), Pasadena, California: NASA Jet Propulsion Laboratory, California Institute of Technology.

Thomas, P. C., Binzel, R. P., Gaffey, M. J., Storrs, A. D., Wells, E. N. & Zellner, B. H. (1997). "Impact Excavation on Asteroid 4 Vesta: Hubble Space Telescope Results." *Science*, **277**(5331), 1492–1495. doi:10.1126/science.277.5331.1492

Thomas, V. C., Makowski, J. M., Brown, G. M., McCarthy, J. F., Bruno, D., Cardoso, J. C., Chiville, W. M., Meyer, T. F., Nelson, K. E., Pavri, B. E., Termohlen, D. A., Violet, M. D. & Williams, J. B. (2011). "The Dawn Spacecraft." *Space Sci. Rev.*, **163**(1–4), 175–249. doi:10.1007/s11214-011-9852-2

Thompson, T. W., Masursky, H., Shorthill, R. W., Tyler, G. L. & Zisk, S. H. (1974). "A comparison of infrared, radar, and geologic mapping of lunar craters." *The Moon*, **10**(1), 87–117. doi:10.1007/BF00562019

Thompson, T. W., Ustinov, E. A. & Heggy, E. (2011). "Modeling radar scattering from icy lunar regoliths at 13 cm and 4 cm wavelengths." *J. Geophys. Res.*, **116**(E1). doi:10.1029/2009JE003368

Tyler, G. L., Balmino, G., Hinson, D. P., Sjogren, W. L., Smith, D. E., Simpson, R. A., Asmar, S. W., Priest, P. & Twicken, J. D. (2001). "Radio science observations with Mars Global Surveyor: Orbit insertion through one Mars year in mapping orbit." *J. Geophys. Res. Planet.*, **106**(E10), 23327–23348. doi:10.1029/2000JE001348

Tyler, G. L., Eshleman, V. R., Fjeldbo, G., Howard, H. T. & Peterson, A. M. (1967). "Bistatic-Radar Detection of Lunar Scattering Centers with Lunar Orbiter I." *Science*, **157**(3785), 193–195. doi:10.1126/science.157.3785.193

Williams, D. A., Jaumann, R., McSween, H. Y., Marchi, S., Schmedemann, N., Raymond, C. A. & Russell, C. T. (2014). "The chronostratigraphy of protoplanet Vesta." *Icarus*, **244**, 158–165. doi:10.1016/j.icarus.2014.06.027

Williams, D. A., Yingst, R. A. & Garry, W. B. (2014). "Introduction: The geologic mapping of Vesta." *Icarus*, **244**, 1–12. doi:10.1016/j.icarus.2014.03.001

Willis, N. J. & Griffiths, H. D. (Eds.). (2007). *Advances in Bistatic Radar*, Raleigh, NC: Scitech Publishing.

9. Supplementary Material

Supplementary Table 1. Dawn bistatic radar acquisition parameters at asteroid Vesta.

Transmitter		
Dawn Spacecraft High-Gain Communications Antenna		
Power P_t	100 ± 0.03 W	(Taylor, 2009)
Wavelength λ	3.55 cm	(Taylor, 2009)
Frequency f	8.435 GHz (X-Band)	(Taylor, 2009)
Polarization	RCP	(Taylor, 2009)
Gain G_t	39.60 ± 0.25 dBi	(Taylor, 2009)
Total loss L:	–2.20 dB ± 0.10 dB	
HGA transmit circuit loss	–0.41 ± 0.057 dB	(Taylor, 2009)
HGA degrees-off-boresight loss	–1.40 ± 0.026 dB	(Taylor, 2009)
Atmospheric attenuation loss	–0.07 ± 0.00 dB	(Taylor et al., 2001)
DSN 70-m antenna pointing loss	–0.10 ± 0.057 dB	(Taylor et al., 2001)
DSN 70-m polarization loss	–0.20 ± 0.057 dB	(Taylor et al., 2001)
FWHM beamwidth θ_{bw}	~1.6°	(Taylor, Cheung & Wong, 2001)
Angle of incidence θ_i	~89°	
Receiver		
Earth Deep Space Network 70-m Antennas		
Gain G_r	74.6 ± 0.2 dBi	(Slobin, 2015)
Polarization	RCP and LCP	(Slobin, 2015)
Sampling rate	16,000 samples/s	
Total System Noise Temperature T_{sys}:	22.9 ± 1.6 K	
T_{sys} in vacuum at zenith	11.7 ± 1.4 K	(Slobin, 2015)
due to elevation (lowest limit, 25°)	7 K	(Slobin, 2015)
due to atmosphere	3.3 ± 1.2 K	(Slobin, 2015)
due to Sun	0.89 K	(Taylor, 2009)
due to other hot bodies	0.00 K	(Taylor, 2009)

Supplementary Table 2. Instantaneous velocities of Dawn (*D*), the echo site on Vesta (*Vpt*) and the receiving antenna on Earth (*E*) during occultation entry, orbit 355 at 03:47:06 UTC.

Component of velocity vector	v_D (m s^{-1})	v_{Vpt} (m s^{-1})	v_E (m s^{-1})
Total in bistatic plane	84.4	96.5	39600
$\hat{r}_D$	–	-86.7	-20396
$\hat{r}_{Vpt}$	-82.2	–	-20396
$\hat{r}_E$	-82.6	86.0	–

v_A : velocity (positive when moving toward the target) — $\hat{r}_B$: radial unit vector from body A toward target B

Supplementary Table 3. Individual contributions to the differential Doppler shift δf_{total} between the direct and echo signals due to the relative motions of the receiver, transmitter and target—i.e., due to the Earth-based receiving antenna (Δf_{direct}), the motion of the Dawn spacecraft (δf_{orbit}) and Vesta's rotation ($\delta f_{\text{rotation}}$).

Δf_{direct}	δf_{orbit}	$\delta f_{rotation}$	δf_{total}
$\frac{1}{\lambda}(v_D\ \hat{r}_E + v_E\ \hat{r}_D)$	$\frac{1}{\lambda}(v_D\ \hat{r}_{Vpt}) - \Delta f_{\text{direct}}$	$\frac{1}{\lambda}(v_{Vpt}\ \hat{r}_D + v_{Vpt}\ \hat{r}_E) - \Delta f_{\text{direct}}$	$\delta f_{orbit} + \delta f_{rotation}$
–584,434 Hz	–9 Hz	+7 Hz	–2 Hz

**Negative differential Doppler shifts indicate a decrease in frequency (motion away from the observer), such that the surface echo reflection has a greater path length to Earth than the direct signal during occultation entry.*

Supplementary Table 4. Sources of uncertainty in the calculation of theoretical δf and σ (km^2).

Parameter	Uncertainty	Description
Position of Dawn r_D	± 3 m	Uncertainty in LAMO reconstructed trajectory (Krening, Semenov & Acton, 2012)
Radius of echo site R_{Vpt}	± 0.5 km	Due to variation in topography within the large radar-illuminated echo site
Latitude of echo site center	± 0.2°	Estimated uncertainty
Longitude of echo site center	± 0.2°	Estimated uncertainty
Measured surface echo power $P_{\text{r echo}\mid\text{meas}}$	± 0.17 $\overline{P_{\text{N echo}}}$	Due to standard deviation of noise power
Measured direct power $P_{\text{r dir}\mid\text{meas}}$	± 0.17 $\overline{P_{\text{N dir}}}$	Due to standard deviation of noise power

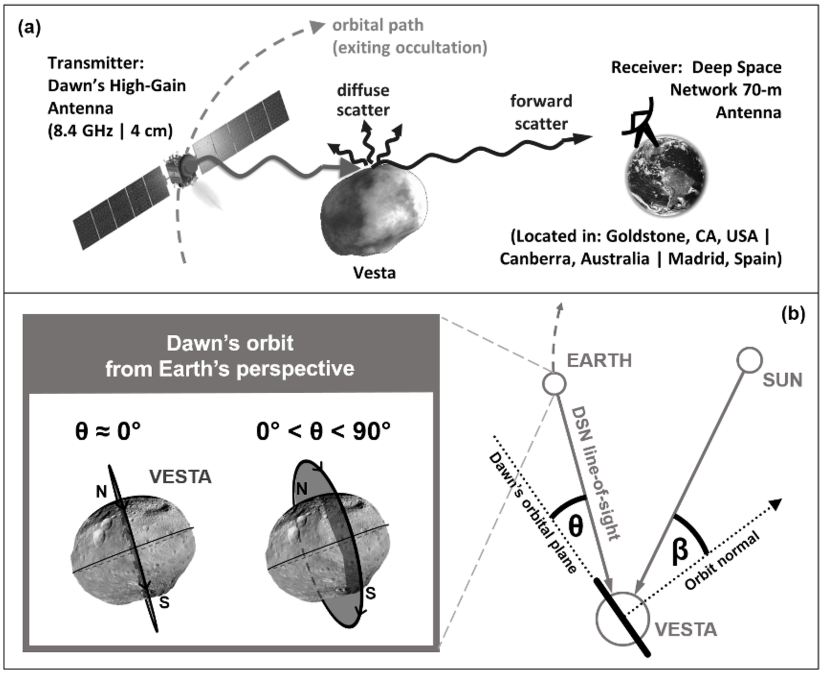

Supplementary Figure 1. Typical orbital geometry of Dawn spacecraft during bistatic radar observations of Vesta (not to scale). In panel (a), Dawn's HGA transmits radio waves during exit from occultation, which then scatter in all directions from Vesta's surface at the echo reflection site. Forward-scattered radio waves are then received at one of the DSN antennas on Earth. Panel (b) illustrates surface reflections occur from mid-latitudes on Vesta even though Dawn is in a polar orbit. Angle β is fixed at 45° to ensure that solar panels are under constant illumination and to maximize the visibility of Vesta's sunlit surface for spectroscopic and framing camera (FC) imaging. From the view of Earth-based receiving antennas, Dawn's orbital plane is tilted by angle θ that varies with the orbits of Earth and Vesta around the Sun, such that $0° < \theta < 90°$. Since Dawn's HGA is constantly pointed at Earth, surface radar reflections occur along mid-latitudes rather than from Vesta's poles.

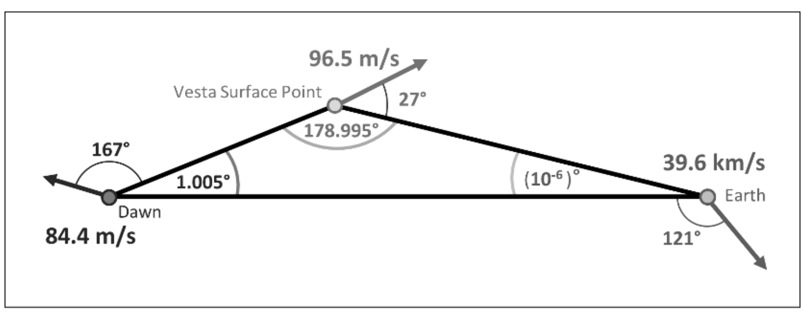

Supplementary Figure 2. Relative motion in the bistatic plane of Dawn's HGA, the Earth-based receiver Vesta's point of surface reflection during orbit 355 occultation entry. Velocities are expressed in Vesta's inertial frame of reference. The theoretical relative Doppler shift between the surface echo and direct signal ranges from ~2 to 20 Hz.

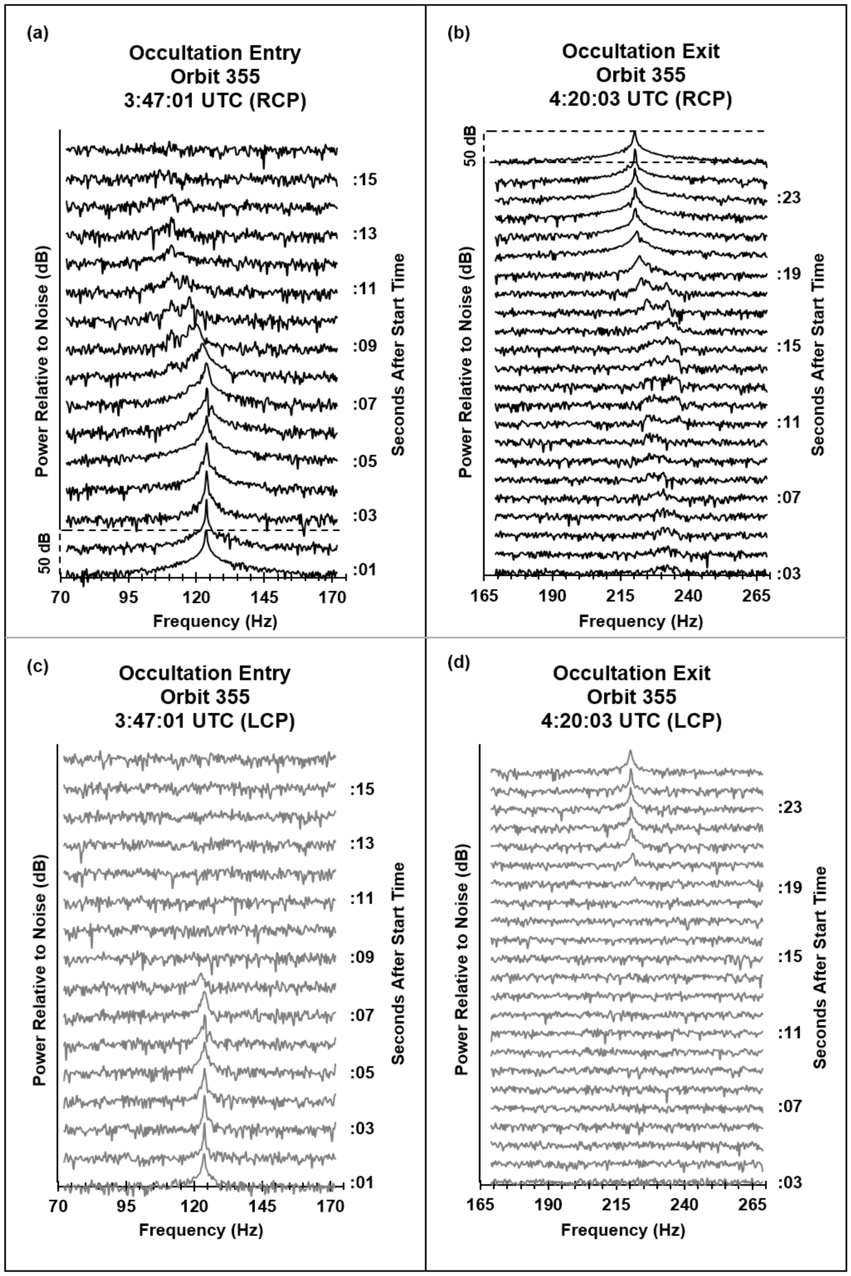

Supplementary Figure 3. Received signal in right- and left-hand circular polarization (RCP and LCP) during (a, c) occultation entry and (b, d) exit during orbit 355. At grazing incidence, surface radar reflections are in the regime of forward scattering. Hence, polarization is conserved such that there is no measurable LCP component in surface radar reflections from Vesta. The presence of LCP power (c, d) in the direct signal is the result of imperfection in the transmitting antenna and the high sensitivity of the DSN receiving system. At its maximum strength, the LCP component of the direct signal is 36 dB above the noise level (i.e. 2.6% of the power measured in RCP).

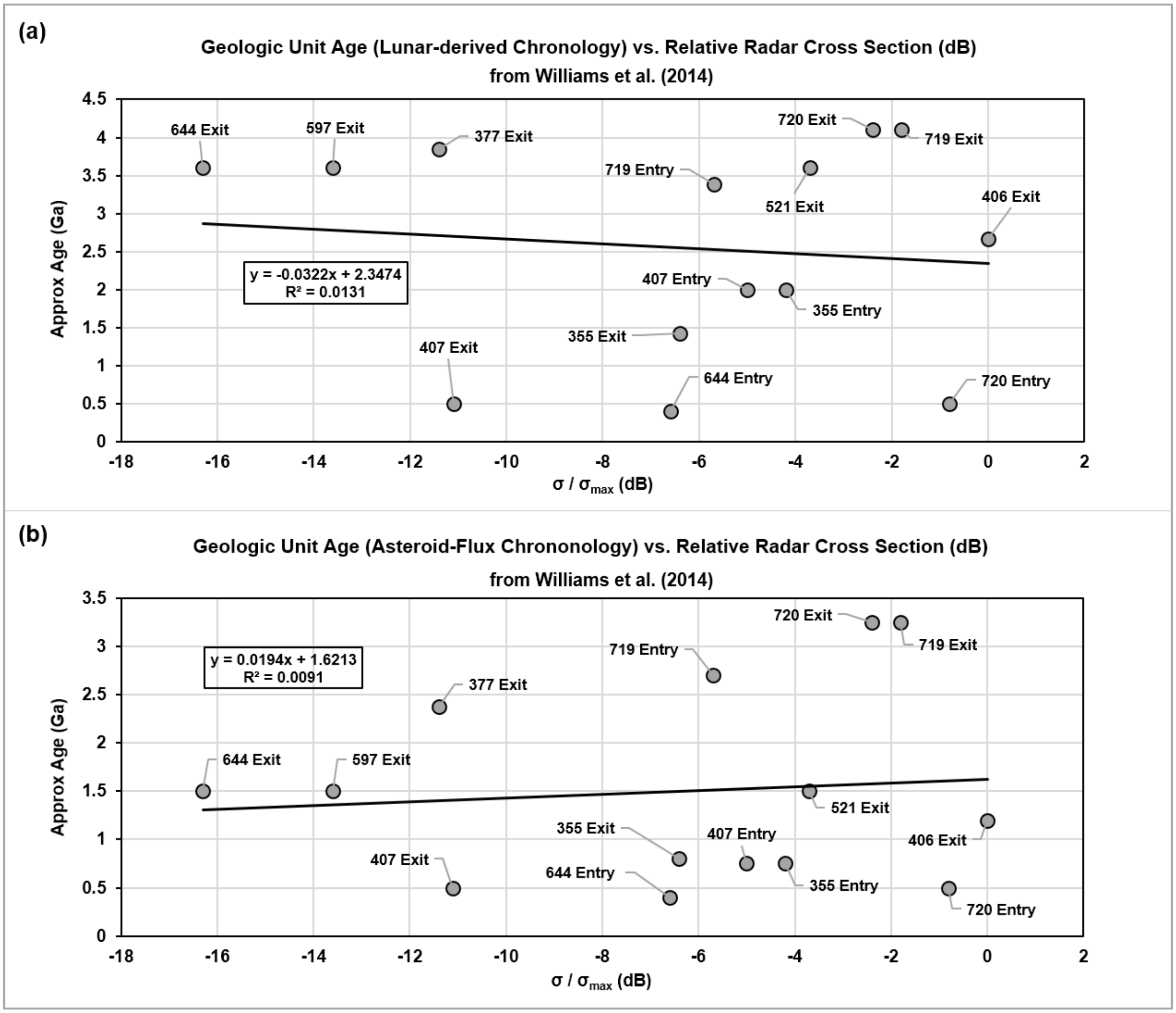

Supplementary Figure 4. Comparison of geologic unit age (Williams et al., 2014) with radar forward-scattering properties at each echo site on Vesta. Panel (a) plots geologic unit ages derived from lunar chronology while plot (b) shows surface ages derived from asteroid-flux chronology. Relative radar forward-scatter cross section (σ/σ_{max}) is calculated for each surface echo with respect to the site of strongest surface echo reflection (occultation exit of orbit 406). Since strong reflections are interpreted to come from smooth surfaces, lower values of (σ/σ_{max}) suggest rougher surfaces than the reference site. Unlike the Moon, Vesta does not exhibit a strong correlation between centimeter-to-decimeter-scale radar scattering properties and surface age, as is shown by the low correlation factor *R*.

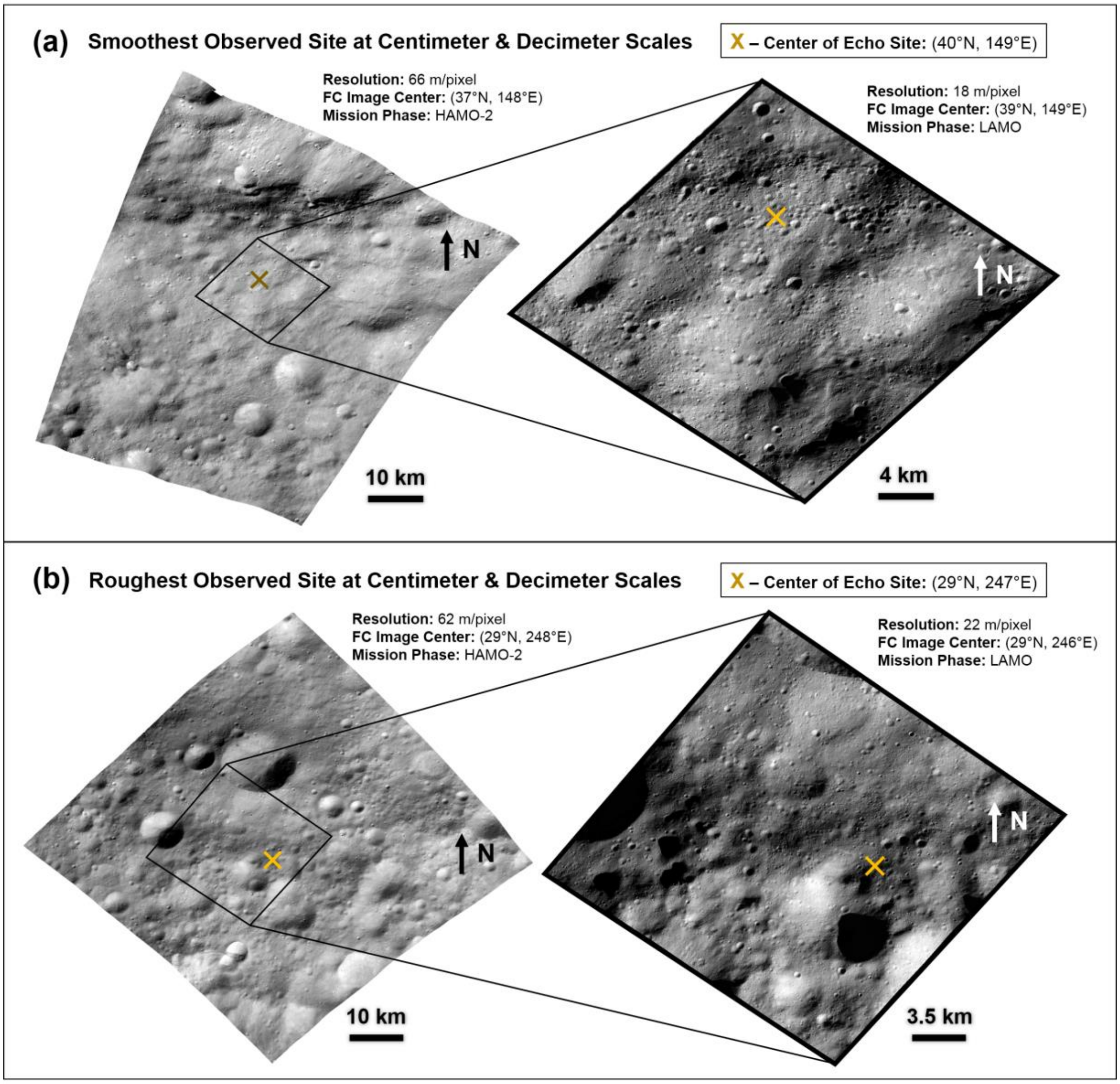

Supplementary Figure 5. High-resolution Dawn framing camera (FC) images of the echo sites with the strongest and weakest radar reflectivity. Roughness appears nearly equal at the resolution of the FC images, whereas radar reflectivity of each site suggests that (a) is much smoother than (b) at centimeter to decimeter scales (below the FC resolution). Images to the left cover the approximate extent of echo sites at ~65-m/pixel resolution acquired during one of Dawn's high-altitude mapping orbits (HAMO or HAMO-2) around Vesta. Images on the right show a subset of echo sites at ~20-m/pixel resolution acquired during Dawn's lowest-altitude mapping orbit (LAMO) of Vesta, where the center of each echo site is marked by an X. Radar-wavelength scale surface roughness on Vesta does not appear to correlate with surface topography at the scale of meters to tens of meters, indicating that cratering alone cannot dictate Vesta's surface texture.

9.1. *Supplementary References*

Krening, S. C., Semenov, B. V. & Acton, C. H. (2012). "DAWN SPICE KERNELS V1.0, DAWN-M/A-SPICE-6-V1.0," NASA Planetary Data System.

Slobin, S. D. (2015). "70-m Subnet Telecommunication." In *DSN Telecommunications Link Design Handbook (810-005),* Module 101, Rev. F. Retrieved from https://deepspace.jpl.nasa.gov/dsndocs/810-005/spacelink.cfm.

Taylor, J. (2009). *Dawn Telecommunications* (DESCANSO Article No. 13), Pasadena, California: NASA Jet Propulsion Laboratory, California Institute of Technology.

Taylor, J., Cheung, K.-M. & Wong, C.-J. (2001a) *Mars Global Surveyor Telecommunications* (DESCANSO Article No. 1).

Taylor, J., Fernández, M. M., Alamanac, A. I. B. & Cheung, K.-M. (2001b). *Deep Space 1 Telecommunications* (DESCANSO Article No. 2), Pasadena, California: NASA Jet Propulsion Laboratory, California Institute of Technology.

Williams, D. A., Jaumann, R., McSween, H. Y., Marchi, S., Schmedemann, N., Raymond, C. A. & Russell, C. T. (2014). "The chronostratigraphy of protoplanet Vesta." *Icarus*, **244**, 158–165. doi:10.1016/j.icarus.2014.06.027

CHAPTER IV

MEASUREMENT REQUREMENTS FOR ORBITAL FORWARD-SCATTER BISTATIC RADAR OBSERVATIONS OF PLANETARY SURFACES

Palmer, E. M. & Heggy, E. (*Under Review*). *IEEE Geoscience and Remote Sensing Letters.*

1. Abstract

Assessing the variability of surface roughness on planetary bodies is crucial for understanding both the physical mechanisms that have governed their surface evolution, and the safety and trafficability of future landing, anchoring and sampling sites. Herein, we present how opportunistic orbital bistatic radar (BSR) methods can be used to achieve the above scientific and technical objectives for key planetary bodies that are currently under investigation by orbital missions. BSR observations conducted at asteroid Vesta and comet 67P/Churyumov-Gerasimenko by the Dawn and Rosetta missions, respectively, demonstrate that it is possible to constrain the surface roughness of small bodies using the spacecraft's high-gain telecommunications antenna (HGA) during entries into and exits from occultation. For several different small-bodies and moons, we present an estimation of the theoretical differential Doppler shift (δf) between the direct signal and surface-scattered signal that is associated with the specific observation geometries of potential opportunistic BSR experiments. Our results suggest that opportunistic BSR observations of small-bodies less than a few hundred kilometers in diameter will require the presence of an onboard ultra-stable oscillator (USO) to be able to quantify surface roughness variability.

2. Introduction

From 2011 to 2012, the Dawn mission conducted the first opportunistic, orbital bistatic radar (BSR) experiment at a small-body, Asteroid Vesta, at grazing incidence using the onboard high-gain radio antenna (HGA) to transmit and the 70-meter Deep Space Network (DSN) antennas on Earth to receive (Palmer, Heggy & Kofman, 2017). By continuously transmitting basic telemetry data while the spacecraft enters and exits occultations behind the target body as seen along the Earth's line of sight, the X-band (8.4 GHz) radio waves transmitted by the HGA scatter from the target's surface just before and immediately after each occultation, resulting in radar reflections from the object's surface at grazing angles of incidence ($\theta_i \approx 89°$, i.e., in the forward-scatter regime of BSR experiments) (Palmer, Heggy & Kofman, 2017). Due to the opportunistic nature of the experiment (i.e., as no specific pointing, slewing of the spacecraft or any electrical or mechanical changes are required during occultations), forward-scatter BSR observations do not conflict with gravity radio science observations and require minimal operational constraints.

By applying radar power spectral analysis to the signal received by the DSN ground station, the power of the surface-reflected signal (hereafter 'the surface echo') can be measured relative to the power received from the direct carrier signal (hereafter 'the direct signal'), and thereby used to assess the relative radar reflectivity of the target body's surface at the site of each surface echo (at grazing incidence). Multiple forward-scatter BSR observations will therefore yield a regional map of relative radar reflectivity across the surface of the target body, where the extent of coverage is dependent on the observation geometry and shape and size of the target body (Palmer, Heggy & Kofman, 2017).

Furthermore, if the surface's dielectric properties are uniform—i.e., for relatively uniform surface density and composition, as is the case for planetary surfaces covered by a well-gardened regolith (Palmer et al., 2015) and for the surfaces of icy moons—any observed variability in the surface's relative radar reflectivity at S- (2.3 GHz) and X-band (8.4 GHz) frequencies can be primarily attributed to differences in surface roughness at the scale of the observing radar wavelength. For X-band observations ($\lambda \approx 4$ cm), characterizing relative surface roughness across the surface of the target body at centimeter-to-decimeter scales is critical for understanding the geophysical processes that shape the surface's texture, as well as for assessing safe surface landing, anchoring and trafficability such as for in-situ and sampling missions (Fong et al., 2008).

However, while orbital BSR experiments have been successfully conducted at Mercury (Butler, Slade & Muhleman, 1993), Venus (Simpson et al., 2009), the Moon (Tyler et al., 1967; Nozette et al., 1996; Patterson et al., 2017), Mars (Fjeldbo, Kliore & Seidel 1972; Simpson & Tyler, 2001) and

Titan (Pérez-Ayúcar, et al., 2006), these are commonly performed at much lower angles of incidence than the forward-scatter regime (i.e., for $\theta_i < 80°$ as opposed to $\theta_i \approx 89°$), and at high orbital spacecraft velocities (e.g., ~3.4 km/s in the case of the Mars Global Surveyor, as opposed to ~200 m/s in the case of the opportunistic BSR experiment by Dawn at Vesta (Palmer, Heggy & Kofman, 2017)).

For small planetary bodies, such as asteroids and comets, the differential Doppler shift δf between the received direct signal and the surface echo signal is therefore very small—$\delta f \approx 10$ Hz for Dawn at Vesta (Palmer, Heggy & Kofman, 2017), and $\delta f < 1$ Hz for Rosetta at comet 67P/CG (Pätzold et al., 2007)—in contrast to $\delta f \approx 10$ kHz for the Mars Global Surveyor (MGS) BSR experiment (Simpson & Tyler, 2001). As a result, the ability to distinguish the direct signal from the surface-reflected (and hence Doppler-shifted surface echo signal) in the received power-frequency spectrum for a given forward-scatter BSR experiment depends on the frequency stability of the transmitted radio signal from the spacecraft (Palmer, Heggy & Kofman, 2017). In turn, the ability to assess a target body's relative surface roughness is dependent on the ability to distinguish the frequency-broadened, Doppler-shifted surface echo from the direct signal.

Herein, we assess the feasibility of conducting opportunistic forward-scatter BSR experiments for several planetary missions by (1) calculating the theoretical δf between the direct signal and surface echo for a given acquisition geometry, and (2) setting a limit on the frequency stability of the spacecraft transmitter.

3. Method

In two-way coherent mode, the frequency of the spacecraft transmitter is driven by the uplink signal with high accuracy (e.g., Asmar et al., 2005). However, during forward-scatter BSR experiments, the spacecraft passes into occultation behind the target body for a few seconds to tens of minutes before re-emerging. As a consequence, only the one-way non-coherent downlink mode is possible during the moments preceding and following occultation, and the frequency stability of the HGA transmitter is therefore dependent on the stability of the onboard internal frequency source (Thornton & Border, 2003; Palmer, Heggy & Kofman, 2017). Our analysis provides the measurement requirement on the frequency stability for the spacecraft's onboard oscillator.

3.1. *Calculating the Differential Doppler Shift*

We calculate theoretical δf for a given planetary body by applying the same approach as used at Asteroid Vesta for the Dawn mission detailed by Palmer, Heggy & Kofman (2017) (further detailed by Simpson (1993)) and under the following assumptions: in the case of opportunistic orbital bistatic radar experiments, (1) all spacecraft orbits are nominally designed to be face-on with respect to Earth, as this minimizes periods of occultation of the spacecraft behind the target body, which entail temporary loss of communication; (2) a reasonable occultation duration of t_{occ} is no more than ~10 minutes (corresponding to average occultation durations of Dawn behind Vesta); and (3) the spacecraft's HGA beamwidth $\theta_{bw} \leq 2°$, such that the surface-scattered echo signal occurs at grazing incidence.

The differential Doppler shift (i.e., frequency separation between the direct signal and surface echo) is given by:

$$|\delta f| = |\Delta f_{\text{echo}} - \Delta f_{\text{direct}}| \tag{1}$$

where
$$\Delta f_{\text{direct}} = \frac{1}{2\pi} \vec{k}_{\text{direct}} \cdot \vec{v}_{\text{direct}} \tag{2a}$$

and
$$\Delta f_{\text{echo}} = \frac{1}{2\pi} \left(\vec{k}_1 \cdot \vec{v}_1 - \vec{k}_2 \cdot \vec{v}_2 \right) \tag{2b}$$

for which $\vec{k}$ is the wave propagation vector of magnitude $2\pi/\lambda_0$; λ_0 is the transmitted wavelength; and $\vec{v}$ is the relative velocity between two objects. The specific acquisition geometry for opportunistic forward-scatter bistatic radar is illustrated in Fig. 1.

Using the geometry defined in Fig. 1, δf reduces to:

$$|\delta f| = \frac{1}{\lambda_0} \left[\left| \left(\hat{k}_{\text{direct}} - \hat{k}_1 \right) \cdot \vec{v}_{\text{SC}|\text{orbit}} \right| + \left| \left(\hat{k}_1 - \hat{k}_2 \right) \cdot \vec{v}_{\text{surf}|\text{rot}} \right| + \left| \left(\hat{k}_{\text{direct}} - \hat{k}_2 \right) \cdot \vec{v}_{\text{body}} \right| \right] \tag{3}$$

where $\left(\hat{k}_{\text{direct}} - \hat{k}_2 \right) \approx 0$ since $\vec{k}_{\text{direct}}$ and $\vec{k}_2$ are nearly parallel at such large distances from Earth.

Equation 3 is then expressed in terms of the angles defined in Fig. 1 as:

$$|\delta f| = \frac{1}{\lambda_0} \left[v_{\text{SC}|\text{orbit}} \sin\left(\theta_{\text{SC}|\text{orbit}|\text{phase}} \right) \left| \sin\left(\theta_{\text{tilt}} \right) - \sin\left(\theta_{\text{tilt}} + \tfrac{1}{2}\theta_{\text{bw}} \right) \right| + v_{\text{surf}|\text{rot}} \left| \cos\left(180° + \tfrac{1}{2}\theta_{\text{bw}} \right) + 1 \right| \right] \tag{4}$$

where $\sin(\theta_{\text{SC}|\text{orbit}|\text{phase}})$ yields the projection of the spacecraft's orbital velocity onto the bistatic plane; and θ_{tilt} characterizes the viewing geometry of the spacecraft's orbital plane with respect to Earth (0° is face-on yielding no occultations, and 90° is edge-on yielding the maximum

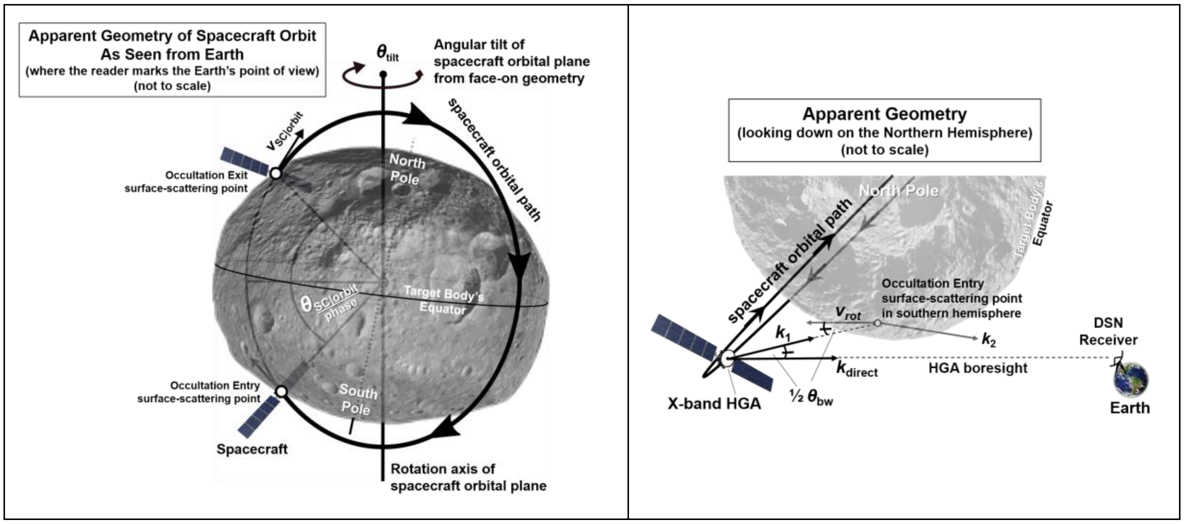

Figure 1. Acquisition geometry (not to scale) of an opportunistic orbital forward-scatter BSR experiment. The spacecraft HGA transmits a signal with a beamwidth of θ_{bw} toward the Deep Space Network receiver on Earth along the wave propagation vector $\vec{k}_{direct}$. Part of the transmitted signal also scatters from the surface of the target body (rotating with velocity $\vec{v}_{rot}$) and propagates along $\vec{k}_1$ and $\vec{k}_2$ undergoing a differential Doppler shift of δf compared to the direct signal. In this example, the surface-scattering point is in the southern hemisphere. The SC's orbital plane is rotated by θ_{tilt} around its polar axis (0° is face-on from Earth's view), resulting in an occultation. The projection of the SC's velocity $\vec{v}_{SC|orbit}$ onto the bistatic plane is non-zero for 0° < $\theta_{SC|orbit|phase}$ < 180°.

possible occultation duration). For a narrow beamwidth of ≤2°, which is associated with spacecraft communications transmissions by X-band (~8.4 GHz) HGAs, $\left(\cos\left(180° + \tfrac{1}{2}\theta_{bw}\right) + 1\right) \approx 10^{-5}$, which is at least three orders of magnitude smaller than $v_{surf|rot}$ of any planetary body, such that Equation 4 becomes:

$$\left|\delta f\right| \approx \frac{1}{\lambda_0} v_{SC|orbit} \sin\left(\theta_{SC|orbit|phase}\right) \left| \sin\left(\theta_{tilt}\right) - \sin\left(\theta_{tilt} + \tfrac{1}{2}\theta_{bw}\right) \right| \tag{5}$$

where
$$\theta_{SC|orbit|phase} = \frac{v_{SC|orbit} t_{occ}}{2(R_{body} + h_{SC})} \tag{6a}$$

and
$$\theta_{tilt} = \cos^{-1}\left[\left(R_{body} - \left(v_{SC|orbit} t_{occ}\right)\frac{1}{2\pi}\right) \Big/ \left(R_{body} + h_{SC}\right)\right] \tag{6b}$$

for which t_{occ} is the duration of complete occultation (the time when the spacecraft is fully obscured by the target body), R_{body} is the maximum radius of the target body, and h_{sc} is the altitude over the target body. The tilt of the spacecraft's orbital plane θ_{tilt} is dependent on the duration of occultation t_{occ} because the maximum possible t_{occ} (e.g., > 30 minutes) will occur when the spacecraft appears to be in an edge-on orbital tilt (θ_{tilt} = 90°) from Earth's viewing geometry, while the minimum possible θ_{tilt} to induce an occultation corresponds to $t_{occ} \gtrsim 0$, such that the apparent angular width of the spacecraft's orbital plane (as seen from Earth's viewing geometry) is equivalent to the apparent angular width of the target body. The orbital phase of the spacecraft $\theta_{SC|orbit|phase}$ can also be determined from t_{occ}, since $t_{occ} \approx 0$ implies that the spacecraft is located at its furthest point from Earth (defined by $\theta_{SC|orbit|phase}$ = 0°) during the moment of spacecraft entry and exit into and from occultation, at which point the spacecraft has no component of velocity along its line-of-sight with Earth. In contrast, when $t_{occ} > 0$, the entry and exit points of the spacecraft into or from occultation will occur when the spacecraft is at some phase $\theta_{SC|orbit|phase}$ along its orbit such that $v_{SC|orbit}$ is non-zero.

Note that if the beamwidth were larger, as potentially the case for S-band (2.3 GHz) transmissions, such that the $v_{surf|rot}$ term remained, it would further increase the calculated differential Doppler shift due to a greater angular separation between the spacecraft and the surface-scattering point during a partial occultation of the HGA beam. However, X-band frequency communications (and higher frequencies, such as 26 GHz at Ka-band) are preferentially used for data downlink operations due to their higher data transmission rate capabilities and higher signal-to-noise ratios (e.g., Simons et al., 2011).

Hence, according to Equation 5, the differential Doppler shift of an opportunistic forward-scatter BSR experiment at X-band frequency (and higher) is primarily dependent on the spacecraft's velocity and the orientation of its orbital plane from Earth's view—where the latter is related to the duration of occultation and the radius of the target body. Table 1 provides the range and applicability of each of the parameters constituting Equations 5, 6a and 6b.

3.2. Calculating the Required Frequency Stability of the Onboard Oscillator

The frequency stability of an oscillator is often reported in terms of its frequency drift rate with respect to the direct carrier frequency ($\Delta f_{drift}/f_0$) over a specified integration time (τ), which corresponds to the one-way Allan deviation in the case of downlink forward-scatter BSR experiments (e.g., Thornton & Border, 2003; Asmar et al., 2005). For a theoretical

Table 1. Parameters and boundary conditions used to calculate δf for opportunistic, forward-scatter bistatic radar experiments.

Parameter	Units	Range of Validity	Definition	Examples: OSIRIS-REx at Asteroid Bennu	Dawn at Asteroid Vesta	MAVEN at Mars
R_{body}	m	$\geq 10^2$	Target body radius	282.5	286,300	3,396,000
h_{SC}	m	$\leq 10^5$	S/C altitude	1000	210,000	125,000
$v_{\text{SC}\mid\text{orbit}}$	m/s	$\geq 10^{-2}$	S/C orbital speed	0.07	200	3,500
$v_{\text{surf}\mid\text{rot}}$	m/s	$< 10^4$	Equatorial rotational velocity of the target body	0.11	93	240
t_{occ}	seconds	60–1800 (i.e., 1-30 min.)	Allowable duration of full occultation (no communication with S/C)	600	600	600
θ_{bw}	degrees	$\leq 2°$	X-band HGA beamwidth (at FWHM)	~1.6°	~1.6°	~1.6°
$\theta_{\text{SC}\mid\text{orbit}\mid\text{phase}}$	degrees	$0° < \lvert\theta\rvert < 90°$	Phase of S/C along polar orbit • $\lvert\theta\rvert = 0°$ *or* 180°: Zero LOS component of S/C orbital velocity from Earth's POV • $\lvert\theta\rvert = \pm 90°$: Maximum LOS component of S/C orbital velocity from Earth's POV	0.91°	6.9°	17°
θ_{tilt}	degrees	0°–90°	Tilt of S/C's polar orbital plane from Earth's POV • $\theta = 90°$: Edge-on orbital plane; longest possible t_{occ}	77.6°	57.4°	29.6°
$\lvert\delta f\rvert$	Hz	0.1–1000	Calculated differential Doppler shift	8.9×10^{-5}	5.0	350

*S/C ≡ spacecraft; HGA ≡ high-gain antenna; FWHM ≡ full-width at half-max; LOS ≡ line-of-sight; POV ≡ point of view

differential Doppler shift δf, and a transmitted direct signal frequency f_0, the frequency drift Δf_{drift} should be much less than δf over the time of integration τ—which in turn must be sufficiently long to increase the frequency resolution f_{res} of the resulting power-frequency spectrum, but sufficiently short so that the onboard oscillator's frequency drift Δf_{drift} does not cause the direct signal to broaden in the frequency spectrum such that it overlaps the Doppler-shifted surface echo signal in the frequency domain. Fig. 2 shows an example of frequency-broadening of the direct signal associated with power spectral analysis of Dawn BSR observations of Asteroid Vesta, and subsequent, partial overlap of the direct signal with the surface echo signal.

It should also be noted that at grazing angles of incidence of ~89° as is the case for opportunistic BSR experiments, the handedness of circularly polarized radio waves is conserved even after reflection from the target body's surface (Palmer, Heggy & Kofman, 2017). For example, as shown in Fig. 2, the LCP component of the surface echo from the Dawn BSR experiment at Vesta is below the noise level and therefore at least 15 dB below the RCP component, which is consistent with the calculation of Fresnel power reflectance that suggests $\gtrsim$90% of the power incident on the surface of Vesta will be reflected with the same sense of circular polarization as that of the incident wave (RCP) (Palmer, Heggy & Kofman, 2017).

Hence, the accurate identification of the surface echo signal does not rely on the presence of an opposite-sense circularly polarized component within the power received at the ground station. Instead, the surface echo is characterized by a secondary peak in the same-sense circularly polarized power-frequency spectrum of the received signal that is Doppler-shifted by δf with respect to the primary peak (the direct signal) as shown in Fig. 2b and 2d.

Herein, we report on the maximum allowable Δf_{drift} for various active and planned missions, where forward-scatter BSR experiments require at least $\Delta f_{\text{drift}} \lesssim \frac{1}{2}|\delta f|$ over a given τ, which we conservatively set to 1 s (for comparison, τ = 2.5 s was used to process the Dawn BSR data at Vesta (Palmer, Heggy & Kofman, 2017)).

4. Results: Minimum Requirements for Spacecraft Onboard Oscillators

The theoretical differential Doppler shift δf is calculated for potential opportunistic BSR observations of 10 different target bodies (including asteroids, moons and one planet) by 11 different current and planned space missions. The δf calculated for each mission sets an upper limit on the allowable frequency drift Δf_{drift} of the spacecraft's internal oscillator. We have assumed that all observations occur at X-band (~8.4 GHz) radar frequencies using high-gain antennas with a beamwidth ≤2°, and that the maximum duration of occultation of the spacecraft by the target body is t_{occ} = 10 minutes. Using a higher transmission frequency or shortening the occultation time will

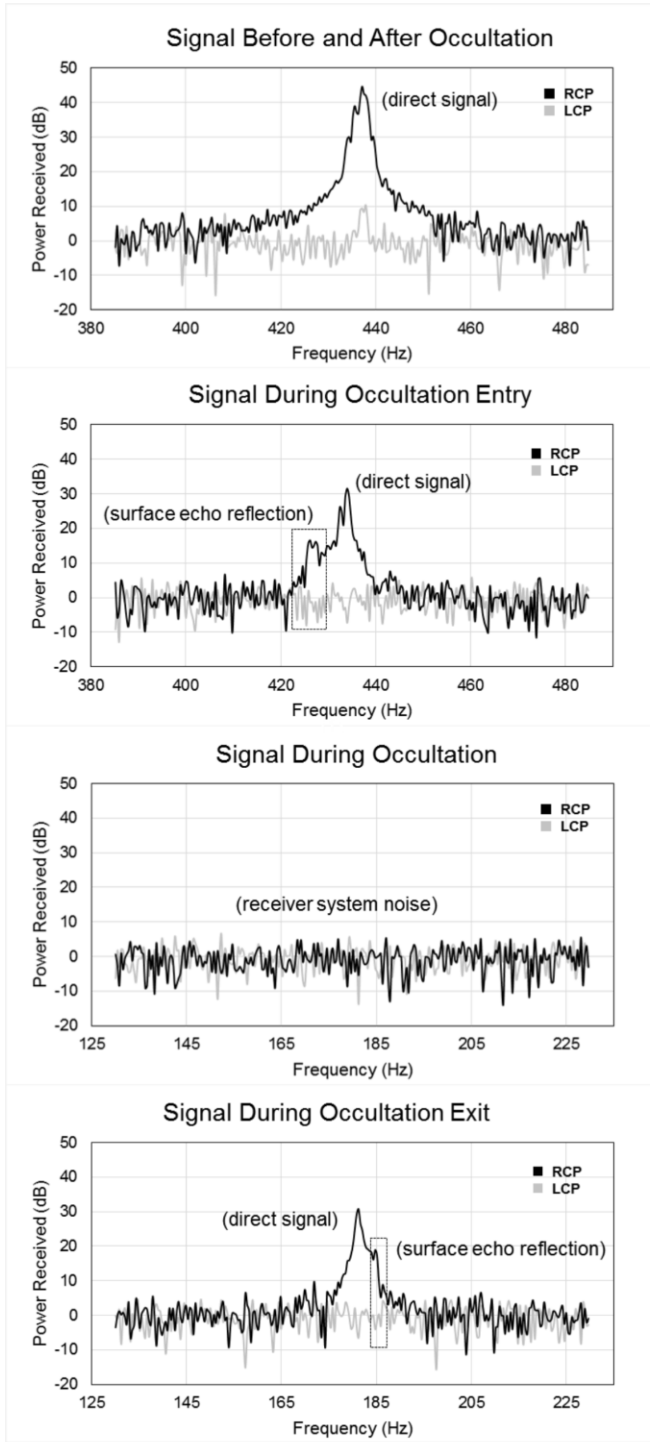

Figure 2. BSR downlink received by ground stations on 29 Feb 2012 from Dawn at Vesta: (a) before, (b) during entry into, (c) during, and (d) during exit from an occultation of Dawn behind Vesta from the receiver's point of view. Surface echo reflections exhibit a small δf relative to the direct signal, and are partially overlapped by the latter

both decrease δf, leading to more stringent requirements on the frequency drift of the internal oscillator.

Our results, summarized in Table 2 and plotted in Fig. 3, suggest that solar system objects with a radius on the order of $R_{body} \lesssim 10^4$–10^5 m require an orbiting spacecraft to have an onboard ultra-stable oscillator (USO) in order to provide sufficient frequency stability over an integration time τ of ~1 s to yield a power-frequency spectral resolution f_{res} better than ½ | δf |.

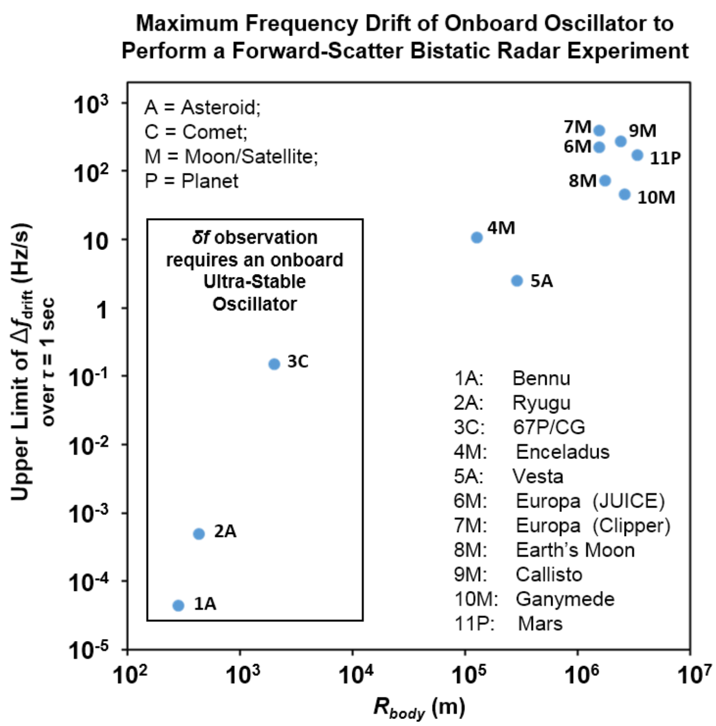

Figure 3. Upper limits on the frequency drift of spacecraft's internal oscillators in order to perform a forward-scatter BSR experiment at different planetary bodies.

In the case of the Dawn BSR experiment conducted at Asteroid Vesta, Palmer, Heggy & Kofman (2017) observed that $\delta f \lesssim 20$ Hz and as small as 2 Hz, and therefore selected f_{res} to be <1 Hz—specifically, $f_{res} = 0.4$ Hz, corresponding to $\tau = 2.5$ s. Hence, to distinguish the direct signal from the surface echo, Dawn's onboard one-way downlink frequency source needed Δf_{drift} less than a few Hz at $\tau = 2.5$ s. Fortunately, Dawn's internal auxiliary oscillator exhibited a one-way $\Delta f_{drift} \approx 0.05$ Hz at $\tau = 1$ s (Chen et al., 2000; fig. 6 therein), resulting in $\Delta f_{drift} \approx 0.1$ Hz at $\tau = 2.5$ s.

For solar system bodies with equatorial radii $R_{eq} \lesssim 10^4$–10^5 m however—which characterize the majority of asteroids and comets—onboard oscillator frequency drift requirements are more stringent and require the presence of an ultra-stable oscillator (USO) onboard the spacecraft to perform a forward-scatter BSR experiment (e.g., as used for Rosetta's S- and X-band BSR experiment at comet 67P/CG (Pätzold et al., 2007)). USOs provide a high-accuracy internal frequency reference for one-way spacecraft transmissions and minimize frequency broadening associated with frequency drift when integrating the received signal over longer periods of time τ that maximize the frequency resolution f_{res} of the observed power-frequency spectra.

Our analysis does not consider high-altitude flyby mission observations of moons and small bodies with $R_{eq} \lesssim 10^4$ m, such as the martian moons Phobos ($R_{eq} \approx 11$ km) or Deimos ($R_{eq} \approx 6$ km). The ongoing Mars Express (MEX) mission has conducted flybys of Phobos typically ≥1,000 km from the surface, with only 6 flybys at close-approach distances of 50-150 km (Witasse et al., 2014). Flyby observations of Deimos, by contrast, have been conducted no closer than 10,000 km (Witasse et al., 2015). At such distances and due to infrequent close-approach maneuvers, opportunistic occultations are rare due to the small size of the target bodies and the observing geometry.

Table 2. Maximum differential Doppler shift and minimum measurement requirements to perform a forward-scatter BSR experiment at different planetary bodies.

Mission	Target Body	R_{body} (m)	$v_{SC\|orbit}$ (m/s)	δf (Hz)	Max. Δf_{drift} (Hz/s) (at τ = 1 s)	Mission Ref.
OSIRIS-REx	Bennu (A)	2.82×10^2	0.07	9×10^{-5}	4×10^{-5}	(Lauretta et al., 2017)
Hayabusa2	Ryugu (A)	4.26×10^2	0.15	1×10^{-3}	5×10^{-4}	(Bellarose & Yano, 2010)
Rosetta	67P/CG (C)	2×10^3	1.88	0.3	1.5×10^{-1}	(Pätzold et al., 2007; Andert et al., 2017)
THEO (*)	Enceladus (M)	1.26×10^5	206	20	10	(MacKenzie et al., 2016)
Dawn	Vesta (A)	2.86×10^5	200	5	2.5	(Palmer, Heggy & Kofman, 2017)
JUICE	Europa (M)	1.561×10^6	3600	460	2×10^2	(JUICE Science Working Team, 2014)
Europa Clipper	Europa (M)	1.561×10^6	4000	800	4×10^2	(Park et al., 2015)
LRO	The Moon (M)	1.738×10^6	1600	150	70	(Mazarico et al., 2017)
JUICE	Callisto (M)	2.411×10^6	4000	540	3×10^2	(JUICE Science Working Team, 2014)
JUICE	Ganymede (M)	2.631×10^6	1600	92	50	(JUICE Science Working Team, 2014)
MAVEN	Mars (P)	3.396×10^6	3500	350	2×10^2	(Jakosky et al., 2015)

(*) Mission concept; (A) Asteroid; (C) Comet; (M) Moon; and (P) Planet

5. Application to Current & Future Missions to Moons, Asteroids and Comets

As several future missions to asteroids, comets and icy moons are considering landing, anchoring and sampling opportunities (e.g., Lauretta et al., 2017; Brown, Cantillo & Porter, 2017; Elvis, 2012), S- and X-band frequency forward-scatter BSR observations can provide valuable information on surface roughness conditions at centimeter-to-decimeter scales for these bodies.

Assessing surface roughness for planetary surfaces is a key element in understanding their geological and geophysical evolution. For instance, airless bodies like the Moon have rough surfaces shaped by impacts and lava flows that result in a narrow range of surface roughnesses associated with these phenomena (Campbell et al., 2010). By contrast, bodies with more complex atmospheres (e.g., global dust storms on Mars) and/or with abundant volatile occurrence (e.g., ground-ice, ice deposits, fluvial flows) will exhibit a broader range of surface textures as a result of aeolian deposition and erosion, as well as potential surface melts and flows that tend to smooth surfaces at the scale of S- and X-band radar observations (e.g., Campbell et al., 2010). As BSR is able to constrain the ambiguities associated with surface roughness variability, it can hence be used to assess whether the body under investigation exhibits a wide range of surface roughnesses (therefore implying the occurrence of active geophysical processes generating its surface texture) or a narrow range of surface roughnesses (such as the gently undulating slopes of 2-8° observed on the Moon at centimeter-to-decimeter scales (Thompson, Ustinov & Heggy, 2011), from which we can deduce that the surface texture is shaped by fewer mechanisms, typically impact-related).

Furthermore, surface roughness enables the assessment of the safest sites for landing and potential surface trafficability (Fong et al., 2008; Palmer, Heggy & Kofman, 2017). Hence, quantifying surface textural properties is fundamental to understanding the primary geophysical processes and physical conditions that have shaped the surface, particularly when compared with geomorphological and compositional studies that use high-resolution orbital optical and hyperspectral observations (e.g., Palmer, Heggy & Kofman, 2017).

Fig. 3 suggests that for most small-bodies (asteroids and comets), an onboard USO will be required for sufficient frequency stability to conduct successful opportunistic forward-scatter BSR observations. Our results also suggest that larger planetary bodies will yield sufficiently large δf that do not impose strong accuracy requirements on the frequency stability of the spacecraft's onboard oscillator. However, our analysis does not account for the weaker SNR of surface reflections that are associated with greater distances of the target body to the Earth (e.g., Europa, Callisto, Ganymede and Enceladus). Our analysis also does not incorporate potential signal distortion associated with different types of plasma environments along the line-of-sight (LOS). Weaker SNR signals will require longer averaging times of the received power-frequency spectra, and therefore better frequency stability of the spacecraft's onboard oscillator so as to minimize Doppler broadening. Future BSR feasibility studies for comets and icy moons will therefore need to account for the above factors, in addition to the measurement requirements summarized in Fig. 3. Increasing the required frequency stability of the onboard oscillator for future planetary missions—e.g., with a frequency drift of <0.001 Hz over an integration time τ of ~1 s—will enable more accurate opportunistic forward-scatter BSR experiments to be conducted at several planetary bodies.

6. Conclusions

Understanding the magnitude and spatial distribution of surface roughness on planetary bodies provides unique insight into the physical mechanisms that govern the evolution of their surfaces. Opportunistic BSR, achieved during entries and exits from occultations by a spacecraft, is a powerful technique capable of providing observations in support of this objective. Our results suggest that orbital BSR conducted at small-bodies $\lesssim$100 km in diameter require the use of an onboard USO while planetary bodies $\gtrsim$500 km do not.

7. Acknowledgements

The authors would like to acknowledge Tommy Thompson and several members of the Radio Tracking Division from the Jet Propulsion Laboratory, as well as Richard Simpson from Stanford University for helpful discussions.

8. References

Andert, T., Remus, S., Simpson, R. A., Paetzold, M., Häusler, B., Tellmann, S., González Peytavi, G. & Bird, M. K. (2017). "Bistatic Radar Observations of 67P/Churyumov-Gerasimenko." *American Geophysical Union Fall Meeting*, Abstract #P12A-01.

Asmar, S. W., Armstrong, J. W., Iess, L. & Tortora, P. (2005). "Spacecraft Doppler tracking: Noise budget and accuracy achievable in precision radio science observations." *Radio Sci.*, **40**(2), 1–9. doi:10.1029/2004RS003101

Bellerose, J. & Yano, H. (2010). "Dynamics of Asteroid 1999 JU3: Target of the Hayabusa Follow-on Mission." *T. JSASS Aerosp. Tech. Jpn.*, **8**(ists27), Tk_23-Tk_28. doi:10.2322/tastj.8.Tk_23

Brown, D. C., Cantillo, L. L. & Porter, M. A. (21 Dec 2017). "NASA Invests in Concept Development for Missions to Comet, Saturn Moon Titan" [Press Release].

Butler, B. J., Muhleman, D. O. & Slade, M. A. (1993). "Mercury: full-disk radar images and the detection and stability of ice at the North Pole." *J. Geophys. Res.*, **98**(E8), 15003. doi:10.1029/93JE01581

Campbell, B. A. (2002). *Radar Remote Sensing of Planetary Surfaces*, Cambridge University Press.

Campbell, B. A., Carter, L. M., Campbell, D. B., Nolan, M., Chandler, J., Ghent, R. R., Ray Hawke, B., Anderson, R. F. & Wells, K. (2010). "Earth-based 12.6-cm wavelength radar mapping of the Moon: New views of impact melt distribution and mare physical properties." *Icarus*, **208**(2), 565–573. doi:10.1016/j.icarus.2010.03.011

Chen, C.-C., Makovsky, A., Shambayati, S., Taylor, F. H., Herman, M. I., Zingales, S. H., Siemsen, K. & Nuckolls, C. (2000). *Small Deep Space Transponder (SDST) DS1 Technology Validation Report* (JPL Publication 00-10 No. 11), Pasadena, California: Jet Propulsion Laboratory, California Institute of Technology.

Elvis, M. (2012). "Let's mine asteroids — for science and profit." *Nature News*, **485**(7400), 549. doi:10.1038/485549a

Fjeldbo, G., Kliore, A. & Seidel, B. (1972). "Bistatic radar measurements of the surface of Mars with Mariner 1969." *Icarus*, **16**(3), 502–508. doi:10.1016/0019-1035(72)90096-6

Fong, T., Deans, M., Smith, T., Lee, P., Heldmann, J., Pacis, E., Schreckenghost, D., Landis, R., Osborn, J., Kring, D., Heggy, E., Mishkin, A., Snook, K. & Stoker, C. (2008). "A Preliminary Examination of Science Backroom Roles and Activities for Robotic Lunar Surface Science." *NLSI Lunar Science Conference*, Abstract #2141.

Jakosky, B. M., Grebowsky, J. M., Luhmann, J. G. & Brain, D. A. (2015). "Initial results from the MAVEN mission to Mars." *Geophys. Res. Lett.*, **42**(21), 8791–8802. doi:10.1002/2015GL065271

JUICE Science Working Team. (2014). *JUICE JUpiter ICy moons Explorer: Exploring the emergence of habitable worlds around gas giants* (Definition Study Report), European Space Agency, Science and Robotic Exploration.

Lauretta, D. S., Balram-Knutson, S. S., Beshore, E., Boynton, W. V., Drouet d'Aubigny, C., DellaGiustina, D. N., Enos, H. L., Golish, D. R., Hergenrother, C. W., Howell, E. S., Bennett, C. A., Morton, E. T., Nolan, M. C., Rizk, B., Roper, H. L., Bartels, A. E., Bos, B. J., Dworkin, J. P., Highsmith, D. E., Lorenz, D. A., Lim, L. F., Mink, R., Moreau, M. C., Nuth, J. A., Reuter, D. C., Simon, A. A., Bierhaus, E. B., Bryan, B. H., Ballouz, R., Barnouin, O. S., Binzel, R. P., Bottke, W. F., Hamilton, V. E., Walsh, K. J., Chesley, S. R., Christensen, P. R., Clark, B. E., Connolly, H. C., Crombie, M. K., Daly, M. G., Emery, J. P., McCoy, T. J., McMahon, J. W., Scheeres, D. J., Messenger, S., Nakamura-Messenger, K., Righter, K. & Sandford, S. A. (2017). "OSIRIS-REx: Sample Return from Asteroid (101955) Bennu." *Space Sci Rev*, **212**(1), 925–984. doi:10.1007/s11214-017-0405-1

MacKenzie, S. M., Caswell, T. E., Phillips-Lander, C. M., Stavros, E. N., Hofgartner, J. D., Sun, V. Z., Powell, K. E., Steuer, C. J., O'Rourke, J. G., Dhaliwal, J. K., Leung, C. W. S., Petro, E. M., Wynne, J. J., Phan, S., Crismani, M., Krishnamurthy, A., John, K. K., DeBruin, K., Budney, C. J. & Mitchell, K. L. (2016). "THEO concept mission: Testing the Habitability of Enceladus's Ocean." *Adv. Space Res.*, **58**(6), 1117–1137. doi:10.1016/j.asr.2016.05.037

Mazarico, E., Neumann, G. A., Barker, M. K., Goossens, S., Smith, D. E. & Zuber, M. T. (2017). "Orbit determination of the Lunar Reconnaissance Orbiter: Status after seven years." *Planet. Space Sci.* doi:10.1016/j.pss.2017.10.004

Nozette, S., Lichtenberg, C. L., Spudis, P., Bonner, R., Ort, W., Malaret, E., Robinson, M. & Shoemaker, E. M. (1996). "The Clementine Bistatic Radar Experiment." *Science*, **274**(5292), 1495–1498. doi:10.1126/science.274.5292.1495

Palmer, E. M., Heggy, E., Capria, M. T. & Tosi, F. (2015). "Dielectric properties of Asteroid Vesta's surface as constrained by Dawn VIR observations." *Icarus*, **262**, 93–101. doi:10.1016/j.icarus.2015.08.031

Palmer, E. M., Heggy, E. & Kofman, W. (2017). "Orbital bistatic radar observations of asteroid Vesta by the Dawn mission." *Nat. Commun.*, **8**(409). doi:10.1038/s41467-017-00434-6

Park, R. S., Bills, B., Buffington, B. B., Folkner, W. M., Konopliv, A. S., Martin-Mur, T. J., Mastrodemos, N., McElrath, T. P., Riedel, J. E. & Watkins, M. M. (2015). "Improved detection of tides at Europa with radiometric and optical tracking during flybys." *Planet. Space Sci.*, **112**, 10–14. doi:10.1016/j.pss.2015.04.005

Patterson, G. W., Stickle, A. M., Turner, F. S., Jensen, J. R., Bussey, D. B. J., Spudis, P., Espiritu, R. C., Schulze, R. C., Yocky, D. A., Wahl, D. E., Zimmerman, M., Cahill, J. T. S., Nolan, M., Carter, L., Neish, C. D., Raney, R. K., Thomson, B. J., Kirk, R., Thompson, T. W., Tise, B. L., Erteza, I. A. & Jakowatz, C. V. (2017). "Bistatic radar observations of the Moon using Mini-RF on LRO and the Arecibo Observatory." *Icarus*, **283**, 2–19. doi:10.1016/j.icarus.2016.05.017

Pätzold, M., Häusler, B., Aksnes, K., Anderson, J. D., Asmar, S. W., Barriot, J.-P., Bird, M. K., Boehnhardt, H., Eidel, W., Grün, E., Ip, W. H., Marouf, E., Morley, T., Neubauer, F. M., Rickman, H., Thomas, N., Tsurutani, B. T., Wallis, M. K., Wickramasinghe, N. C., Mysen, E., Olson, O., Remus, S., Tellmann, S., Andert, T., Carone, L., Fels, M., Stanzel, C., Audenrieth-Kersten, I., Gahr, A., Müller, A.-L., Stupar, D. & Walter, C. (2007). "Rosetta Radio Science Investigations (RSI)." *Space Sci. Rev.*, **128**(1–4), 599–627. doi:10.1007/s11214-006-9117-7

Pérez-Ayúcar, M., Lorenz, R. D., Floury, N., Prieto-Cerdeira, R. & Lebreton, J.-P. (2006). "Bistatic observations of Titan's surface with the Huygens probe radio signal." *J. Geophys. Res. Planet.*, **111**(E7). doi:10.1029/2005JE002613

Simons, R. N., Wintucky, E. G., Landon, D. G., Sun, J. Y., Winn, J. S., Laraway, S., McIntire, W. K., Metz, J. L. & Smith, F. J. (2011). "Demonstration of multi-Gbps data rates at Ka-band using software-defined modem and broadband high power amplifier for space communications." In *2011 IEEE MTT-S International Microwave Symposium*, Baltimore, MD, USA: IEEE, pp. 1–4. doi:10.1109/MWSYM.2011.5972636

Simpson, R. (2001). "Mars Global Surveyor Bistatic Radar Probing of the MPL/DS2 Target Area." *Icarus*, **152**(1), 70–74. doi:10.1006/icar.2001.6629

Simpson, R. A. (1993). "Spacecraft studies of planetary surfaces using bistatic radar." *IEEE. T. Geosci. Remote*, **31**(2), 465–482. doi:10.1109/36.214923

Simpson, R. A., Tyler, G. L., Häusler, B., Mattei, R. & Pätzold, M. (2009). "Venus Express bistatic radar: High-elevation anomalous reflectivity." *J. Geophys. Res.*, **114**. doi:10.1029/2008JE003156

Thompson, T. W., Ustinov, E. A. & Heggy, E. (2011). "Modeling radar scattering from icy lunar regoliths at 13 cm and 4 cm wavelengths." *J. Geophys. Res.*, **116**(E1). doi:10.1029/2009JE003368

Thornton, C. L. & Border, J. S. (2003). *Radiometric Tracking Techniques for Deep-Space Navigation*, DESCANSO Series Vol. 1, Hoboken, NJ: John Wiley & Sons, Inc. doi:10.1002/0471728454

Tyler, G. L., Eshleman, V. R., Fjeldbo, G., Howard, H. T. & Peterson, A. M. (1967). "Bistatic-Radar Detection of Lunar Scattering Centers with Lunar Orbiter I." *Science*, **157**(3785), 193–195. doi:10.1126/science.157.3785.193

Witasse, O., Duxbury, T., Chicarro, A., Altobelli, N., Andert, T., Aronica, A., Barabash, S., Bertaux, J.-L., Bibring, J.-P., Cardesin-Moinelo, A., Cichetti, A., Companys, V., Dehant, V., Denis, M., Formisano, V., Futaana, Y., Giuranna, M., Gondet, B., Heather, D., Hoffmann, H., Holmström, M., Manaud, N., Martin, P., Matz, K.-D., Montmessin, F., Morley, T., Mueller, M., Neukum, G., Oberst, J., Orosei, R., Pätzold, M., Picardi, G., Pischel, R., Plaut, J. J., Reberac, A., Pardo Voss, P., Roatsch, T., Rosenblatt, P., Remus, S., Schmedemann, N., Willner, K. & Zegers, T. (2014). "Mars Express investigations of Phobos and Deimos." *Planet. Space Sci.*, **102**, 18–34. doi:10.1016/j.pss.2013.08.002

CHAPTER V

CONCLUSIONS

Through the projects described in the above chapters, the first dielectric model of an asteroid's surface has been constructed (Palmer et al., 2015); the first orbital bistatic radar observations of a small-body have been analyzed and interpreted in terms of the asteroid's surface texture at centimeter-to-decimeter scales (Palmer, Heggy & Kofman, 2017); and the feasibility of conducting the same experiment at other small-bodies by ongoing and planned missions has been assessed (Palmer & Heggy, *Under Review*). Following is a summary of the major conclusions and implications from each of these studies in terms of understanding potential volatile occurrence (past or present) on airless, desiccated bodies, particularly through the use of orbital and Earth-based radar remote sensing observations.

1. Dielectric Variability of Asteroid Vesta's Surface

We have established the first surface dielectric model of Asteroid Vesta by using lunar basaltic soil samples as analogs to the dielectric properties of the Vestan basaltic regolith, and by adjusting for the different temperatures, densities and mineralogical variations that are observed by Dawn's Visible and InfraRed (VIR) mapping spectrometer. We find that the dielectric constant ε' of Vesta's desiccated surface at S- and X-band radar frequencies (2.3 GHz and 8.4 GHz, respectively) is ~2.4 and is constant across the surface. Given that the surface is not thermally stable for surficial ice occurrence, any spatial variations observed the X-band and S-band radar reflectivity of Vesta's surface can therefore be directly attributed to variations in surface roughness at the scale of the wavelength (centimeters to decimeters).

2. Surface Roughness Variability of Asteroid Vesta's Surface

Through radar power spectral signal analysis, we measured the strength of radar forward-scattering properties of different reflection sites on Asteroid Vesta as acquired by the bistatic radar experiment (BSR) conducted by the Dawn mission. Significant spatial variations were observed in the radar reflectivity of the surface, and in light of the spatially uniform dielectric properties of Vesta's surface material, this result implies substantial spatial variations in centimeter-to-decimeter scale surface roughness. Unlike the Moon, however, Vesta's surface roughness variations are not correlated with the age of the surface as inferred from crater counting methods, suggesting that impact cratering is not the only process shaping the asteroid's surface. Instead, the occurrence of heightened hydrogen concentrations within large smoother terrains (over hundreds of square kilometers) suggest that potential ground-ice presence may have contributed to the formation of Vesta's current surface texture. Moreover, this hypothesis is consistent with geomorphological analysis of Dawn Framing Camera images of crater walls by Scully et al. (2015), who identify curvilinear gullies that may have been formed by transient fluid flows. Given that water-ice can survive on airless bodies in the main asteroid belt, provided they are buried at sufficient depth and overlain by a thick, porous regolith (Schorghofer, 2008; Stubbs & Wang, 2012), we postulate that water occurrence at Vesta's surface could result from intense heating, melting and subsequent flow of buried water-ice upward along deep impact-induced fractures in the case of a high-energy collision.

3. Future Opportunities for Conducting BSR Observations of Small-Bodies

The combination of constructing a dielectric model of Asteroid Vesta's surface and analyzing the orbital BSR data acquired by the Dawn mission has resulted in the first assessment of Vesta's surface roughness variability. In turn, surface roughness can be used to infer the primary geophysical processes that have shaped the target body, and provides valuable input for assessing surface trafficability for future landing, anchoring and sampling missions. We examined nominal orbital parameters associated with ongoing and planned missions to other small-bodies, as well as the Jovian and Saturnian icy moons, to assess the feasibility of conducting other low-risk opportunistic forward-scatter BSR experiments. In order to successfully quantify relative surface roughness, we find that an onboard ultra-stable oscillator (USO) is necessary onboard the spacecraft when the target body is ≲100 km in diameter so as to accurately distinguish the main carrier signal from the slightly Doppler-shifted surface-scattered signal during power spectral analysis in the orbital acquisition geometry associated with forward scatter. In light of impending prospects for exploring asteroids and small moons through the use of landers—including the ongoing JAXA mission that has just set two landers on Asteroid Ryugu (JAXA National Research and Development Agency, 22 Sept. 2018), and NASA's OSIRIS-REx mission that is en route to Asteroid Bennu for sample collection (Jones & Morton, 24 Aug. 2018)—surface roughness characterization at the scale of centimeters to meters will be crucial for assessing surface trafficability. Conducting opportunistic BSR experiments by ongoing and planned missions to such bodies presents a low-cost, low-risk means by which to accomplish this goal.

4. References

Jones, N. N. & Morton, E. (24 Aug 2018). "NASA's OSIRIS-REx Begins Asteroid Operations Campaign." [Press Release] https://www.nasa.gov/feature/goddard/2018/nasas-osiris-rex-begins-asteroid-operations-campaign

Palmer, E. M., Heggy, E., Capria, M. T. & Tosi, F. (2015). "Dielectric properties of Asteroid Vesta's surface as constrained by Dawn VIR observations." *Icarus*, **262**, 93–101. doi:10.1016/j.icarus.2015.08.031

Palmer, E. M., Heggy, E. & Kofman, W. (2017). "Orbital bistatic radar observations of asteroid Vesta by the Dawn mission." *Nat. Commun.*, **8**(409). doi:10.1038/s41467-017-00434-6

Palmer, E. M. & Heggy, E. (Under Review). "Measurement Requirements for Orbital Forward-Scatter Bistatic Radar Observations of Planetary Surfaces." Submitted to: *IEEE Geosci. Remote Lett.*

Schorghofer, N. (2008). "The Lifetime of Ice on Main Belt Asteroids." *Astrophys. J.*, **682**(1), 697–705. doi:10.1086/588633

Scully, J. E. C., Russell, C. T., Yin, A., Jaumann, R., Carey, E., Castillo-Rogez, J., McSween, H. Y., Raymond, C. A., Reddy, V. & Le Corre, L. (2015). "Geomorphological evidence for transient water flow on Vesta." *Earth Planet. Sci. Lett.*, **411**, 151–163. doi:10.1016/j.epsl.2014.12.004

Stubbs, T. J. & Wang, Y. (2012). "Illumination conditions at the Asteroid 4 Vesta: Implications for the presence of water ice." *Icarus*, **217**(1), 272–276. doi:10.1016/j.icarus.2011.11.007

JAXA National Research and Development Agency (22 Sep 2018). "MINERVA-II1 of Hayabusa2 Touches Down Ryugu." [Press Release] http://global.jaxa.jp/press/2018/09/20180922_minerva2.html

APPENDIX

Complementary Perspectives from Comet 67P and the Moon

This section summarizes three studies that are complementary to the major themes of this dissertation. In addition to the Dawn mission, I have been fortunate to contribute to other projects that support space missions and our understanding of ice distribution throughout the solar system, including the European Space Agency's Rosetta mission to Comet 67P/Churyumov-Gerasimenko and NASA's Lunar Reconnaissance Orbiter (LRO) to the Moon. The first two studies relate to characterizing the radar properties of Comet 67P both before and after Rosetta's arrival, and reveal significant changes in our understanding of the surface texture of active cometary nuclei. While potential water occurrence at the surface of Asteroid Vesta was hypothesized in Chapter III to act as a smoothening mechanism, on actively outgassing comets that contain much more ice, we observe that most of the surface is very rocky and rough, likely associated with constant resurfacing by volatile outgassing. In the third study mentioned here, I helped examine LRO radar observations of crater fills that suggest the dielectric constant of the lunar surface is not as homogeneous as once thought, and instead that the dielectric constant of crater fills are observed to increase with increasing crater size. The ability to examine the dielectric properties of the lunar surface at such high resolution is a significant benefit of its proximity to the Earth. We can likewise apply this knowledge to enhance our understanding of the detailed radar properties of other airless basaltic/siliceous small-bodies.

Radar properties of comets: Parametric dielectric modeling of Comet 67P/Churyumov-Gerasimenko

Heggy, E., Palmer, E. M., Kofman, W., Clifford, S., Righter, K. & Hérique, A.
Partially reprinted from: Icarus, **221**, 925–939, doi:10.1016/j.icarus.2012.09.023

In 2014, the European Space Agency's Rosetta mission is scheduled to rendezvous with Comet 67P/Churyumov–Gerasimenko (Comet 67P). Rosetta's CONSERT experiment aims to explore the cometary nucleus' geophysical properties using radar tomography. The expected scientific return and inversion algorithms are mainly dependent on our understanding of the dielectric properties of the comet nucleus and how they vary with the spatial distribution of geophysical parameters. Using observations of comets 9P/Tempel 1 and 81P/Wild 2 in combination with dielectric laboratory measurements of temperature, porosity, and dust-to-ice mass ratio dependencies for cometary analog material, we have constructed two hypothetical three-dimensional parametric dielectric models of Comet 67P's nucleus to assess different dielectric scenarios of the inner structure. Our models suggest that dust-to-ice mass ratios and porosity variations generate the most significant measurable dielectric contrast inside the comet nucleus, making it possible to explore the structural and compositional hypotheses of cometary nuclei. Surface dielectric variations, resulting from temperature changes induced by solar illumination of the comet's faces, have also been modeled and suggest that the real part of the dielectric constant varies from 1.9 to 3.0, hence changing the surface radar reflectivity. For CONSERT, this variation could be significant at low incidence angles, when the signal propagates through a length of dust mantle comparable to the wavelength. The overall modeled dielectric permittivity spatial and temporal variations are therefore consistent with the expected deep penetration of CONSERT's transmitted wave through the nucleus. It is also clear that changes in the physical properties of the nucleus induce sufficient variation in the dielectric properties of cometary material to allow their inversion from radar tomography.

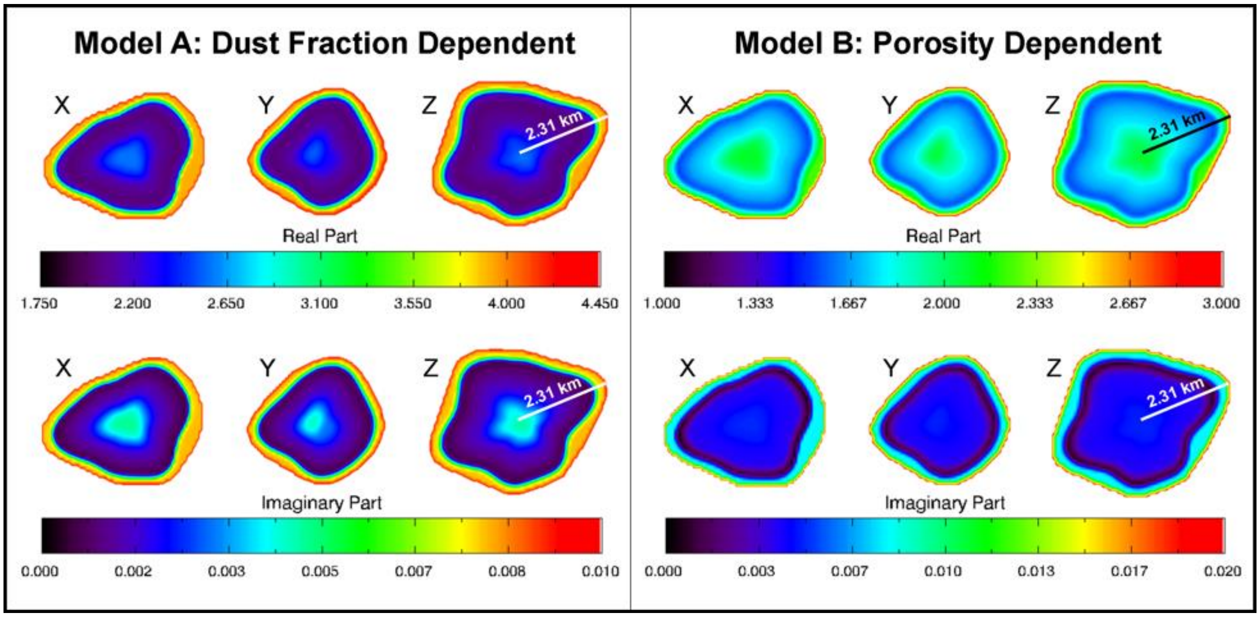

Figure 1. Two hypothesized pre-rendezvous dielectric models of Comet 67P. Models A and B are constructed assuming a layered inner structure. The comet nucleus' dielectric properties are modeled using empirical formulas that relate ε' and ε'' to different dust fractions and porosities of chondritic dust mixtures with ice. The outermost layer consists of ~1-15 m of ice-free dust and is underlain by a crystalline ice crust ~250 m thick. The remaining interior is comprised of successive layers of dirty ice. Model A shows dust fraction increasing toward the core for a fixed porosity. Model B shows porosity decreasing toward the core with a fixed dust fraction. The modeled dielectric gradients through the comet interior suggest that CONSERT will be able to detect changes in dust mass-fraction of ±20% and changes in porosity of ±10%.

Post-Rendezvous Radar Properties of Comet 67P/CG from the Rosetta Mission: Understanding Future Earth-Based Radar Observations and the Dynamical Evolution of Comets

Heggy, E., Palmer, E. M., Hérique, A., Kofman, W. & El-Maarry, M. R.

Under review by: Monthly Notices of the Royal Astronomical Society

Rosetta's two-year mission at comet 67P/Churyumov-Gerasimenko (67P/CG) has significantly improved our understanding of the radar properties of comets and the insights they provide into the formation history and dynamical evolution of the nucleus. Rosetta's CONSERT radar experiment has transmitted radar pulses through the inner comet head, and does not observe measurable signal broadening that could be associated with the presence of subsurface inclusions, which in turn represent the primordial building blocks of the nucleus. This result implies that primordial building blocks could be smaller than the radar wavelength and/or have weak dielectric contrast ($\Delta\varepsilon_r'$), thereby producing no measurable broadening, and is consistent with a purely thermal origin for the ~3-m surface bumps observed on pit walls and cliffsides, hypothesized to be high-centered polygons formed from the fracturing of the sintered shallow subsurface during seasonal thermal expansion and contraction. Using Rosetta mission observations, contrary to previous assumptions of cometary surfaces being dielectrically homogeneous and smooth, we now find that cometary surfaces can be dielectrically heterogeneous ($\varepsilon_r' \approx 1.2$-$2.7$), and rough at both S- and X-band radar wavelengths (i.e., centimeters to decimeters). Future changes in the observed radar reflectivity of 67P/CG will be mostly induced by large-scale structural rather than small-scale textural changes of the comet nucleus. By monitoring changes in 67P/CG's radar properties over time via future Earth-based and orbital radar observations, we will be able to characterize the ongoing dynamical evolution of cometary nuclei.

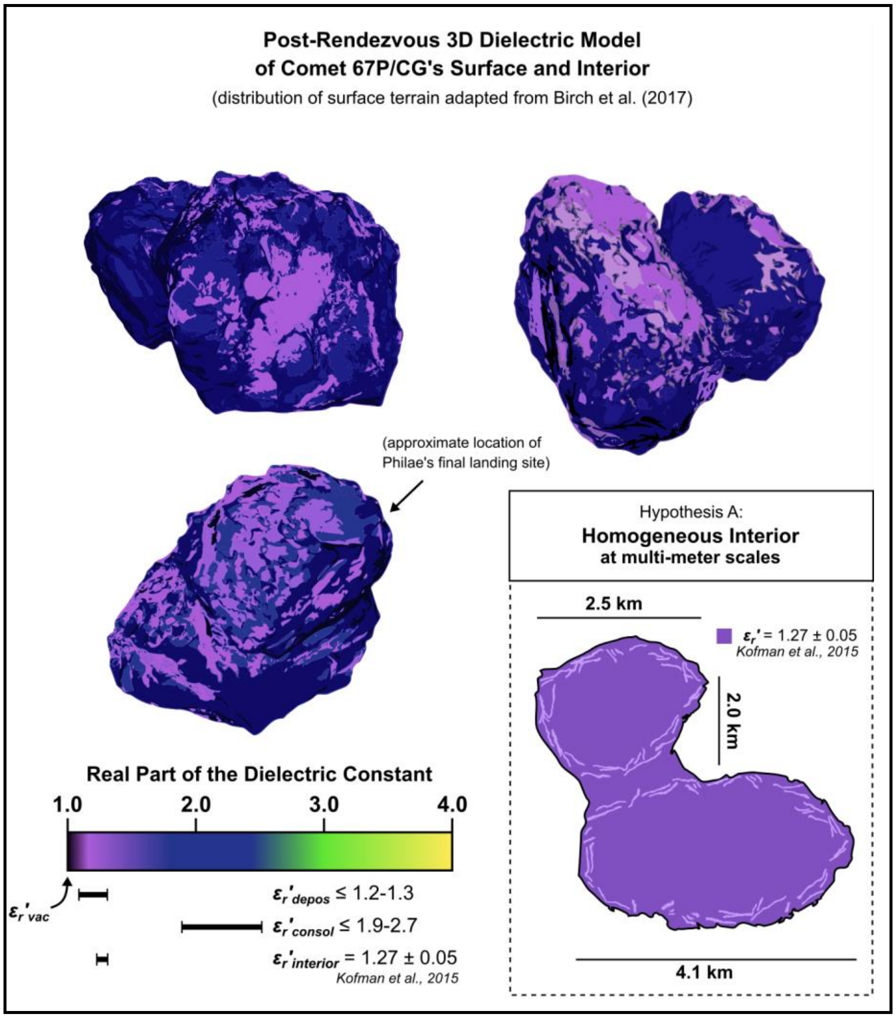

Figure 2. Post-rendezvous updated 3D dielectric model of Comet 67P. Unlike asteroids, which have thick, well-gardened regoliths with homogeneous dielectric properties, Comet 67P/CG has an actively reworked surface with a subsequently dielectrically heterogeneous surface due to the uneven distribution of regolith material. Roughly 30% is covered by thick, loose fine-grained surface deposits of dust and ice with $\varepsilon_r' \lesssim 1.3$, and 70% consists of consolidated material with $\varepsilon_r' \lesssim 1.9\text{-}2.7$. In addition, the surface appears rough at all scales (cm to m), suggesting that the dielectric constant of the surface material cannot be inferred from either X- or S-band radar backscatter observations without radar propagation simulations, since the signal will be dominated by diffuse backscatter. We suggest that changes in 67P's radar reflectivity observed over time by Earth-based radar would correspond to large-scale changes in the comet's structural and textural properties, whether indicative of increased fine-grain surface deposit coverage and subsequent increase in surface insolation, or increased roughness associated with increased fracturing and thermal weathering of cliff-sides, overhang collapses and/or nucleus breakup.

Exploring the Dielectric Properties of Lunar Crater Fills Using Radar Observations by Chandrayaan-1/Mini-SAR and LRO/Mini-RF

Heggy, E., Palmer, E. M., Fa, W., Thompson, T. W., Thompson, B. J. & Patterson, G. W.

Submitted for review to: Earth and Planetary Science Letters

Identifying polarimetric radar signatures for ice inclusions in the lunar regolith at the poles of the Moon is hampered by a lack of knowledge about the variabilities in the dielectric properties of mixtures of the lunar regolith and ice. To address this ambiguity, we assess the dielectric properties of the lunar surface as inverted from LRO Mini-RF and Chandrayaan-1 Mini-SAR polarimetric backscattered signals. In particular, we measure the dielectric properties of crater fills in north polar and equatorial regions in an attempt to constrain the range of variability of the dielectric constant as a function of latitude and crater diameter, where the latter is indicative of excavated soil depth. Our observations suggest that the average dielectric constant of the lunar surface ranges from 2.3 to 3.8 at S-band radar frequencies, and that surface dielectric properties do not show a dispersive dependence on frequency through X-band. The dielectric constant of crater fills is found to be correlated with crater size, with small craters having a value of 2.3-2.7, and large ones having values as high as 3.8. Our results suggest that with increasing crater size up to ~8 km, simple crater fills may contain an increasing abundance of centimeter- to decimeter-sized rocks, hence increasing ε_r'. If the observed dependence of dielectric properties on crater size is typical for dry lunar regolith, then our findings also suggest that the detectability of porous water-ice by S- and X-band radar is most likely achievable within craters $\gtrsim$5 km in diameter and less likely within smaller craters due to dielectric contrast requirements.

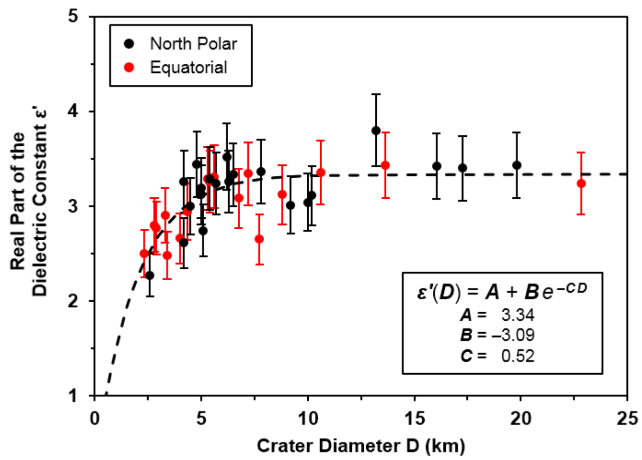

Figure 3. Inverted dielectric constant of lunar crater fills vs. crater diameter. We suggest that simple crater fills with ε_r' below the best-fit curve are potential candidates for ice inclusions since the occurrence of porous ice would lower ε_r' from the value of dry, ice-poor lunar regolith. To maximize the detectability of water-ice occurrence, these results suggest that future S- and X-band radar observations should target the crater fills of simple craters $\gtrsim$5 km in diameter, since the dry crater-fill material in these craters has the highest dielectric contrast with porous ice inclusions. Crater fills with anomalously high ε_r' are likely explained by the presence of higher density material (e.g., a potentially younger crater with higher cm-dm rock abundance at the surface and shallow subsurface).